

Section of Electrical and Computer Engineering
Department of Engineering
Aarhus University

Detection of Joint Destructions in High-Resolution Peripheral Quantitative Computed Tomography Images

Master's Thesis in Computer Engineering

Frederik Andersen
MSc student
AU503241@uni.au.dk

Morten Morberg Madsen
MSc student
AU501465@uni.au.dk

Supervisor:
Christian Fischer Pedersen

June 3, 2018



Section of Electrical and Computer Engineering
Department of Engineering
Aarhus University

IT-byen Katrinebjerg
Finlandsgade 22
8200 Aarhus N, Denmark

+45 8715 0000
eng@au.dk
eng.au.dk

Preface

This master's thesis was carried out at the Department of Engineering, Aarhus University in an interdisciplinary collaboration with the Department of Rheumatology, Aarhus University Hospital. The thesis is completed in accordance to the requirements for acquiring a master's degree in Computer Engineering.

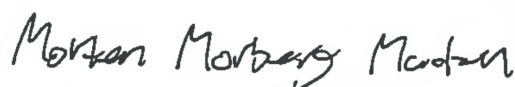
The authors would like to express their gratitude to Christian Fischer Pedersen for his outstanding guidance and supervision throughout the study. Also, a special thanks to Ellen Margrethe Hauge, Kresten Krarup Keller, Rasmus Klose and the Department of Rheumatology, Aarhus University Hospital for the interdisciplinary collaboration and providence of relevant data. Finally, it is the authors hope that the contributions made in this study, will benefit further research in the area of rheumatoid arthritis.

All source files associated with the study are found at: <https://morberg@bitbucket.org/morberg/dojdih-r-pqct.git>

Aarhus, June 3, 2018



Frederik Andersen



Morten Morberg Madsen

Abstract

In this study, a new method is presented for automatic detection and quantification of cortical breaks in high-resolution peripheral quantitative computed tomography images (HR-pQCT). The purpose of the method is to aid domain personal in disease prognosis of patients affected with the chronic autoimmune disease rheumatoid arthritis.

For the proposed method, a hybrid segmentation method is developed with the purpose of isolating the bone joints by their periosteal surface. The hybrid segmentation method is composed of thresholding, morphological operations and active contour segmentation techniques. Due to bone alignment problems, as a result of patient motion during image acquisition, a registration method is presented with the purpose of realigning the bone joint structures. A detection and quantification method is presented, using the resulting output of the segmentation method. Utilizing image manipulation techniques, cortical breaks are detected and quantified in accordance with specific erosion criteria. The proposed method was validated against visual erosion detections, from where the methods sensitivity and precision were defined. The erosion quantification capabilities was validated using accuracy and precision based on visual erosion quantifications.

Through the method validation, it is verified that the proposed method is able to automatically detect and quantify erosions. The detection sensitivity is 71.8% with a precision of 6.6%. The quantifications of detected erosions have an accuracy error of 19%-29.9% and a precision error of 44.1%-77.7% when compared to visual erosion quantifications.

The proposed method has a high sensitivity and a low precision, indicating that the method detects more erosions than specified by the visual detection. The high number of erosion detections is closely related to image noise artifacts which creates a basis that fulfills the criteria for possible erosions. The origin of these noise artifacts is from the image acquisition process.

The proposed automatic method shows promising results and is considered a valid aiding tool for domain personal in the estimation of bone erosions. Moreover, the method acts as a basis for further development in automatic rheumatoid arthritis progression estimation using HR-pQCT imaging.

Résumé

Dette studie præsenterer en ny original metode til automatisk detektion og kvantificering af kortikale brud ved benyttelse af den medicinske billede modalitet HR-pQCT. Formålet med metoden er, at afhjælpe domæne personale i prognosticering og diagnosticering af patienter, som er ramt af den kroniske, inflammatoriske ledsygdom rheumatoid arthritis, også kendt som leddegigt.

Til brug i den endelige metode er der udviklet en sammensat segmenteringsmetode med henblik på at isolere knogleled ved deres periostale omkreds. Segmenteringsmetoden er sammensat af tre segmenteringsteknikker, herunder thresholding, morfologiske operationer samt aktive konturer. Patientbevægelse under scanningsprocessen medfører utilpassede scanningsbilleder, bestående af indhak i det aksiale plan. Til formålet at indjustere denne problematik, er der udviklet en registreringsmetode. En metode til detektion og kvantificering er udviklet på baggrund af det grundlag segmenteringsmetoden resulterer i. Denne er baseret på en række billedmanipulations metoder samt morfologiske operationer, som muliggøre detektionen af kortikalske brud i overensstemmelse med en række kriterier for erosioner.

Valideringen af den endelige metode er udført ved sammenligning med visuelle detektioner, som anses som den gyldne reference inden for området. Herunder er detektionsmetoden valideret på baggrund af sensitiviteten samt dens præcision, og kvantificeringen ved akkuratess samt præcisions værdier.

Under valideringen af metoden, blev det verificeret at den foreslåede metode er i stand til automatisk at detektere og kvantificere erosioner. Detektionen er mulig med en sensitivitet på 71.8%, samt en præcisions fejl på 6.6%. Samtidig opnår kvantificering metoden en akkuratess fejl på 19%-29.9% samt en præcision på 44.1%-77.74% ved sammenligning af de visuelle kvantifikationer.

Den højere sensitivitet sammenlignet med den lave præcision indikerer at metoden detekterer flere erosioner end den visuelle detektion. Dog skyldes det højere antal også støj artefakter som fejlagtigt bliver medtaget som erosioner, da deres indvirkning på segmenteringsmetoden danner et grundlag som opfylder de kriterier, der skal til for at godtage en mulig erosion. Disse artefakter opstår under scanningsprocessen, grundet fejlkalibrering og patientbevægelse.

Metoden viser generelt lovende resultater, og anses som et brugbart værktøj for domæne personel i deres estimering og analyse af erosioner. Herudover danner metoden også et basis for fremtidig udvikling indenfor automatisk rheumatoid arthritis progressions estimation ved brug af HR-pQCT billeder.

Table of Contents

Preface	iii
Abstract	v
Resumé	vii
Table of Contents	ix
1 Introduction	1
1.1 Rheumatoid Arthritis	2
1.2 Research Group	2
1.3 High-Resolution peripheral Quantitative Computed Tomography	3
1.4 Problem Formulation	4
2 State of the Art	5
3 Methods	9
3.1 Dataset	9
3.2 Proposed Method Overview	13
3.3 Preprocessing	14
3.4 Segmentation	16
3.5 Registration	42
3.6 Erosion Detection and Quantification	50
4 Experiments and Results	57
4.1 Manual Labeling	57
4.2 Segmentation Experiments and Results	58
4.3 Registration Experiments and Results	71
4.4 Erosion Detection and Quantification Experiments and Results	74
4.5 Profiling Experiment and Results	78
5 Discussion	81
5.1 Further Research	84
6 Conclusion	85
6.1 Perspectivation	85
6.2 Contributions	86
6.3 Personal Contributions	87
A Manual Labeling	89
B Active Contour Results	94
Bibliography	97

Chapter 1

Introduction

This study addresses automatic detection and quantification of joint destructions, utilizing the forthcoming medical image modality High-Resolution peripheral Quantitative Computed Tomography (HR-pQCT).

Joint destruction is an indicator of disease activity for rheumatoid arthritis (RA), which is a chronic inflammatory joint disease [1]. RA is known to not only reduce the quality of life for affected patients, but also reduce the expected lifetime by ten years [2]. Joint destruction in form of cortical bone erosions can occur at an early disease stage, making it a highly favorable indicator for early disease prognosis [3].

The technological development of modern day medical imaging modalities, are strongly tied to the reliability of detection and analysis of erosions. A forthcoming modality showing promising results within the field of erosion detection is HR-pQCT.

Presently, most of all erosion detection and quantification is carried out manually. It is therefore considered both inconsistent and time consuming due to the personal involvement of specialists with domain knowledge. Few studies have tried to automate the erosion detection and quantification process in HR-pQCT images by utilizing medical image processing.

Töpfer et al. [4] introduced a semi-automatic method where region growing techniques are used to quantify manually marked erosions.

An automatic erosion detection method was proposed by Peters et al. [5]. Their method is based on periosteal surface segmentation, followed by various image manipulation steps leading to erosion isolation. The method is presented as a automatic procedure, however the authors advise the use of a semi-automatic procedure, in order to assure quality. Currently, no automated method both capable of detection and quantification of erosions in HR-pQCT images exist.

The aim of this study is to develop an automatic method capable of both detecting and quantifying erosions associated with RA, in the HR-pQCT images. The study is an interdisciplinary collaboration between the Department of Rheumatology, Aarhus University Hospital and the Department of Engineering, Aarhus University.

The development of such automatic method could in a civil context improve patient progression estimation reliability as well as reduce manual involvement during this process.

The remaining of this chapter provides background information associated with the study. A description of RA is provided in section 1.1, presenting the motivation behind the study. Furthermore, the research group, which is the origin of the study, is presented in section 1.2. To understand the significance of the forthcoming image modality, HR-pQCT is described in section 1.3 . Lastly, section 1.4 presents the initial problem formulation of the study.

1.1 Rheumatoid Arthritis

The chronic autoimmune disease rheumatoid arthritis can affect various parts of the human body and primarily it impacts the joints located in wrists and hands. In most cases the disease may cause joint inflammation resulting in pain, stiffness, swelling and warmth in the affected regions. However, the mortality of the disease is considered significant as a result of joint destruction and disability [2].

RA inflicts around 0.5% to 1%, of the population in the northern hemisphere, from urban to rural areas [1]. The causation of RA is not fully understood but involves a complex interplay of environmental and genetic factors [6]. Statistical risk factors associated with RA includes smoking, socioeconomic status and educational attainment [1]. Because of the chronology of the disease, it leads to huge socioeconomic effects, both in medical expenses and in reduced work capacity. Treatment of RA consist of surgery, patient education, physical and occupational therapy as well as drug treatment [6].

One of the main features of RA are bone erosions, which can be used as a diagnostic criteria, as they relate to disease activity [7]. Bone erosions are considered as breaks in the cortical bone, which is the hard shell surrounding the inner more porous trabecular (spongy) bone containing the bone marrow. However, the cortical breaks are accompanied by further destruction into the trabecular bone. Seen on fig. 1.1 are three cases of active bone erosions in three different RA patients. In all three

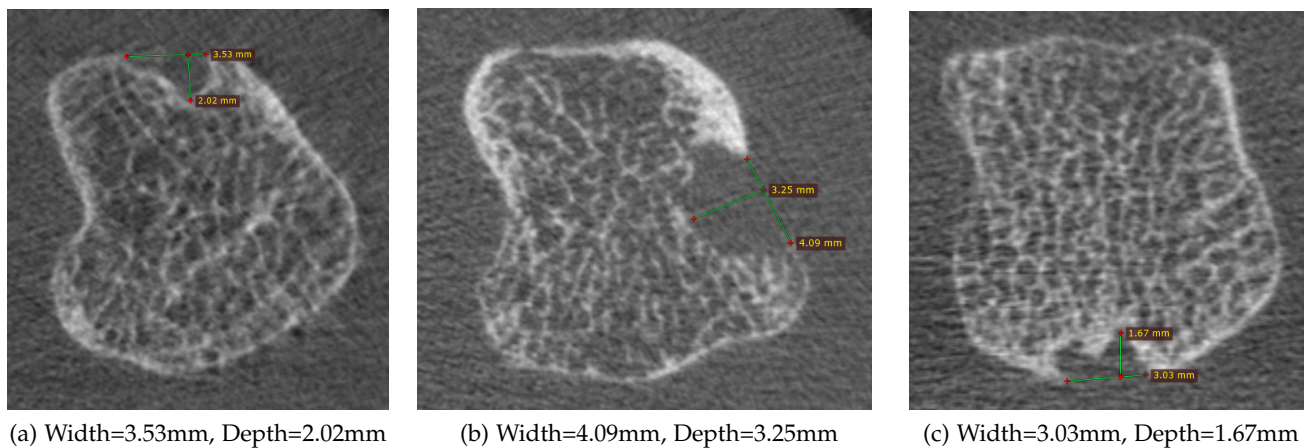


Figure 1.1: Three cases of active erosions located in joints of RA patients, which has been scanned using HR-pQCT.

cases, interruption of the cortical contour is present along with trabecular destruction.

Bone erosions occur early in the disease stage, and may be detectable after a few weeks. Studies show that bone erosions affect half of all untreated patients affected by RA after 6 months [7]. The importance of early erosion detection is therefore a necessity for rapid treatment of RA.

1.2 Research Group

A danish study was established in 2014, with the purpose of estimating the efficiency and safety regarding a new protocol for early RA treatment [8]. The study is named DanACT, and includes rheumatology departments in Aarhus, Silkeborg, Horsens, Gråsten, Svendborg and Odense.

A spin-off research group to the DanACT study was created at Aarhus University Hospital, with the overall purpose of investigating the HR-pQCT image modality as a prognostic marker for RA [9]. The HR-pQCT data used in this investigation derives from a subgroup of patients covered by the

DanACT study.

Associated to this research group, a PhD project was proposed, accepted and initialized at the Department of Rheumatology, Aarhus University Hospital. The purpose of this study, is to test two overall objectives [2]. The first objective is to determine if erosive bone changes can be detected at an earlier stage by the use of HR-pQCT imaging. The second objective is to test if an automated algorithm can be developed to decrease variation and cost of RA disease evaluation.

To realize the second objective, an interdisciplinary collaboration between Department of Rheumatology, Aarhus University Hospital and the Department of Engineering, Aarhus University has been established, and thereby creating the origin of this master's thesis.

In addition to interdisciplinary collaboration and guidance, the Department of Rheumatology has contributed to the study with HR-pQCT image data, originating from the DanACT study, as well as visual erosion quantifications.

1.3 High-Resolution peripheral Quantitative Computed Tomography

High-Resolution peripheral Quantitative Computed Tomography is an adaption of the conventional medical image modality Computed Tomography (CT). HR-pQCT images are acquired using sequential radiographic projections, captured over a range of angular positions around the object of interest [10]. As presented on fig. 1.2, these projections are captured by a set of detectors, from where the raw projections are further combined through computational techniques, to create the reconstructed 3D image set. Special for CT modalities are a high intensity difference between soft tissue and bone structure. CT and its submodalities are therefore well suited for analysis and processing of bone imaging, including determination of joint and erosion margins [11]. Notably, the cortical bone is easily identified due to its high absorption rate of the radiographic projections. All CT modalities are calibrated with a reference to water, making intensities across scanners closely related [12].

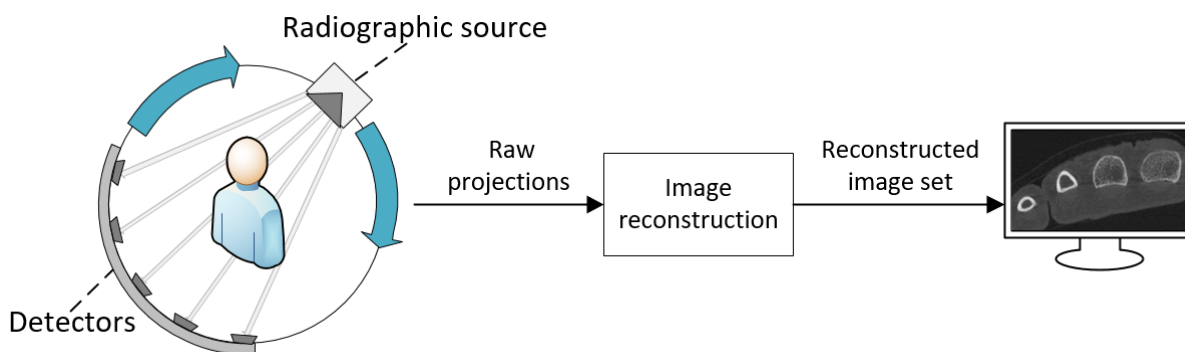


Figure 1.2: HR-pQCT data acquisition process.

The HR-pQCT modality is developed to examine in vivo volumetric bone mineral density (BMD) and microarchitecture of the peripheral limbs [13]. It is considered to have a high signal-to-noise ratio (SNR) and a spatial resolution with a nominal isotropic voxel dimension of $82\mu m$ [10]. Moreover, HR-pQCT exposes patients to a considerably lower radiation dose compared to regular x-ray, making it advantageous for scenarios where multiple scans are desired over time. All these factors in combination with a shorter acquisition time, when comparing to MRI, makes HR-pQCT an interesting method for advanced imaging in clinical RA studies [14].

The primary manufacturer behind HR-pQCT is Scanco Medical AG located in Brüttisellen, Switzerland [15]. This is also the manufacturer behind the clinical scanner of the model XtremeCT, seen on

fig. 1.3, which was used to acquire the data associated with this study. XtremeCT is designed specifically for in vivo osteoporosis studies concerning the distal tibia and radius, and therefore developed for larger bone architectures than the human hand.



Figure 1.3: XtremeCT HR-pQCT scanner by Scanco Medical AG. Reprinted from [16].

Several other submodalities of CT exist including μ CT and multidetector CT. Each type of CT modality adaption varies in precision and resolution, with μ CT being the leading modality in both factors. μ CT is on the other hand only capable of in vitro scanning, or in vivo scanning of small animals such as mice [17]. This makes HR-pQCT considered the de facto method for clinical in vivo distal bone analysis.

1.4 Problem Formulation

High-Resolution peripheral Quantitative Computed Tomography (HR-pQCT) is a forthcoming medical imaging technique, applicable for detection and analysis of bone erosions related to rheumatoid arthritis, affecting around 35.000 people in Denmark. Treatment escalation for rheumatoid arthritis is among others based on the progression and severity of joint erosions.

The focus of the presented master's thesis is to design, implement, test and document a method for automatic detection and quantification of erosions based on HR-pQCT images. The method must prove itself functional via concrete experiments. To quantify the quality of the method, statistical comparisons with current state of the art, which is manual detection, should be carried out via objective quality metrics. These comparisons should lead to an overall assessment of the potential impact and significance of the method.

In a social context, such a method could improve the reliability of patient progression estimation. Secondly, it could reduce personal involvement for manual data analysis, and thereby reduce financial expenses.

Chapter 2

State of the Art

The following chapter presents the current state of RA disease diagnostic in medical image processing. Various approaches for different image modalities have been proposed, leading to the current work with HR-pQCT.

Medical imaging plays a key role in modern RA disease diagnostic and prognosis estimation. The reason for this is that different types of disease indicators can be extracted from the medical images and further used for prognosis estimation. One such indicator is BMD, which can be used to estimate the internal destruction as a result of the disease [18]. Another indicator is the quantification of joint space width (JSW), which can be used to assess the level of structural damage [19].

The indicator covered in this study, is bone erosions which is considered highly desirable for RA disease diagnosis, as bone erosions are a main feature of RA [7]. Moreover, early diagnostics is possible through erosion detection, as it can occur early in the course of RA [3]. Erosion activity monitoring is also used to measure disease progression, as erosion activity is closely associated to progressively impaired joint functionalities for RA patients [20].

The precision of bone erosion detection and quantification is directly connected to the medical image modalities.

One medical image modality used for semi-quantification bone erosion assessment is Conventional 2D Radiography (CR) [4]. CR is seen as the origin to modern medical imaging techniques and is typically used for daily clinical practice [3].

Moreover, CR is used in an automatic method developed by Huo et al. [19] for JSW estimations. However, due to the limited sensitivity as a result of the 2D projectional character, CR is known to underestimate both the number and volume of erosions [21]. Therefore, more sensitive imaging modalities are used for better correctness and precision erosion detection and quantification.

A modality with increased sensitivity is Magnetic Resonance Imaging (MRI). MRI is capable of creating 3D representations of the scanned region, thereby providing more information than the 2D CR. Multiple methods for erosion detection and quantification are proposed for the MRI modality.

Bird et al. [22] and Crowley et al. [23] both proposed semi-automated methods for erosion quantification in wrists of RA patients. Both methods are depending on manual segmentation by outlining detected erosions. Emond et al. [24] presented another semi-automatic method for erosion quantification by utilizing region growing techniques for segmentation of the bone erosion volumes.

The MRI modality is considered less effective than the CT modality for structural bone change assessment [25]. This is due to the weak voxel intensity contrast between the bone structure and soft tissue, as seen on fig. 2.1.

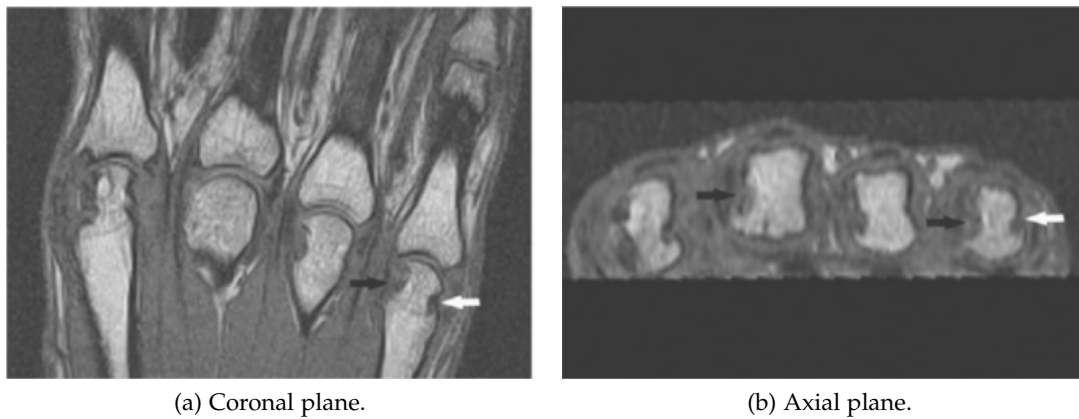


Figure 2.1: MRI scan of finger joints. Arrows point towards erosions. Reprinted from [25].

Another semi-automatic method for erosion detection on human wrists, using the CT modality, was proposed by Duryea et al. [26]. Their approach was based on manual 2D segmentation of the periosteal surface using a graphical user interface (GUI), followed by active contour segmentation. Finally, region growing segmentation was used to quantify the erosion volumes. Newer CT modalities has later been presented with an increase in resolution and sensitivity, thereby providing a better basis for erosion detection and quantification.

Finally, the in vivo CT adaption HR-pQCT, as presented in section 1.3, has shown almost perfect reliability when compared to μ CT for erosion detection and quantification [5, 17]. A semi-automatic method for erosion quantification in HR-pQCT images was presented by Töpfer et al.[4].

The first step of their method covers periosteal surface segmentation, which is acquired using a method consisting of region growing, local adaptive thresholding and morphological operations. Based on the periosteal surface segmentation, erosions were manually identified by placing a seeding point in each interruption. These points were then inflated iteratively using a level set based algorithm, stopping at a given voxel intensity value, resulting in a closed 3D volume.

In the case of low-intensity edges in the periosteal surface, the inflation might yield leakage in non-erosion bone areas. In the scenario of inflation leakage an optional step is used, however, this requires manual detection of the leakage.

The method is considered promising in its quantification of bone erosions, still this is based on multiple manual steps, including seeding point placement and detection of inflation leakage.

Another method for automatic detection of erosions in HR-pQCT images, was introduced by Peters et al. [5]. Their proposed method consists of four main steps. The first step is to segment the periosteal surface, which is realized through a segmentation method produced by the scanner manufacturer [11]. Secondly, a solid volume of the periosteal segmentation is created. Thirdly, morphological operations is used to define the outer shell of the volume, resulting in an approximation of the cortical bone, with a constant thickness of 4 voxels. Lastly, this outer shell is analyzed for discontinuities, which meets defined erosion properties, resulting in the final detected erosions. Because of contour errors produced by the method, they propose a semi-automatic procedure for contour correction. The semi-automatic process provides promising results, whereas the automatic process is disapproved by the authors, as quality cannot be guaranteed.

In addition to the erosion detection and quantification methods presented above, another study based

on the HR-pQCT modality has yielded a standardized method for quantification of BMD and microarchitecture properties, for the trabecular bones in hands and wrists [27]. The standardization, presented by Yang et al. [27], is based on a standard method for extraction of trabecular bone density and structure properties [28]. The method shows promising results for RA prognosis estimation.

Chapter 3

Methods

The following chapter addresses the material and methods used for the proposed erosion detection and quantification method. Section 3.1 addresses the image data used in this study and introduces the source of the image data, the acquisition process and various properties related to the datasets. To give an overview of the proposed erosion detection and quantification method, section 3.2 introduces the selected submethods and their purpose. The selected submethods are preprocessing, segmentation, registration and erosion detection and quantification, which is presented in further details in sections 3.4 to 3.6.

The methods presented throughout this study are all implemented using the MATLAB language and framework [29], which is chosen for its intuitive approach to image processing. The MATLAB version used is MATLAB R2018a, in addition with the toolboxes seen in list 3.1:

List 3.1: MATLAB toolboxes used in the study.

- Image Processing and Computer Vision Toolbox [30]
- Medical Image Processing Toolbox [31]
- Curve Fitting Toolbox [32]
- Hausdorff Distance [33]
- Active Contour Segmentation [34]
- Localized Active Contour [35]
- Niblack Local Thresholding [36]

The developed method is intended to partly replace the manual analysis of patient scans, which is not directly considered time critical. Therefore, a rapid processing time is not of highest priority during the method development. At a later point, parallelization of the method onto multiple CPUs or GPUs would greatly reduce the processing time, however, this is not taken into consideration in the scope of this study.

3.1 Dataset

The image data used in this study is collected through the DanACT research study as described in section 1.2. The HR-pQCT image data is acquired from 231 patients and again 3 months later from

180 of those patients.

Patients are fixated in a cast and scanned in approximately 8 minutes [9]. The scanned region length is 2.7 cm for each patient, which is achieved through 3 individual scans of 110 image slice, with the combined length of 0.9 cm. The reason for the 3 combined scans is to achieve a complete scan of the joints of interest. An entire scan is therefore 330 image slices and will hereafter be denoted as a dataset. Each dataset has a voxel size of $82 \times 82 \times 82 \mu m$, while the image resolution is varying between scans.

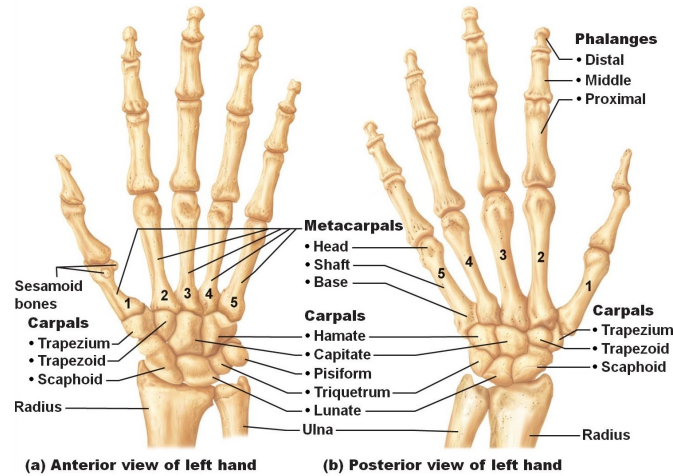


Figure 3.1: Bones of the wrist and hand. Reprinted from [37].

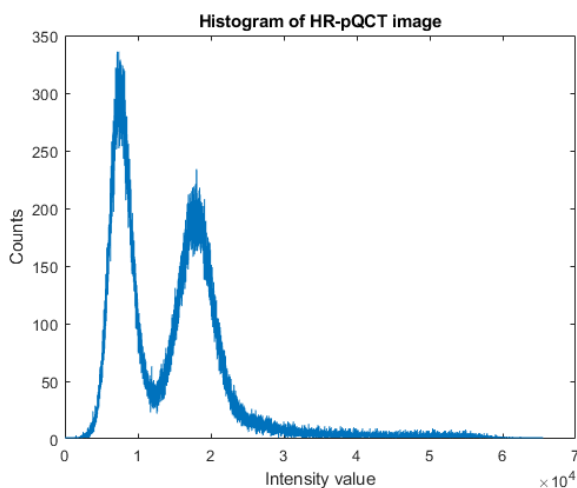
The starting point of the scanned region is located at the head of the 2nd to 5th metacarpal and reaches the base of the 2nd to 5th proximal phalanges, thereby covering the whole metacarpophalangeal joint (MCP) as seen on fig. 3.1. The region of interest (ROI) is considered the 2nd and 3rd MCP, as they are the most commonly erosion affected joints [38]. Therefore the scan is focused at these regions by the placement of the patient hand. The majority of the scans are taken of the right hand, however, some left hand scans are acquired in scenarios where the patients left hand contains known interesting features, or if metal or other distortion objects are located in the right hand.

As a result of different obstructing medical image artifact types, the image quality varies greatly for the acquired data. Miscellaneous artifacts might degrade the image quality in medical images including noise, beam hardening, scatter, pseudoenhancement, motion, cone-beam, helical, ring and metal artifacts [39]. The overall degradation is a combination of both the population, intensity and types of artifacts superimposing the image slices.

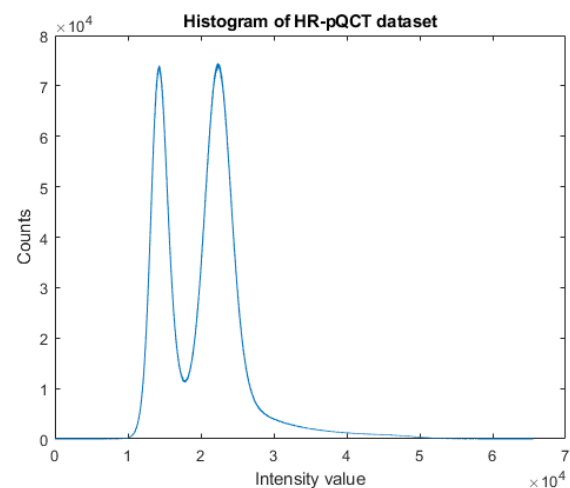
An analysis process of the image quality and relevant image artifacts was conducted to determine plausible challenges, within the image in correlation to the final erosion detection and quantification method. The challenges was analyzed for their possible effect on the images, and how these might be reduced. Examination of the images in this study, reveals that the artifacts mainly degrading the image quality is noise of Gaussian characteristics, patient motion and ring artifacts.

The noise in the images are of Gaussian characteristics [40]. An image histogram of a random image slice within a dataset is shown in fig. 3.2a. It is observed that the histogram contains two curves of Gaussian characteristics. The first left most Gaussian curve represents the image border around the hand, whereas the second right most Gaussian curve represents the hand tissue. The minor pixel intensities after the second Gaussian curve is representing the bone structure and noise.

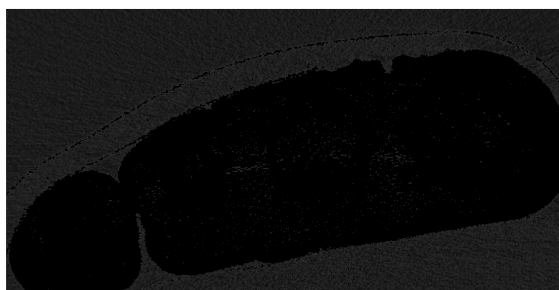
A representation of the left most Gaussian curve is illustrated in fig. 3.2c, where all intensities



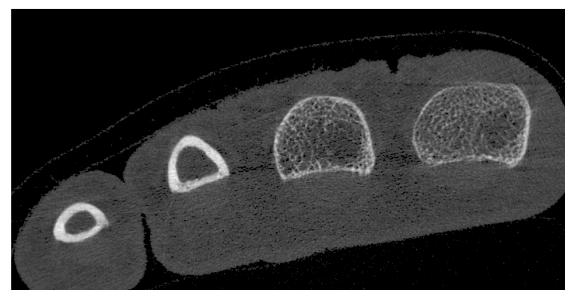
(a) Single HR-pQCT image slice histogram.



(b) Entire HR-pQCT dataset histogram.



(c) Pixel intensities within first Gaussian distribution.



(d) Pixel intensities above first Gaussian distribution.

Figure 3.2: A histogram of a single HR-pQCT image slice is seen in fig. 3.2a. A histogram of an entire HR-pQCT dataset is seen in fig. 3.2b. A HR-pQCT image slice only including intensity values below the Gaussian intersection of fig. 3.2a is seen in fig. 3.2c. A HR-pQCT image slice only including intensity values above the Gaussian intersection of fig. 3.2a is seen in fig. 3.2d.

below the intersection of the two Gaussian curves are included. In addition fig. 3.2d contains all intensities above the Gaussian curve intersection. This tendency of two Gaussian distributions, exists in all HR-pQCT images in this study. A image histogram of a entire HR-pQCT dataset is seen in fig. 3.2b. The information regarding the Gaussian distributions and the image objects contains within, can further be used to separate image information. The characteristics of the Gaussian distributions are however intersecting, and a clear separation is therefore unachievable.

Patient motion artifacts are caused by patient movement during the acquisition of the dataset. The effect of patient motion causes blurring and streaks through the images, especially effecting bone areas, as seen on fig. 3.3a. Even though the patient is fixated to a cast during the scan, patient motion artifacts are still highly present in the images. This is mainly due to the long image acquisition time of 8 minutes. Methods for reduction of patient motion include a faster acquisition time and better fixation methods. Currently a better fixation method is under development for the data acquisition process producing data for this study.

Computational quantification and reduction of patient motion in HR-pQCT images is currently a research topic, with few proposed methods [41, 42]. These proposed methods use the projection data which is not acquirable for this study, as only reconstructed data is available. Patient motion

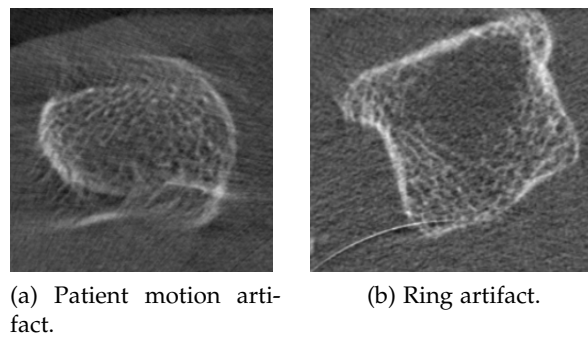


Figure 3.3: An example of a patient motion artifact is shown in fig. 3.3a. An example of a ring artifact is shown in fig. 3.3b.

mainly affects the image quality because bone structures become indistinct. This is expected to have an effect on both segmentation and further analysis of the images as incorrect information is present, and desired information is suppressed.

Ring artifacts are concentric rings often found superimposing the image slices as seen in fig. 3.3b. The cause of ring artifact is typically miscalibrated or defective detector elements in the scanner [39, 43]. Correction and removal of ring artifacts can either be achieved through scanner recalibration or by computationally post scanning methods. Computational methods are divided into two groups; methods applied to projection data and methods applied to reconstructed data. A proposed method for the reduction of ring artifact, in reconstructed HR-pQCT image slices, is introduced in [44] and shows promising results.

The reason for the high image quality degradation from ring artifact is because of its intensity similarities compared with the bone structure. Ring artifacts superimposing the images in this study all have either extremely high or low intensity value. In the case of high intensity values they are hard to disguise from bone structure intensities. Some ring artifacts also superimpose the bone structures, and potentially removes or suppresses desired information. As mentioned above, patient motion contributes negatively to the overall image quality by adding blurred noisy regions to the bones. Moreover, as a dataset is combined by three scans of 110 slices, patient motion between these three separate scans, yields a misalignment in the shift from slice 110-111 and again from 220-221. This misalignment disturbs the image sensitivity in the concerned regions, as possible erosions located in the shift cannot be correctly analyzed in the 3D plane, as the axial planes are not aligned. This misalignment is considered a registration problem.

Based on the artifacts and their severities an image quality metric is desired to rank the overall quality of the datasets. An automatic method of image quality assessment in HR-pQCT images was proposed in [44], but needs more refinement before use. The de facto standard for HR-pQCT image quality assessment is visual scoring by domain personal, through the image acquisition process. This is done through a semiquantitative scale from 1 to 5, where 1 is the highest possible quality and 5 represents worst case image quality [45]. These quality scores was not accessible for the data used in this study. However, domain personal from Aarhus University hospital, did score the individual image slices containing erosions, using the specified scale. Only datasets with quality ranks 1 to 3 were accepted for further analysis, in accordance with manufacture suggestion [45]. This implies that datasets with poor image quality might still exist in the analyzed data, as the grading is only performed on individual image slices.

3.2 Proposed Method Overview

Based on the purpose of this study a method is proposed, which can be subdivided into individual subparts, each having a specific responsibility for the overall erosion detection and quantification. The composition of the method is illustrated in fig. 3.4.

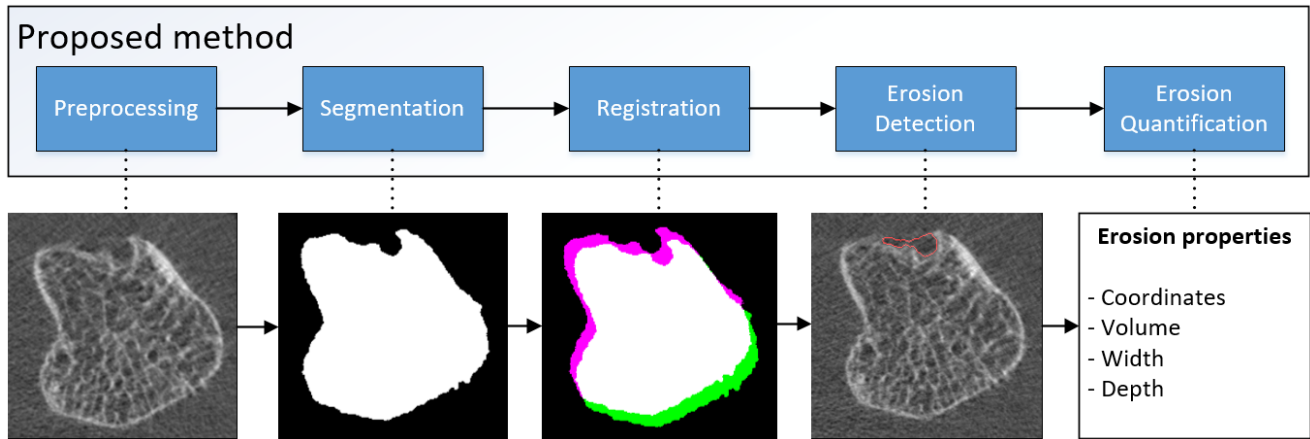


Figure 3.4: The overall proposed method for the entire erosions detection and quantification process. Included are five overall steps following each other, including from the left: preprocessing, segmentation, registration, erosion detection and erosion quantification. To increase the visibility of each steps contribution to the process, only a single joint is presented in the figure, however, the method processes an entire dataset at a time.

The first step of the proposed method is denoted as preprocessing, and concerns initializing of the datasets. The main responsibilities of the preprocessing is to load datasets, data format convergence and appliance of image enhancement methods.

The proposed method for erosion detection is based upon the usage of the periosteal surface of the bone joints to detect erosions, by searching for cortical breaks. This approach was selected, as earlier work within the area of automatic and semi-automatic erosion detection and quantification in HR-pQCT images [5, 4], yielded promising results by the use of this approach. To accomplish this approach, a clear isolation of the periosteal surface is necessary. Because of this, a segmentation step is required, and introduced in the proposed method. As a result of this segmentation a clear binary separation of the periosteal surface is achieved, as seen in fig. 3.4.

Because of the patient motion, a misalignment in each joint for every 110 image slices is present. In addition, due to the stochastic nature of the patient motion, each joint is not affected by the same misalignment transformation. This challenge introduces the third step of the proposed method, namely registration with the responsibility of realigning the joints. Typically registration is a preprocessing step performed before further segmentation and analysis, but because of the specific registration problem in this study, the registration is carried out after the segmentation. The reason for this is that the registration needed, is an individual registration of each joint. Therefore, a clear separation of each joint is necessary, thereby explaining the decision of placing the registration step after segmentation.

The fourth and fifth step of the proposed method is the actual erosion detection and erosion quantification. The responsibilities of these steps is to detect all erosions in a given dataset, and quantify a set of properties related to each erosion. The properties include width, depth, volume and centroid, which is important in order to evaluate the prognosis and diagnosis of RA. Each of the proposed method steps are further described in details in the following sections.

3.3 Preprocessing

The first step of the proposed method is the preprocessing. Preprocessing defines the process of applying initial methods and algorithms to the data, with the goal of creating a better starting point for the future steps and processing. Preprocessing may include many different methods e.g. image enhancement and image manipulation.

Image enhancement is the process of enhancing the image information, making it easier for further algorithms and methods to comprehend the image. Image enhancement in medical images may include intensity scaling, noise reduction, artifact reduction and edge enhancement [46].

Intensity scaling is the process of scaling the range of the intensity values to a wider range of intensities. This process is capable of increasing the performance of both the Human Visual System (HVS) or computational analysis of the images, as otherwise hidden intensity details are revealed.

Noise reduction is a large subject within medical image processing, and is generally concerned with the reduction of noise artifacts that hinders further image analysis. The complexity and effect of medical image noise reduction, is also varying from the simpler filter e.g. mean, median and Gaussian [46], to the more complex image filters e.g. adaptive, frequency domain and hybrid methods [46]. The main challenge involved with medical image noise reduction, is to reduce image noise, without reducing the wanted image information.

Artifact reduction is also an image enhancement process as artifacts typically reduce the local image quality. Different processes exist for artifact reduction or removal, each concerning individual types of artifacts. Similar to noise reduction, considerations regarding the effect of eventual image information reduction should be taken.

Edge enhancement is the process of enhancing the borders and edges of the objects present in the images. The process is capable of boosting the performance of edge detection algorithms such as edge-based segmentation methods. A trade-off is concerned with edge enhancement as noise in the images also gets enhanced.

Another preprocessing step is image manipulation, which might be a necessity in order to process the medical images or make further processing simpler. Image manipulation could for instance be data type conversion, resampling or domain switch. Medical images are often stored in specific medical image data types like the Digital Imaging and Communications in Medicine (DICOM) standard. The DICOM standard contains both the image and associated medical information. Medical image data types, can also be of different sizes both signed or unsigned and between 8 and 32 bytes. Medical images may also consist of different channels from 1 grayscale, 3 RGB or several frequency channels. Data format conversion may be necessary to either display images or to make image computations less complex.

Image resampling is the process on resizing the image. Down-sampling reduces the amount of image pixels to be processed, and may therefore diminishes the overall computational time. However, important information present in the images might also be removed or suppressed.

Lastly, domain switch is the process of converting the domain of the image. This could for instance be a conversion from spatial to frequency domain, which enables the appliance of specific frequency methods.

For the proposed preprocessing method, it was considered utmost important to not risk the removal of information within the images. This decision was based upon the very limited amount of pixels required to change whether a cortical break exists or not. This limitation removes the use of many preprocessing techniques which might modify image information. This includes filtering, edge-enhancement and resampling. Therefore, the final proposed preprocessing method consists of the two steps illustrated on fig. 3.5.

The first step of the proposed preprocessing is lossless conversion for the original image datatype

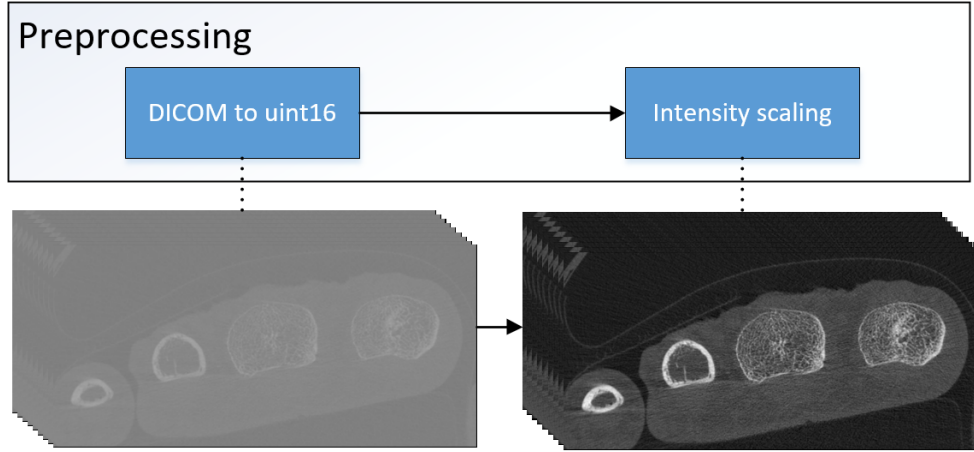


Figure 3.5: The internal steps of the preprocessing.

DICOM to an unsigned integer of 16 bits. This is done to extract the image data from the patient information, and convert to a data type which is feasible for further image processing. The second step of the preprocessing is intensity scaling.

3.3.1 Intensity Scaling

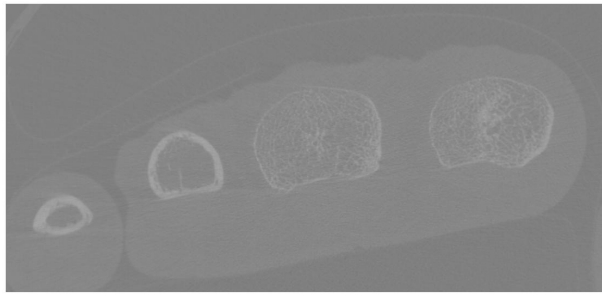
The second preprocessing step applied to the proposed method is intensity scaling, which is used to convert low contrast to high contrast images. Medical images are typically stored in pixel ranges of 2^n , but usually only use a narrow range of these pixel values. This also applies for the entire data used in this study. By looking at the image histogram and corresponding image on figs. 3.6a and 3.6c it is seen that the image histogram is very narrow and that the image therefore is hard to visually comprehend. By stretching the histogram values to the whole image range, otherwise hidden details may be uncovered to HVS as well as algorithms. Scaling of an image can be mathematically expressed using eq. (3.1) [46]:

$$\mathbf{I}_{scaled}(i, j) = (\mathbf{I}(i, j) - low_{in}) \cdot \frac{high_{out} - low_{out}}{high_{in} - low_{in}} + low_{out}, \quad (3.1)$$

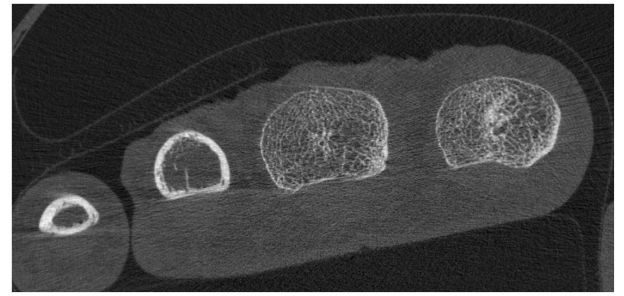
where $i \in 1, 2, \dots, M$ $j \in 1, 2, \dots, N$ of an $M \times N$ image \mathbf{I} , low_{in} is the minimum intensity value of the image \mathbf{I} , $high_{in}$ is the maximum intensity value of the image \mathbf{I} , low_{out} is the minimum intensity value of the output image \mathbf{I}_{scaled} and $high_{out}$ is the maximum intensity of the output image \mathbf{I}_{scaled} . A representation of intensity scaling is seen in figs. 3.6b and 3.6d.

Image artifacts in medical images might have varying maximum and minimum intensities, especially in the case of ring artifacts, which can produce both low and high contrast intensities. Because of this, a dataset might be scaled differently, thereby having different intensities for the same image objects. Duo to this, all images within a dataset needs to be scaled equally. This is done by finding the median of the lowest intensity values in all images in the given dataset, and the median of the highest intensity values in a dataset, and scale all images in the dataset accordingly to these medians. The median is selected instead of the mean, to counter eventually disruption from outliers.

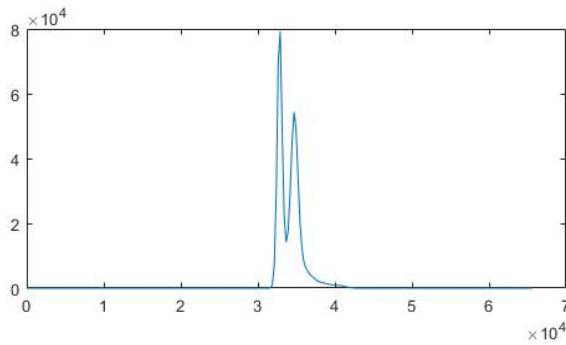
The algorithm for the intensity scaling is explained in alg. 1. Firstly, the minimum and maximum for each image is found and stored in min_{all} and max_{all} , where an image dataset is represented in size $M \times N \times O$. The median of the min_{all} and max_{all} is found and stored as low_{in} and $high_{in}$. Next the image is scaled using equation eq. (3.1), where low_{out} and $high_{out}$ represent the wanted intensity range. If the intensity value is outside the bounds of low_{in} and $high_{in}$ they are set to low_{out} and $high_{out}$



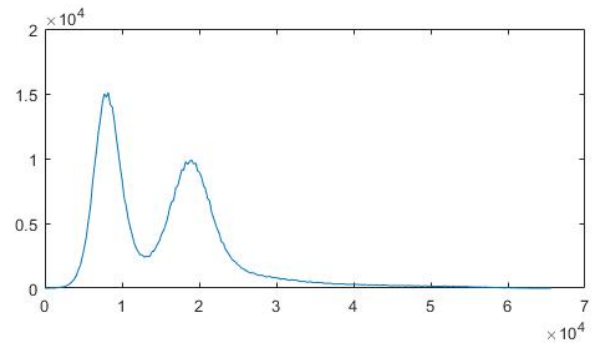
(a) Unscaled image.



(b) Scaled image.



(c) Histogram of unscaled image.



(d) Histogram of scaled image.

Figure 3.6: Figure 3.6a is the original received image, fig. 3.6c is the histogram of fig. 3.6a, fig. 3.6b is the intensity scaled version of fig. 3.6a and fig. 3.6d is the histogram of fig. 3.6b.

respectively, in order to scale the images equally.

3.4 Segmentation

The second step of the proposed method is segmentation. Image segmentation is a large subject addressing separation of ROI from the remaining image. Medical image segmentation is an essential analysis tool, which is a prerequisite for other medical image methods e.g. feature extraction, image measurements and image display. This involves analyzing and specifying regions of anatomical structures such as muscles, bones and blood vessels or pathological regions such as tissue deformities, sclerosis lesions and cancer cells [46]. As image segmentation is used for various data types and the goal of the segmentation is inconsistent depending on the use case, no de facto segmentation technique is considered to be existing. The methods for image segmentation is also highly diverse, each with their own pros and cons. Following this, a description of the primary groupings of segmentation methods which have been under consideration for this study is provided below.

Thresholding-based Segmentation

Thresholding-based segmentation is the most simple and widest used segmentation category, especially for medical images [46]. Thresholding involves the process of segmentation by dividing the pixel intensities into different intervals. This is especially relevant for medical images like CT or MRI, where image objects typically are clearly divided into pixel intensities. The main challenge for thresholding-based segmentation methods, is to find the optimal threshold value for the given ROI. For a clearly defined bimodal image, as seen in fig. 3.7a, the threshold dividing the image in structure and back-

Algorithm 1: Intensity Scaling

```

for  $k = 1$  to  $O$  do
  for  $i = 1$  to  $M$  do
    for  $j = 1$  to  $N$  do
       $\min_{all}(k) = \min(\text{dataset}(i, j, k));$ 
       $\max_{all}(k) = \max(\text{dataset}(i, j, k));$ 
    end
  end
end
 $low_{in} = \text{median}(\min_{all});$ 
 $high_{in} = \text{median}(\max_{all});$ 
for  $k = 1$  to  $O$  do
  for  $i = 1$  to  $M$  do
    for  $j = 1$  to  $N$  do
      if  $\text{dataset}(i, j, k) < low_{in}$  then
         $\text{dataset}(i, j, k) = low_{out};$ 
      else if  $\text{dataset} > high_{in}$  then
         $\text{dataset}(i, j, k) = high_{out};$ 
      else
         $\text{dataset}(i, j, k) = (\text{dataset}(i, j, k) - low_{in}) \cdot \frac{high_{out} - low_{out}}{high_{in} - low_{in}} + low_{out};$ 
      end
    end
  end
end

```

ground is found with ease. On the contrary, if an image is not bimodal, as seen in fig. 3.7b, finding one or multiple threshold values is often considered challenging, especially for images containing noise, low contrast object edges or artifacts.

Many different thresholding methods exists, which can be divided into six groups according to [47]. Histogram shape-based methods analyze the histogram of the image by looking at the curvature. Clustering-based methods clusters the image into foreground and background, based on the gray level intensities and Gaussian models. Entropy-based methods attempts to maximize the information according to background and foreground regions. Object attribute-based methods finds and groups similar objects based on edges or shapes. Spatial methods use high order probability distributions or pixel correlations. Lastly, local methods utilizes smaller local characteristics to define the local threshold [47]. Thresholding based segmentation is, despite the large number of methods and high use, subject to failure in the presence of inhomogeneity, noise and artifacts.

Edge-based Segmentation

Edge-based segmentation methods use information about image gradient to divide the image into objects. The gradient of an image is defined as an approximation of the first order derivative of the images function [46]. The most common gradient calculators are Sobel [48], Roberts [49] and Prewitt [50], which are all based on convolutions. Such a convolution could be weighted summations of local neighboring pixels intensities. These weights are listed by arrays in a form corresponding to the local neighborhood of the image.

Regularly, a threshold operation as described above, is performed on the gradient to determine if an edge is present or not. This results in a binary image, representing edges present in the image. The

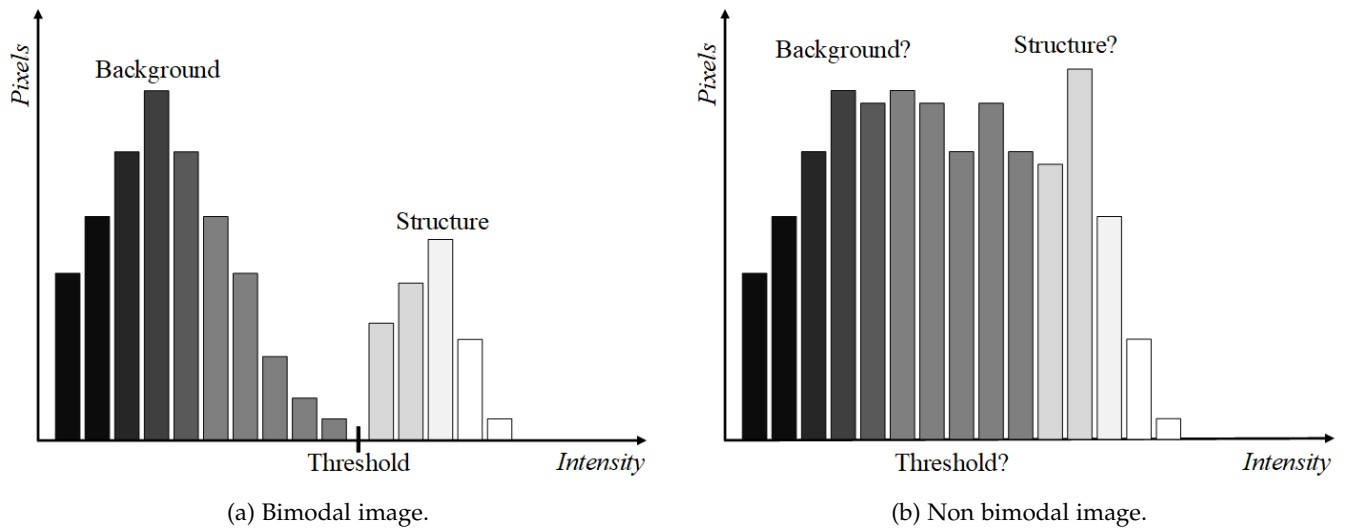


Figure 3.7: Threshold value selection difficulties for a non bimodal image.

difficult part of edge-based thresholding is to select the appropriate threshold, enabling the inclusion of correct edges and exclude noise and artifacts. The simple gradient-based approach is computationally fast and simple, but has the common problem of discontinuous edge borders [46]. Typically postprocessing steps including edge linking and grouping is used, however, these are generally computationally expensive and unreliable [46]. Some edge-based methods mention the demand of both pre- and post-processes in combination with the edge segmentation operation itself, to achieve correct edge detection [51, 52]. Edge-based segmentation is especially useful in scenarios where the images have clear distinguishable borders and edges.

Active Contour-based Segmentation

Active Contour-based segmentation is a prominent image processing technique. The technique utilizes a confluence of geometry, physics and approximation theory in its mathematical foundation. Active contours are often referred to as *deformable models*, *active surfaces* and *snakes*. The generic approach is based on closed smooth spline curves, also referred to as *snakes*, moving towards a given object contour, as illustrated on fig. 3.8. This concept is called evolution and is based on an optimization, influenced by two separate types of forces. The first forces are external, originating from the image data, and pull the snakes towards the object contour. The second forces are internal and are used to maintain smoothness in the resulting contour by resisting deformations.

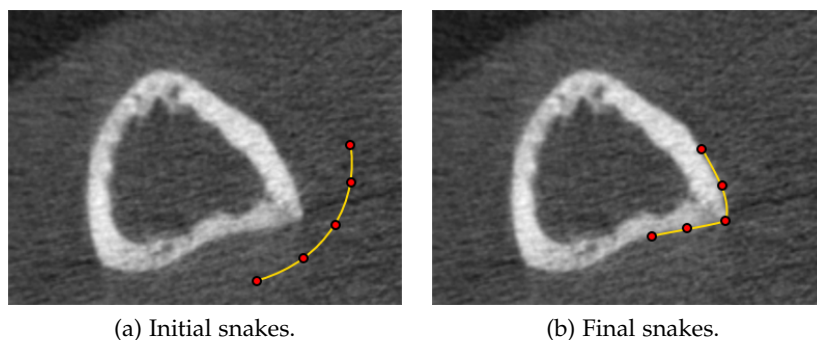


Figure 3.8: Illustration of snakes evolved towards object contour.

In general, active contour methods can be grouped into two groups, namely parametric and geometric. Geometric active contours are equal to parametric, as they both are based on curve evolution. However, they differ in that geometric active contours utilizes level set methods. The initial evolved contour can either be created manually or automatically, but has a huge impact on the final result of the active contour. Active contour methods can both be used for standalone segmentation, or as border refinement solutions. However, the method is considered very computational complex, which is highly dependable on the initial contour and image resolution.

Region-based Segmentation

Region-based segmentation uses neighboring pixel characteristics to segment images. The process typically starts with a point or a group of points called the seed. Based on the characteristics of the seed values e.g. pixel intensity characteristics, the seed grows, thereby including new neighboring pixels into the seed with similar characteristics. The choice for inclusion of a pixel, is called the homogeneity criterion, and can be based on e.g. pixel intensities, pixel mean or pixel variance. The region grow is an iterative process which stops, when no more neighboring pixels can be added to the growing region. The region-based segmentation is good for segmenting single similar characteristic objects within an image. Problems associated with region-based segmentation, is the selection of the initial seed point, which typically is performed manually. Another problem is the proper choice and setup of the homogeneity criterion, which if not selected correctly, results in inclusion or exclusion of areas and pixels respectively outside or inside the ROI [46].

Classification-based Segmentation

Classification-based segmentation techniques utilizes a set of features to segment a relevant objects. This is done using pattern recognition techniques, on the set of features, with associated labels. These features could for instance include pixel intensities, spatial properties, texture measures and gradients. Two overall classification techniques exist, namely supervised and unsupervised.

Supervised classification is initialized by manual feature selection. These manual feature labels are considered the golden truth, and are used to train the algorithm. The trained algorithm can then be used to segment images by extracting features similar to the training features. Supervised classification techniques are split into two sub categories, namely parametric and non-parametric [53]. Parametric classification utilizes maximum likelihood estimations to perform the segmentation. Non-parametric requires no prior knowledge regarding the data. Instead, a series of methods can be used in the classification, such as; k-nearest neighborhood, decision tree theory or minimum distance classifiers [53].

Unsupervised classification does not need initialization. Instead, it composes data containing equal or similar features into groups. When grouping is completed, manual labeling of the generated groups is needed to be able to identify these.

Classification-based segmentation is good in scenarios where objects are describable through the same set of indistinguishable features. However, supervised classification does require a comprehensive training process to ensure robustness. Unsupervised classification in contrast does not require any training, but may have a low robustness.

3.4.1 Challenges in HR-pQCT Segmentation

Medical image segmentation is considered a critical and challenging subject. Due to challenges in medical images typical segmentation methods might be inconsistent. Three key challenges are often found in CT images, as defined by Truc et al. [54], which are inhomogeneous bone structures, low-contrast edges and overlapping intensity values of bones. These three challenges are all applicable for the HR-pQCT data used in this study.

The inhomogeneous bone structures are a result of the nature of the joint bones. This means that the contour of the ROI can change drastically between slices, implying the need of a method capable of segmenting different shaped objects. Examples of the different shapes of contour present in the HR-pQCT data used, are seen in fig. 3.9.

Gaps and low-contrast edges as seen on figs. 3.9b to 3.9d, are often due to low cortical thickness and image artifacts. This makes it difficult for a segmentation method to create a fully closed contour of the ROI.

The last challenge is overlapping intensity values as seen on fig. 3.9a, which is a result of bones close to each other, thereby making their border intensities diffused [54]. This is often seen in the MCP joint shifts. This calls for a segmentation method capable of distinguishing diffused objects.

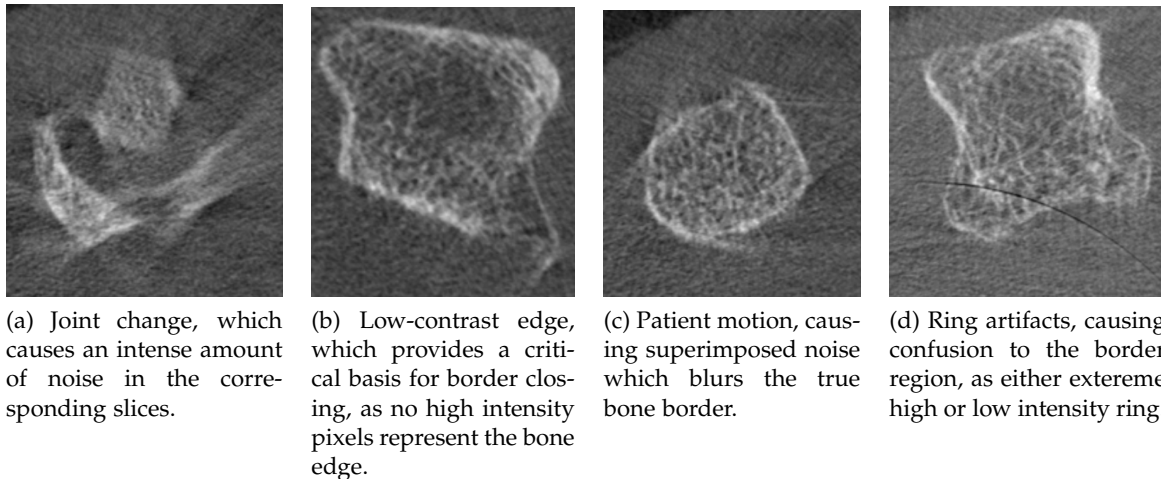


Figure 3.9: Selected examples of HR-pQCT images, representing common challenges for medical image segmentation.

3.4.2 Proposed Segmentation Method

The proposed segmentation method is a hybrid method. Because of the challenges in medical image segmentation, as presented section 3.4.1, a single segmentation method, as presented in section 3.4, is not precise nor accurate enough. Several of the standalone methods have been studied, but none had the ability to properly segment the joints. Thresholding methods have difficulties in adequate segmentation of the whole periosteal surface, without introducing a vast amount of noise and artifacts. The edge based methods are likewise not capable of segmenting the periosteal border because of low contrast edges. Active contour-based methods showed promising results, but if the initial contour was imprecise the computational complexity of the algorithms was undesirably high. Region-based methods shows the same problems as for the threshold-based methods, because of the large intensity difference in the periosteal surface, which in turn will lead to high noise and artifact presence. Lastly, the classification-based methods requires a large amount of learning features, which was not available for this study, and deemed to time consuming.

Based on the research within the field of RA, HR-pQCT and image processing, many authors use the segmentation software Image Processing Language (IPL) developed by the scanner manufacturer Scanco Medical AG [11, 45, 55, 56, 57, 58, 59, 60, 41]. This software was not available for this study. Some studies use a hybrid segmentation method [4], originally developed for segmentation of bone in volumetric computed tomography [61]. Based on the paper by Kang et al. [61], their proposed method was not interpretable, and there was no source code available, which meant that their method could not be tested. This led to the proposed hybrid segmentation method for this study, which is based on some of the same principles as in [61]. The proposed method consists of three overall steps, as seen in fig. 3.10.

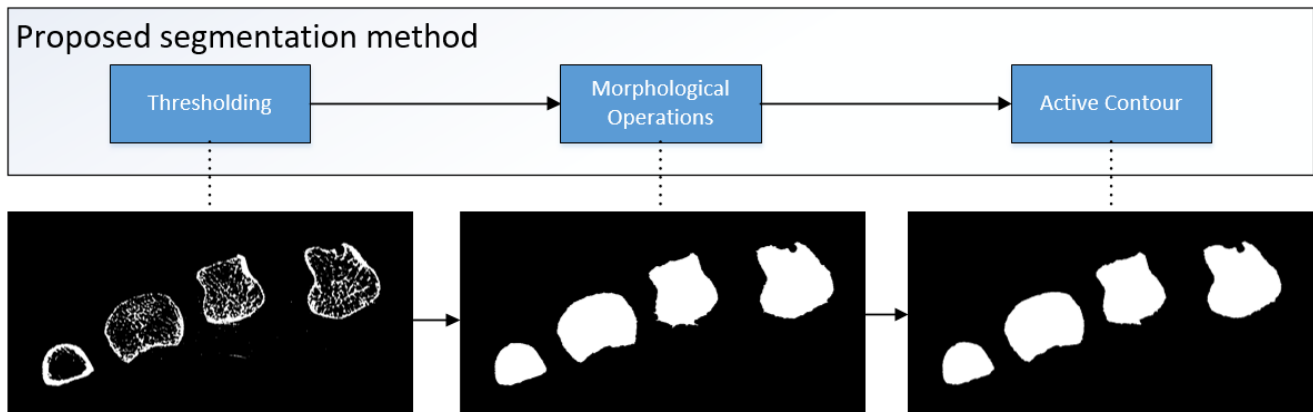


Figure 3.10: A step by step illustration of the three steps contained in the proposed hybrid segmentation method.

The first part of the proposed hybrid method is thresholding. In this step the images are thresholded and an initial non closed binary masks of the bone structures are obtained. Following this the binary mask is closed and filled using morphological operations. Because of the behavior of the closing by the morphological operations, small cavities and details in the periosteal surface is filled or removed, which also means possible erosions is in the risk of disappearing. The last step of the method is to use an active contour method to refine the border of the binary mask, thereby uncovering the else hidden information and erosions in the periosteal surface. The reason for not using only an active contour-based methods, is because of their high computational complexity, which would result in an extremely high processing time for the segmentation method.

3.4.3 Thresholding

The first part of the proposed hybrid segmentation method is thresholding. Through initial analysis, thresholding alone was not an option for segmentation of the entire periosteal surface, as these techniques could not capture all of the structures without including false elements. The purpose of the thresholding step is to create a starting basis for the segmentation, which will be fully closed by the appliance of other methods. The needed thresholding method shall to the best of its ability only include true representations of the bone joints, with as little as possible inclusion of false segmentation. As described in section 3.4 a vast amount of thresholding methods exists. These methods can be divided into several groupings. Thresholding methods are primarily not developed for medical images, which makes the process of selecting a fitting methods nontrivial. As the methods cannot be selected based on their mathematical properties, a further analysis through experiments is needed to select the best solution. For this study, four different thresholding methods are selected for further analysis. These methods are selected, as they each represent a specific thresholding category and showed promising results through initial tests.

Three of the methods calculates a single global threshold value t , based on the image $\mathbf{I}(i, j)$. This value is used to calculate a binary image $\mathbf{B}(i, j)$, according to eq. (3.2):

$$\mathbf{B}(i, j) = \begin{cases} 1 & \text{if } \mathbf{I}(i, j) > t \\ 0 & \text{if } \mathbf{I}(i, j) \leq t \end{cases} \quad (3.2)$$

where, $i \in 1, 2, \dots, M$ $j \in 1, 2, \dots, N$ and $M \times N$ is the size of the image \mathbf{I} . The fourth method presented utilizes a local adaptive thresholding approach which creates a thresholding value for each individual pixel in the image.

Gaussian characteristic thresholding

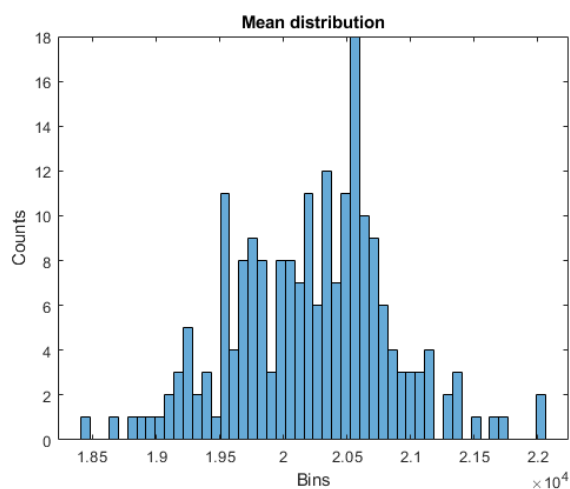
The first thresholding approach is developed specifically for this study, and utilizes the characteristics of the HR-pQCT datasets. As presented in section 3.1 the images can be modelled as a combination of two distinct Gaussian distributions, which represent the image border and the tissue. All pixel intensities above these distributions are considered bone structure. A simple approach to the thresholding would be to specify a constant thresholding value above the two Gaussian distributions, and then threshold all images accordingly to this value. The Gaussian distributions might change their mean and standard deviation, which in turn would produce unsatisfying thresholding results.

The idea behind the presented approach is to use the information of the Gaussian distributions to select the threshold value. The Gaussian distributions can be expressed as the summation of the two Gaussian distributions as seen in eq. (3.3):

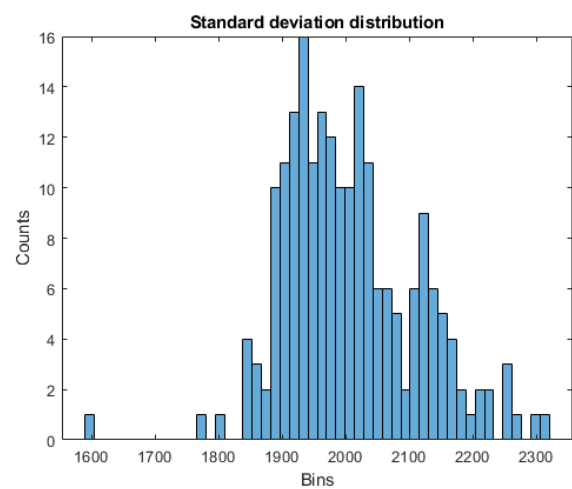
$$y(x) = A_1 \cdot e^{-\left(\frac{x-\mu_1}{2\sigma_1}\right)^2} + A_2 \cdot e^{-\left(\frac{x-\mu_2}{2\sigma_2}\right)^2}, \quad (3.3)$$

where A_1 and A_2 are the heights of the two Gaussian distributions respectively, the means of the Gaussian distributions are μ_1 and μ_2 respectively and σ_1 and σ_2 are the standard deviations of the Gaussian distributions respectively.

An experiment was carried out to investigate the distribution of the mean and standard deviation of the second Gaussian in all datasets. The results are seen in fig. 3.11.



(a) Histogram of the mean of the second Gaussian.



(b) Histogram of the standard deviation of the second Gaussian.

Figure 3.11: The histogram of the mean and standard deviation of all datasets.

It is seen in the variation of means and standard deviations throughout the entire datasets, that

a single thresholding value cannot be selected, thereby proving the presented approach. By using a fitting operation, the values for the two distributions can be found. The threshold value is then calculated as eq. (3.4):

$$t = \mu_2 + 3.5 \cdot \sigma_2. \quad (3.4)$$

The choice of $3.5 \cdot \sigma_2$, was selected because the threshold value then passes the 0.999 confidence interval of the right most Gaussian distribution. This implies that eventual noise from the right most Gaussian distribution is avoided.

Algorithm 2: Gaussian characteristic thresholding

```
[f, bins] = histogram(dataset, nr_bins);
[A1, μ1, σ1, A2, μ2, σ2] = fit(f);
t = μ2 + 3.5 · σ2;
```

The algorithm for the Gaussian characteristic thresholding is seen in alg. 2. First a histogram for the entire dataset is calculated with the number of bins as specified in nr_{bins} . The result of the histogram is the bin widths $bins$ and the counts per bin f . The characteristics of the Gaussian models are then calculated, using a fitting algorithm which is from the the MATLAB Curve Fitting Toolbox [32] called *fit* [62]. Lastly the threshold is calculated.

Entropy thresholding

Another approach for selecting the best threshold value is using information theory. One entropy method [63] based upon the entropy of the image histogram is selected for analysis. Based on the histogram of the image the individual gray-level probabilities can be calculated using the observed frequencies f_1, f_2, \dots, f_n , as seen in eq. (3.5) [64]:

$$p_i = \frac{f_i}{N}, \quad \sum_{i=1}^n f_i = N, \quad i = 1, 2, \dots, n, \quad (3.5)$$

where N is the total amount of pixels in the image, and n is the number of gray-levels. Using the probabilities the total entropy H_T of the image can be calculated using eq. (3.6) [64]:

$$H_T = - \sum_{i=1}^n p_i \ln(p_i). \quad (3.6)$$

Treating the image as bimodal, it can be divided into two distributions, the background and the structure. The two models are divided at the point t . The individual probability sums $P_A(t)$ and $P_B(t)$ of the two distributions A and B are given by eq. (3.7) [64]:

$$P_A(t) = \sum_{i=1}^t p_i, \quad P_B(t) = 1 - P_A(t). \quad (3.7)$$

Let H_S be formulates as eq. (3.8) [64]:

$$H_S(t) = - \sum_{i=1}^t p_i \ln(p_i). \quad (3.8)$$

Then each of the distributions can be modeled with their own entropies, which are given by eqs. (3.9) and (3.10) [64]:

$$H_A(t) = \ln(P_A(t)) + \frac{H_S(t)}{P_A(t)}, \quad (3.9)$$

$$H_B(t) = \ln(P_B(t)) + \frac{H_T - H_S(t)}{P_B(t)}. \quad (3.10)$$

The combined entropy is then given by eq. (3.11) [64]:

$$\psi(t) = H_A(t) + H_B(t) = \ln(P_A(t) \cdot P_B(t)) + \frac{H_S(t)}{P_A(t)} + \frac{H_T - H_S(t)}{P_B(t)}. \quad (3.11)$$

By maximizing $\psi(t)$ the information between the background and the structure is likewise maximized. The optimum threshold value t^* is therefore found at the maximum, as given by eq. (3.12) [64]:

$$t^* = \arg \max_{t \in n} (\psi(t)), \quad (3.12)$$

where n is the set of gray levels. The Entropy thresholding as presented above, calculates the threshold for a histogram with two distributions. This can be further expanded into several distributions, thereby including several threshold values to be searched for. For the Entropy method used in this study, the histogram is assumed to have 3 distributions.

The algorithm for the entropy thresholding is seen in alg. 3. First a image histogram is created to find the frequencies of the grayscale values. The number of bins in the histogram is specified through the nr_{bins} parameter. The histogram returns two vectors, one with the bin ranges and one with the frequencies. The frequencies are then divided with the cumulative sum of the frequencies to obtain the probabilities.

Algorithm 3: Entropy thresholding

```

[f, bins] = histogram(image, nrbins);
f = f / sum(f);
fmax = max(f);
fmin = min(f);
HT = 0;
for i = fmin to fmax do
    | HT = HT + f(i) · ln(f(i));
end
PA = 0;
HS = 0;
for i = fmin to fmax do
    | PA = PA + f(i);
    | PB = 1 - PA;
    | HS = HS + f(i) · ln(f(i));
    | co(i) = ln(PA + PB) -  $\frac{H_S}{H_P}$  +  $\frac{H_S - H_T}{P_A}$ ;
end
comax = max(co);
coIdx = find(comax, co);
t = bins(coIdx);

```

The range of the frequencies are found through the min and max algorithms. The total entropy is calculated through a for loop.

Hereafter, a for-loop calculates all possible informations. The for-loop loops through all probabilities, and increments the A distributions cumulated probability along with H_S . The combined information is then calculated. After the for-loop, the maximum combined information is found along with its index in the gray-levels. This index corresponds to the threshold value.

Otsu thresholding

The Otsu thresholding is a clustering-based thresholding method. The clustering approach tries to divide the image histogram and characteristics into regions, thereby determining the optimal threshold. The most commonly used clustering technique is by Otsu [65]. The individual gray-level probabilities p_i can be calculated using eq. (3.13) [65]:

$$p_i = \frac{f_i}{N}, \quad \sum_{i=1}^n f_i = N, \quad i = 1, 2, \dots, n, \quad (3.13)$$

where f_i is the individual representations of the gray-levels from the image histogram, N is the total number of pixels in the image, and n is the total number of gray-levels. Supposing the image histogram can be divided into two distributions the individual probabilities $\omega_0(t)$ and $\omega_1(t)$ for the two distributions can be calculates as eqs. (3.14) and (3.15) [65]:

$$\omega_0(t) = \sum_{i=0}^t p_i, \quad (3.14)$$

$$\omega_1(t) = \sum_{i=t+1}^n p_i. \quad (3.15)$$

The individual distributions means $\mu_0(t)$ and $\mu_1(t)$ can be calculated as eqs. (3.16) and (3.17) [65]:

$$\mu_0(t) = \sum_{i=0}^t i \cdot \frac{p_i}{\omega_0(t)}, \quad (3.16)$$

$$\mu_1(t) = \sum_{i=t+1}^n i \cdot \frac{p_i}{\omega_1(t)}, \quad (3.17)$$

with a combined mean eq. (3.18) [65]:

$$\mu_T = \sum_{i=1}^n i \cdot p_i. \quad (3.18)$$

The individual variances are calculated as eqs. (3.19) and (3.20) [65]:

$$\sigma_0^2(t) = \sum_{i=1}^t (i - \mu_0(t))^2 \cdot \frac{p_i}{\omega_0(t)}, \quad (3.19)$$

$$\sigma_1^2(t) = \sum_{i=t+1}^n (i - \mu_1(t))^2 \cdot \frac{p_i}{\omega_1(t)}. \quad (3.20)$$

The total variance can be described as a sum of two variances as seen in eq. (3.21) [65]:

$$\sigma_T^2(t) = \sigma_{WCV}^2(t) + \sigma_{BCV}^2(t). \quad (3.21)$$

The within-class variance (WCV) $\sigma_{WCV}^2(t)$ can be described as eq. (3.22) [65]:

$$\sigma_{WCV}^2(t) = \omega_0(t) \cdot \sigma_0^2(t) + \omega_1(t) \cdot \sigma_1^2(t). \quad (3.22)$$

Likewise, the between-class variance (BCV) $\sigma_{BCV}^2(t)$ can be described as eq. (3.23) [64]:

$$\sigma_{BCV}^2(t) = \omega_0(t) \cdot (\mu_0(t) - \mu_T)^2 + \omega_1(t) \cdot (\mu_1(t) - \mu_T)^2. \quad (3.23)$$

Based on these class variances, the optimal threshold t^* can be found by minimizing the WCV or maximizing the BCV. As the BCV is less computationally expensive, as the variances does not need to be calculated, this is usually maximized as seen in eq. (3.24) [65].

$$t^* = \arg \max_{t \in n} (\sigma_{BCV}^2(t)). \quad (3.24)$$

The Otsu thresholding, as presented above, calculates the threshold for a histogram with two distributions. This can be further expanded into several distributions, thereby including several threshold values to be searched for. For the Otsu method used in this study, the histogram is assumed to have 3 distributions.

Algorithm 4: Otsu thresholding

```

[f, bins] = histogram(image, nr_bins);
f = f / sum(f);
fmax = max(f);
fmin = min(f);
for i = fmin to fmax do
    |  $\mu_T = i \cdot f(i)$ ;
end
 $\omega_{0prev} = \omega_0 = 0$ ;
 $\mu_0 = \mu_1 = 0$ ;
for i = fmin to fmax do
    |  $\omega_0 = \omega_0 + f(i)$ ;
    |  $\omega_1 = 1 - \omega_0$ ;
    |  $\mu_0 = (\omega_{0prev} \cdot \mu_0 + f(i) \cdot i) / \omega_0$ ;
    | for j = i to fmax do
    | |  $\mu_1 = \mu_1 + j \cdot f(j) / \omega_1$ ;
    | end
    |  $BCV(i) = \omega_0 \cdot (\mu_0 - \mu_T) + \omega_1 \cdot (\mu_1 - \mu_T)$ ;
    |  $\omega_{0prev} = \omega_0$ 
end
 $BCV_{max} = \max(BCV)$ ;
 $BCV_{Idx} = \text{find}(BCV_{max}, BCV)$ ;
t = bins(BVCIdx);

```

Seen in alg. 4 is the Otsu thresholding algorithm, which starts with finding an image histogram where the parameter *nr_bins* specifies the number of bins in the histogram. The return values of the histogram is the *bins*, which is the bin ranges, and *f* which is the number of counts for each bin range. The bin counts are divided with its sum to get the probabilities for each bin. The range of the probabilities are found through the functions min and max. Next, the mean for all probabilities are found though a for-loop. The following for-loop calculates all BCV values for all probabilities. The cumulative probabilities for each distribution is calculated along with each distributions mean for each probability in the histogram. Based on these values the BCV is calculated. After the for-loop,

the maximum BCV value is found along with its associated index in the f vector. This index is then used to find the corresponding value in the bin range vector, which then correspond to the optimum threshold value.

Niblack local adaptive thresholding

The locally adaptive thresholding methods take another approach to thresholding, as the methods presented above. The term locally indicates that the approach utilizes local statistics to compute a local threshold for each pixel. One of the first methods using this approach, which showed promising results in initial testing, was presented by Niblack [66]. The methods is seen in eq. (3.25) [47]:

$$\mathbf{T}(i, j) = \mu(i, j) + k \cdot \sigma(i, j), \quad (3.25)$$

where k is a bias constant, typically set to -0.2 [47], $i \in 1, 2, \dots, M$ $j \in 1, 2, \dots, N$ and $M \times N$ is the size of the image \mathbf{I} . The local mean $\mu(i, j)$ and local standard deviation $\sigma(i, j)$ is calculated as eqs. (3.26) and (3.27) [66]:

$$\mu(i, j) = \frac{1}{K \cdot L} \sum_{k=-K}^K \sum_{l=-L}^L \mathbf{I}(i+k, j+l), \quad (3.26)$$

$$\sigma(i, j) = \sqrt{\frac{1}{K \cdot L} \sum_{k=-K}^K \sum_{l=-L}^L (\mathbf{I}(i+k, j+l) - \mu(i, j))^2}, \quad (3.27)$$

where, $k \in -K, \dots, K$ $l \in -L, \dots, L$ and $K \times L$ is the size of a local window. The thresholding is then produced using eq. (3.28):

$$\mathbf{B}(i, j) = \begin{cases} 1 & \text{if } \mathbf{I}(i, j) > \mathbf{T}(i, j) \\ 0 & \text{if } \mathbf{I}(i, j) \leq \mathbf{T}(i, j), \end{cases} \quad (3.28)$$

where $\mathbf{B}(i, j)$ is the resulting binary image.

The algorithm for the Niblack thresholding is seen in alg. 5. The algorithm calculates a specific thresholding value for each pixel in the image of the size $M \times N$. For each pixel, the local mean and variance is also calculated, which is done though two separate double for-loops, each in an area specified by the window size of $K \times L$. The result of the algorithm is a matrix of the same size as the image, which can be used to threshold. The algorithm presented does not account for border errors and padding.

Algorithm 5: Niblack thresholding

```

for  $i = 1$  to  $M$  do
  for  $j = 1$  to  $N$  do
     $\mu(i, j) = 0$ ;
    for  $k = -K$  to  $K$  do
      for  $l = -L$  to  $L$  do
         $\mu(i, j) = \mu(i, j) + I(i + k, j + l) / (K \cdot L)$ 
      end
    end
     $\sigma(i, j) = 0$ ;
    for  $k = -K$  to  $K$  do
      for  $l = -L$  to  $L$  do
         $\sigma(i, j) = \sigma(i, j) + (I(i + k, j + l) - \mu(i, j))^2 / (K \cdot L)$ ;
      end
    end
     $\sigma(i, j) = \sqrt{\sigma(i, j)}$ ;
     $T(i, j) = \mu(i, j) + k \cdot \sigma(i, j)$ ;
  end
end

```

3.4.4 Morphological Operations

The initial thresholding segmentation method presented in section 3.4.3 yields non-closed contours, as a result of the varying pixel intensities of the ROI. A category of mature and recognized methods, capable of closing and cleaning up such masks, are morphological operations. Morphological operations describe a set of commonly used operations within mathematical morphology, which forms the foundation of morphological image processing. Morphological operations are recognized for their usability in clearing up unfinished segmentations, where they are used to either add pixels that are intended to close segmentation masks or to remove undesired pixels. The operations are applicable for transformation of both binary and grayscale images according to geometrical and topological concepts such as shape, size, connectivity, distance and convexity. The basic idea behind morphological operations is to gradually shift a structuring element, defined by a matrix mask, on the image. The four most widely used morphological operations are erosion, dilation, opening and closing, each producing a specific result.

Structuring elements

Two overall types of structuring elements exist, namely *flat* and *non-flat*. In this study, only flat structuring elements are used.

Flat structuring elements are based on either 2D or 3D binary valued neighborhoods. As shown in the example on fig. 3.12, the *true* pixels of the structure are included in the morphological computation, whereas the *false* are not.

The example provided in fig. 3.12 are of the shape type *cross*. However structuring elements can be formed in various shapes e.g. disk, line, rectangle for 2D and e.g. sphere and cube for 3D.

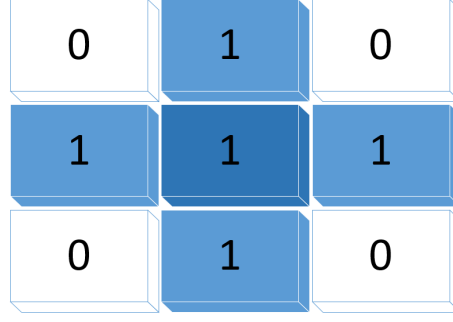


Figure 3.12: Examples of a flat structuring element. The dark blue center block represent the center pixel of which the morphological operations is originated in.

Erosion

Erosion operations, represented as \ominus , are used to thin lines or shrink objects in images, as shown in fig. 3.13a, where the original square is eroded using a disk structuring element. The operation combines two sets using the vector subtraction of set elements, and is given by eq. (3.29) [67]:

$$\mathbf{A} \ominus \mathbf{B} = \{x \in \mathbf{E}^N | x + b \in \mathbf{A} \text{ for every } b \in \mathbf{B}\}, \quad (3.29)$$

where \mathbf{A} is the binary image, \mathbf{B} is the structuring element and \mathbf{E}^N is the euclidean space of dimension N where \mathbf{A} and \mathbf{B} are subsets with elements $a = (a_1, \dots, a_N)$ and $b = (b_1, \dots, b_N)$ of N -tuples of element coordinates.

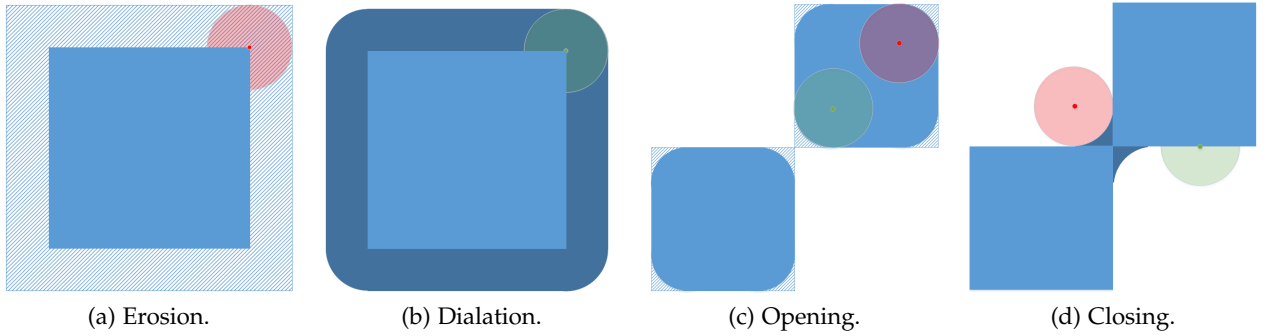


Figure 3.13: Visualization of the basic MO. Striped light blue areas indicates removed objects, filled light blue represents remaining objects, and dark blue shows added areas after the operations. The structuring elements are in all cases disks, where red and green represents erosion and dilation operations respectively. Inspired by [68].

Dilation

The dilation operation is the morphological counterpart to erosion. Dilation, represented as \oplus , are used to thicken objects in the input image. An example of the dilation operation is seen on fig. 3.13b, where the original light blue square is expanded to the dark blue object. The operation combines two sets using vector addition of set elements, and using the definitions from eq. (3.29) it can be obtained by eq. (3.30) [67]:

$$\mathbf{A} \oplus \mathbf{B} = \{x \in \mathbf{E}^N | x = a + b \text{ for some } a \in \mathbf{A} \text{ and } b \in \mathbf{B}\}. \quad (3.30)$$

Opening

The opening operation is defined as the dilation of the erosion of an image. Opening, represented as \circ , can be used for morphological noise suppression or object separation. The operation removes objects smaller than the structuring elements from the foreground and removes them by adding them to the background. An example of the opening operation is seen on fig. 3.13c, where two connected objects, consisting of two squares, are first eroded using the red structuring element and hereafter dilated by the green disk. The open operation is defined as eq. (3.31) [67]:

$$\mathbf{A} \circ \mathbf{B} = (\mathbf{A} \ominus \mathbf{B}) \oplus \mathbf{B}. \quad (3.31)$$

Closing

The last of the basic morphological operations is the closing operation, which is the counterpart to the opening operation. Whereas opening removes noise by eliminating small objects, closing on the other hand removes small holes existing in objects, and connects otherwise unconnected objects. An example of closing is seen on fig. 3.13d, where the original light blue object is first dilated by the green disk structuring element. Following, an erosion of the red disk structuring element, leading to the union of the light blue object and the dark blue object, thereby connecting the two objects. The closing operation is given by eq. (3.32) [67]:

$$\mathbf{A} \bullet \mathbf{B} = (\mathbf{A} \oplus \mathbf{B}) \ominus \mathbf{B}. \quad (3.32)$$

Minimum object removal

Another operation similar to the morphological operation open is the minimum object removal. The morphological open operation removes objects of a certain size, however, it also disconnects larger objects, which is not always desired. The minimum object removal method only removes objects with sizes below a certain threshold, and can therefore be used as a noise suppression operation.

Proposed morphological method

The idea of the morphological operations, within the proposed segmentation method, is to create a fully closed contour of the joints, using the initial thresholding segmentation. The proposed morphological step can be decomposed into four substeps, as seen in fig. 3.14.

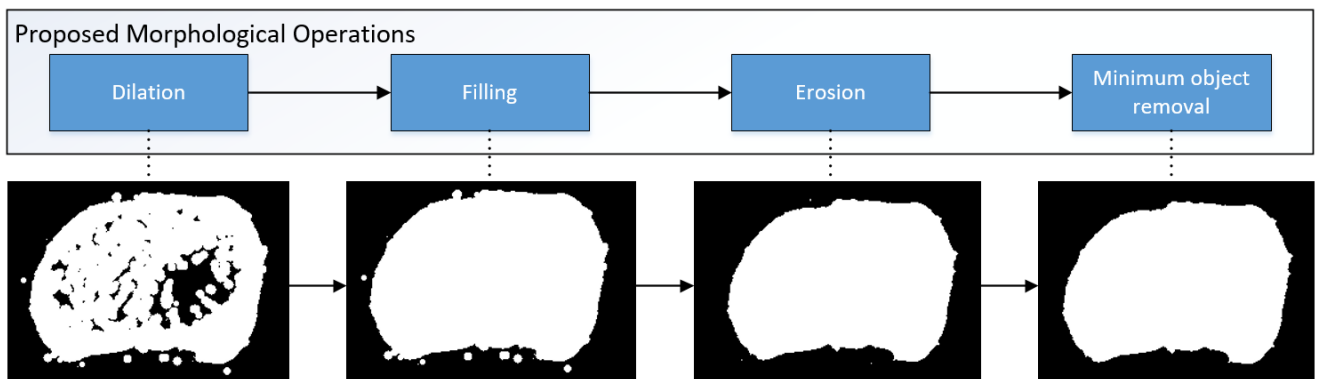


Figure 3.14: The four steps of the proposed morphological operations in the proposed segmentation method. Consist of, starting from the left: dilation, filling, erosion and minimum object removal. To increase the visibility of each steps individual contributions to the process, only a single joint is presented in the figure, however, the method processes an entire dataset at a time.

Firstly, a 3D morphological dilation operation is used to connect all elements in the joint contours, filling eventual open periosteal breaks. The dilation uses a morphological sphere structuring element. The dilation is carried out on three groupings of 110 image slices, in order to avoid over segmentation as a result of registration problems. Secondly, a 2D filling operation is used in the axial plane, thereby filling the entire closed bone structures. Thirdly, a 3D morphological erosion operation is used to obtain the original periosteal surface size. The erosion operation utilizes the same morphological structuring element and size as the dilation, along with the division in three 110 image slices. Lastly, a minimum object removal is used to remove small unconnected elements in the final contour, as these otherwise will represent noise. The optimum sizes for the radius of the sphere structuring element and the minimum object threshold cannot be calculated mathematically, and will therefore be found through experiments.

3.4.5 Active Contour

The second step of the proposed segmentation method, being the morphological operations, often results in an oversegmentation in the periosteal surface, because of the nature of the structuring element size. Therefore, a method is needed to refine the border of the periosteal surface. A mature well recognized method for such scenario is active contour-based segmentation.

As presented in section 3.4, active contour methods utilizes energies both external and internal to refine a contour.

Active contours are very computational expensive, when the initial contour deviates significantly from the true resulting contour. However, as the two initial steps, thresholding and MO, create a mask close to the desired result, the computational complexity of the active contour should be drastically lowered.

Various active contour-based segmentation methods exist, however, three different versions were analyzed, which are:

- Active Contours Without Edges (*Global CV*) [69]
- Localizing Region-Based Active Contours [70] including:
 - Chan-Vese based energy (*Local CV*)
 - Mean Separation based energy (*Local MS*)

The Active Contours Without Edges method, presented by Chan et al. [69] will hereafter be denoted as Global CV. This method was chosen due to its widely use and well resulting border refinement capabilities [70]. Global CV bases its contour evolution on global properties, making it fragile to noisy images, as noisy elements may interrupt the evolution.

Because of this, two other methods are selected, namely Local CV and Local MS. They are both based on widely used energy models, but only considers local properties in their curve evolution. This should theoretically make them more robust to noisy images as well as images where the ROI and the background shares same statistical models, as seen for the Gaussian distributed HR-pQCT images [70]. The two local methods are based on two different energy models. The reason for analyzing these, lies in the assumption that different energy models might yield different performances on the HR-pQCT images. The two models were chosen for their widely use [70].

Active contour methods are categorized in to parametric and geometric methods. To introduce the basic concepts behind active contours, parametric active contour models is first described following the various versions analyzed in this study.

Parametric Active Contours

Parametric active contours are based on the evolution of *snakes*, which can be described as closed spline curves, that are controlled continuously by different forces. The evolution of the curve contour \mathbf{C} , is based on minimization of two different energy types, namely internal energy E_{int} and external energy E_{ext} . The addition of these two energies, defines the total energy function E_C to be minimized for the initial contour as presented as eq. (3.33):

$$E_C = E_{int} + E_{ext}. \quad (3.33)$$

Internal energy aims to restrain shape-based properties, such as topology, smoothness and curvature. The energy function associated to the internal energy presented by Kass et al. is defined as eq. (3.34) [64]:

$$E_{int} = \int_0^1 \alpha(\Omega) \left| \frac{\partial c}{\partial \Omega} \right|^2 + \beta(\Omega) \left| \frac{\partial^2 c}{\partial \Omega^2} \right|^2 \partial \Omega, \quad (3.34)$$

where the weighting parameter $\alpha(\Omega)$ is used to control the tension of the curve. The first order derivative defines the continuity of the curve, and allows for the curve to act like a membrane [71]. The other weighting parameter $\beta(\Omega)$ controls the rigidity of the curve, applied to the second order derivative, which defines the curvature of the curve. Controlling these constrains is considered a regularization of the curve, in the deformation applied in the evolving process applied by the external energy.

External energy is most commonly formed by a single source, namely local features derived from the image to be processed referred to as E_{img} . However, Kass et al. also presents the ability to include user defined constraints denoted as E_{con} . As this section is meant to describe the basic features of parametric active contours, E_{con} is disregarded in the energy model. External energy is comparable to kinetic energy, and differs from the internal energy, as it aims to deform the contour to minimize the distance to local image edges. Various means can be applied to attract the curve towards the desired object, whereas Kass et al. presents three energy functions, which when combined describes the total energy function for an image as eq. (3.35) [71]:

$$E_{ext} \approx E_{img} = \omega_{line} E_{line} + \omega_{edge} E_{edge} + \omega_{term} E_{term}, \quad (3.35)$$

where the weights ω can be adjusted to vary the behavior of the contour evolution.

Active Contours Without Edges (*Global CV*)

Active Contours Without Edges is a well known active contour method, developed by Tony F. Chan and Luminita A. Vese [69]. It is more commonly known as the Chan-Vese (CV) method and has since its origin been used as basis for multiple other methods.

Former methods depended on the image gradient $|\nabla \mathbf{I}|$ as curve evolution discontinuation criteria. However, for very noisy images or images containing low-contrast edges, this might result in curves to evolve undesired beyond object boundaries. Global CV is not depending on an image gradient as an evolution stopping criteria, instead it utilizes a stopping term defined by Mumford et al. [72]. Global CV is robust in regards to the positioning of the initialization curve \mathbf{C} [69].

The basic principles of Global CV is presented using a simplified fitting term, given as eq. (3.36) [69]:

$$F_1(\mathbf{C}) + F_2(\mathbf{C}) = \int_{inside(\mathbf{C})} |\mathbf{I}(i, j) - c_1|^2 \partial i \partial j + \int_{outside(\mathbf{C})} |\mathbf{I}(i, j) - c_2|^2 \partial i \partial j, \quad (3.36)$$

where \mathbf{C} denotes the initial evolving contour. In addition $I(i, j)$ is a given image, considered to consist of two regions, one being the object to be detected, and the other region being the background. Now, the boundary between these regions is defined as the contour \mathbf{C}_0 , so that the object region is placed inside \mathbf{C}_0 and the background is located outside of \mathbf{C}_0 . The constant c_1 defines the average intensity values of image \mathbf{I} inside the contour \mathbf{C} , and c_2 defines the average intensity values outside \mathbf{C} .

Next, four different scenarios of positioning of \mathbf{C} relative to \mathbf{C}_0 is considered as presented on fig. 3.15, to determine the minimizer of the fitting term eq. (3.36). Of the four scenarios, it is illustrated

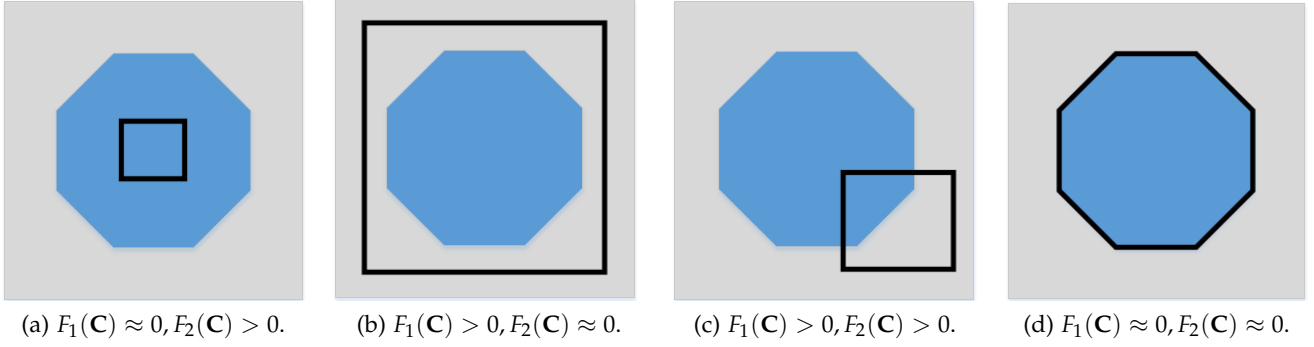


Figure 3.15: The four possible initializations and placements of \mathbf{C} . Gray illustrates the background region, blue defines the object with the boundary \mathbf{C}_0 and the black squares represent the curve \mathbf{C} . The scenario in fig. 3.15d indicates the minimization of fitting term eq. (3.36). Inspired by [69]

that the minimization of the fitting term eq. (3.36) is given in the case where the curve \mathbf{C} is placed directly on \mathbf{C}_0 eq. (3.37) [69]:

$$\inf_{\mathbf{C}} \{F_1(\mathbf{C}) + F_2(\mathbf{C})\} \approx 0 \approx F_1(\mathbf{C}_0) + F_2(\mathbf{C}_0). \quad (3.37)$$

This minimization problem defines the basic principle of the Global CV method.

However, to make the Global CV model more adaptive, in regards to the dimensions of the objects desired to be detected, some regularization terms are added. These are introduced through the energy function $F(\mathbf{C})$ presented on eq. (3.36) [69]:

$$\begin{aligned} F(\mathbf{C}) = & \mu \cdot \text{Length}(\mathbf{C}) + v \cdot \text{Area}(\text{inside}(\mathbf{C})) \\ & + \lambda_1 \int_{\text{inside}(\mathbf{C})} |\mathbf{I}(i, j) - c_1|^2 \partial i \partial j \\ & + \lambda_2 \int_{\text{outside}(\mathbf{C})} |(\mathbf{I}(i, j) - c_2|^2 \partial i \partial j \end{aligned} \quad (3.38)$$

where $\mu \geq 0$, $v \geq 0$ and $\lambda_1, \lambda_2 > 0$ are fixed parameters. μ is seen as a length parameter, and v as an area parameter, both used to scale the relative importance of the contour \mathbf{C} dimensions. In accordance to [69], the three parameters value $v = 0$ and $\lambda_1 = \lambda_2 = 1$ are chosen, and μ varied to enable the possibility to detect smaller objects.

The CV method is further described through a level set method, where the contour \mathbf{C} is replaced with ϕ and the following assumptions eq. (3.39) [69]:

$$\begin{cases} \mathbf{C} = \{(i, j) \in \Omega : \phi(i, j) = 0\}, \\ \text{inside}(\mathbf{C}) = \{(i, j) \in \Omega : \phi(i, j) > 0\}, \\ \text{outside}(\mathbf{C}) = \{(i, j) \in \Omega : \phi(i, j) < 0\} \end{cases} \quad (3.39)$$

where Ω is the domain of image \mathbf{I} so that $\mathbf{C} \subset \Omega$ and $\phi : \Omega \rightarrow \mathbb{R}$ [69]. Thereby, the object boundary is given by the zero-level curve of the level set function ϕ , as presented on fig. 3.16. Next, assuming the

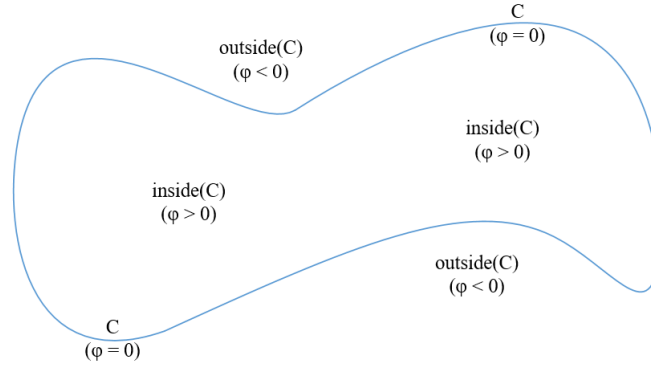


Figure 3.16: The curve \mathbf{C} represented as the zero-level line of a level set function. Inspired by [69]

inside of the contour \mathbf{C} as the regularized Heaviside function H_ϵ eq. (3.40) [69]:

$$H_\epsilon(\phi(i, j)) = \frac{1}{2} \left(1 + \frac{2}{\pi} \arctan \left(\frac{\phi(i, j)}{\epsilon} \right) \right), \quad (3.40)$$

and the associated Dirac delta measure, being the derivative of H_ϵ to describe the surface of the contour \mathbf{C} as eq. (3.41) [69]:

$$\delta_\epsilon(\phi(i, j)) = \frac{\partial H_\epsilon(\phi(i, j))}{\partial \phi(i, j)} = \frac{1}{\pi} \frac{\epsilon}{\epsilon^2 + \phi(i, j)^2}, \quad (3.41)$$

where the parameter ϵ is kept constant at $\epsilon = 1$ in accordance with [69]. The energy function of CV can now be written as eq. (3.42) [69]:

$$\begin{aligned} F_\epsilon(\phi) = & \mu \int_{\Omega} \delta_\epsilon(\phi(i, j)) |\nabla \phi(i, j)| \partial i \partial j \\ & + \int_{\Omega} |\mathbf{I}(i, j) - c_1|^2 H_\epsilon(\phi(i, j)) \partial i \partial j \\ & + \int_{\Omega} |\mathbf{I}(i, j) - c_2|^2 (1 - H_\epsilon(\phi(i, j))) \partial i \partial j \end{aligned} \quad (3.42)$$

Now, to segment a given image \mathbf{I} , the energy function eq. (3.42) is minimized with respect to the average intensity constants c_1 and c_2 which are expressed as functions of ϕ . By keeping ϕ fixed, the constants are defined as eqs. (3.43) and (3.44) [69]:

$$c_1(\phi) = \frac{\int_{\Omega} \mathbf{I}(i, j) H_\epsilon(\phi(i, j)) \partial i \partial j}{\int_{\Omega} H_\epsilon(\phi(i, j)) \partial i \partial j}, \quad (3.43)$$

$$c_2(\phi) = \frac{\int_{\Omega} \mathbf{I}(i, j) (1 - H_\epsilon(\phi(i, j))) \partial i \partial j}{\int_{\Omega} (1 - H_\epsilon(\phi(i, j))) \partial i \partial j}, \quad (3.44)$$

which in a more simplified version can be explained as eq. (3.45) [69]:

$$\begin{cases} c_1(\phi) = \text{average}(\mathbf{I}) & \text{in } \{\phi \geq 0\} \\ c_2(\phi) = \text{average}(\mathbf{I}) & \text{in } \{\phi < 0\} \end{cases} \quad (3.45)$$

Next, by keeping c_1 and c_2 fixed, the gradient descent equation for the evolution of the level set function ϕ is derived from eq. (3.42) as eq. (3.46) [69]:

$$\frac{\partial \phi}{\partial t} = \delta(\phi) \left[\mu \nabla \cdot \left(\frac{\nabla \phi}{|\nabla \phi|} \right) - \left(\mathbf{I}(i, j) - c_1 \right)^2 + \left(\mathbf{I}(i, j) - c_2 \right)^2 \right], \quad (3.46)$$

which is discretized using standard finite differences as eq. (3.47) [69]:

$$\begin{aligned} \frac{\phi(i, j)^{k+1} - \phi(i, j)^k}{\Delta t} = & \delta(\phi(i, j)^k) \left[\mu \Delta_-^x \cdot \left(\frac{\Delta_+^x \phi(i, j)^{k+1}}{\sqrt{(\Delta_+^x \phi(i, j)^k)^2 + \frac{1}{4}(\phi(i, j+1)^k - \phi(i, j-1)^k)^2}} \right) \right. \\ & + \mu \Delta_-^y \cdot \left(\frac{\Delta_+^y \phi(i, j)^{k+1}}{\sqrt{(\Delta_+^y \phi(i, j)^k)^2 + \frac{1}{4}(\phi(i+1, j)^k - \phi(i-1, j)^k)^2}} \right) \\ & \left. - \left(\mathbf{I}(i, j) - c_1(\phi(i, j)^k) \right)^2 + \left(\mathbf{I}(i, j) - c_2(\phi(i, j)^k) \right)^2 \right] \end{aligned} \quad (3.47)$$

where the forward and backward standard differences are defined as:

$$\begin{aligned} \Delta_-^x \phi(i, j) &= \phi(i, j) - \phi(i-1, j), & \Delta_+^x \phi(i, j) &= \phi(i+1, j) - \phi(i, j), \\ \Delta_-^y \phi(i, j) &= \phi(i, j) - \phi(i, j-1), & \Delta_+^y \phi(i, j) &= \phi(i, j+1) - \phi(i, j). \end{aligned} \quad (3.48)$$

Lastly, the approach of the Global CV method is summed up and presented in alg. 6:

Algorithm 6: Chan-Vese algorithm

```

for  $i = 1$  to  $M$  do
  for  $j = 1$  to  $N$  do
    Initialization of level set function  $\phi(i, j)^0 = \phi(i, j)_0$ ;
    for  $k = 0$  to  $k_{max}$  do
      Calculate  $H(\phi(i, j)^k)$  using eq. (3.40);
      Calculate  $\delta_\epsilon(\phi(i, j)^k)$  using eq. (3.41);
      Compute  $c_1(\phi(i, j)^k)$  and  $c_2(\phi(i, j)^k)$  using eqs. (3.43) and (3.44);
      Solve eq. (3.47), to determine  $\phi(i, j)^{k+1}$ ;
    end
  end
end

```

First the initialization of the model is executed by the placement of the initial contour, defining the zero-level set. The Heaviside and Dirac are hereafter calculated. The average intensity values c_1 and c_2 are calculated based on the location of the level set function $\phi(i, j)$. Using the two constants, $\phi(i, j)$ is evolved according to eq. (3.47), resulting in $\phi(i, j)^{k+1}$. This procedure is handed out for the given k_{max} amount of iterations, yielding the finalized contour $\phi(i, j)^{k_{max}}$.

Localizing Region-Based Active Contours (*Local CV & Local MS*)

The second method analyzed, is based on the local region-based active contour framework presented by Lankton et al. [70]. Their work was focused on creating a framework for region-based segmentation utilizing localized versions of already existing region-based energies, such as [69, 73]. Basing the active contour on local properties instead of global, is favorable for images where the ROI and background shares same statistical model, and thereby considered as heterogeneous.

Like the method Global CV, the localized framework considers a given image \mathbf{I} , as the initial image to be processed, defined in the domain Ω . A closed contour is denoted \mathbf{C} , which determines the binary initialization of the active contour. The contour \mathbf{C} is described through the level set function ϕ in accordance to eq. (3.39). The implementation of the localized region-based model analyzed in this study, utilizes the same Heaviside function $H_\epsilon(\phi(i, j))$ eq. (3.40), originally presented in Global CV, in describing the inside region of the contour ϕ . Again, where the condition parameter ϵ is kept constant at $\epsilon = 1$ in accordance to [69]. The exterior of ϕ , being the region outside of the contour, is defined as $(1 - H_\epsilon(\phi(i, j)))$, and the area around the contour is specified using the same Dirac delta function eq. (3.41).

To only consider the local regions of the contour ϕ , Lankton et al. introduced the idea of adding an object, such as a disk or square in the peripheral of ϕ . Where after the evolution of the contour is based on the local properties within this object, instead of the global properties for the entire image \mathbf{I} . Such an object can be described as a disk through the characteristic function eq. (3.49) [70]:

$$\mathbf{D}(x, y) = \begin{cases} 1, & \|x - y\| < r \\ 0, & \text{otherwise.} \end{cases}, \quad (3.49)$$

where the points $y(i, j)$ within the area defined by a radius r from the center point $x(i, j)$ is 1 and 0 otherwise.

Next, to determine the local growth or retreat of the active contour, an energy function E is defined as eq. (3.50) [70]:

$$E(\phi) = \int_{\Omega_x} \delta\phi(x) \int_{\Omega_y} \mathbf{D}(x, y) \cdot F(\mathbf{I}(y), \phi(y)) \partial y \partial x. \quad (3.50)$$

The energy function has an internal energy function denoted F , which is considered a generic function, as it is replaceable by various local region-based energy measures, such as localized versions of [69, 73].

The internal energy function F is multiplied with $\delta\phi(x)$ in the integral over x , hence the integral of the circumference of the curve. This ensures that the growth of the contour will not result in new contours, but still allows for splitting and merging of the contour, as it adheres to the circumference.

Next, by applying each x in $\delta\phi(x)$ with the object mask $\mathbf{D}(x, y)$, it is ensured that the energy function F only considers local information in the neighborhood of x .

Lastly, curve smoothing of the final contour is ensured by applying a regularization term to the energy function E , resulting in E_{reg} as eq. (3.51) [70]:

$$E_{reg}(\phi) = E(\phi) + \alpha \int_{\Omega_x} \delta\phi(x) \|\nabla\phi(x)\| \partial x, \quad (3.51)$$

where the parameter α is used to weight the smoothing factor. Next, the evolution equation for this energy equation can be found by taking the first variation of $E_{reg}(\phi)$ with respect to ϕ , resulting in eq. (3.52) [70]:

$$\begin{aligned} \frac{\partial\phi}{\partial t}(x) = & \delta\phi(x) \int_{\Omega_y} \mathbf{D}(x, y) \cdot \nabla_{\phi(y)} F(\mathbf{I}(y), \phi(y)) \partial y \\ & + \alpha \cdot \frac{\delta\phi(x)}{\left(\frac{\nabla\phi(x)}{|\nabla\phi(x)|} \right)}. \end{aligned} \quad (3.52)$$

By utilizing the object structure $\mathbf{D}(x, y)$, the global constants earlier presented as eqs. (3.43) and (3.44)

are transformed to localized versions u_x and v_x eqs. (3.53) and (3.54) [70]:

$$u_x = \frac{\int_{\Omega_y} \mathbf{D}(x, y) \cdot H(\phi(y)) \cdot \mathbf{I}(y) \partial y}{\int_{\Omega_y} \mathbf{D}(x, y) \cdot H(\phi(y)) \partial y}, \quad (3.53)$$

$$v_x = \frac{\int_{\Omega_y} \mathbf{D}(x, y) \cdot (1 - H(\phi(y))) \cdot \mathbf{I}(y) \partial y}{\int_{\Omega_y} \mathbf{D}(x, y) \cdot (1 - H(\phi(y))) \partial y}. \quad (3.54)$$

Next, by inserting these local intensity means in internal energy functions, such as the one used in Global CV, the Local CV is given as eq. (3.55) [70]:

$$F_{CV} = H(\phi(y))(\mathbf{I}(y) - u_x)^2 + (1 - H(\phi(y))) (\mathbf{I}(y) - v_x)^2, \quad (3.55)$$

which can be used directly as an energy measure for eq. (3.51). To derive the evolution equation for the curve ϕ , the derivative of F_{CV} is taken with respect to $\phi(y)$, which yields eq. (3.56) [70]:

$$\nabla_{\phi(y)} F_{CV} = \delta\phi(y) ((\mathbf{I}(y) - u_x)^2 - (\mathbf{I}(y) - v_x)^2). \quad (3.56)$$

When inserted into eq. (3.52), the definition of the curve evolution ϕ for the Local CV energy as: eq. (3.57) [70]:

$$\frac{\partial\phi}{\partial t}(x) = \delta\phi(x) \int_{\Omega_y} \mathbf{D}(x, y) \cdot \delta\phi(y) ((\mathbf{I}(y) - u_x)^2 - (\mathbf{I}(y) - v_x)^2) \partial y + \alpha \cdot \frac{\delta\phi(x)}{\left(\frac{|\nabla\phi(x)|}{|\nabla\phi(x)|}\right)}, \quad (3.57)$$

where the minimum energy, is obtained, when each point around the curve has evolved, such that the local interior and exterior for every point is best approximated by the two local means u_x and v_x [70].

Another example of an region-based energy, denoted Local MS, which has been analyzed and tested is, the one presented by Yezzi et al. [73]. This energy function, which is defined as mean separation energy is given on its global form as E_{MS} eq. (3.58) [70]:

$$E_{MS} = \int_{\Omega_y} (c_1 - c_2)^2, \quad (3.58)$$

where c_1 and c_2 are the global intensity means presented in eqs. (3.43) and (3.44). The energy model proposes that the mean intensities for the interior and exterior regions should be maximally separated, thereby creating the largest contrast.

By inserting the local intensity means as defined by eqs. (3.53) and (3.54), the local internal energy function F_{MS} is given as eq. (3.59) [70]:

$$F_{MS} = \int_{\Omega_y} (u_x - v_x)^2, \quad (3.59)$$

which is a valid energy measure for $E_{reg}(\phi)$ eq. (3.51). Again, as for the Local CV F_{CV} , the local curve ϕ evolution is found by inserting the derivative of F_{MS} into eq. (3.52), leading to eq. (3.60) [70]:

$$\frac{\partial\phi}{\partial t}(x) = \delta\phi(x) \int_{\Omega_y} \mathbf{D}(x, y) \cdot \delta\phi(y) \left(\frac{(\mathbf{I}(y) - u_x)^2}{A_u} - \frac{(\mathbf{I}(y) - v_x)^2}{A_v} \right) \partial y + \alpha \cdot \frac{\delta\phi(x)}{\left(\frac{|\nabla\phi(x)|}{|\nabla\phi(x)|}\right)}, \quad (3.60)$$

for which A_u is the area of the local interior region, and A_v the area of the local exterior region:

$$A_u = \int_{\Omega_y} \mathbf{D}(x, y) \cdot H(\boldsymbol{\phi}(y)) \partial y, \quad (3.61)$$

$$A_v = \int_{\Omega_y} \mathbf{D}(x, y) \cdot (1 - H(\boldsymbol{\phi}(y))) \partial y, \quad (3.62)$$

where the minimum energy is obtained when the largest difference between the two local means u_x and v_x for every point x on the contour $\boldsymbol{\phi}$.

The localized region-based active contour framework, using both Local CV and Local MS energy models, are summarized through alg. 7.

Algorithm 7: Localizing Active Contour

```

for  $i = 1$  to  $M$  do
  for  $j = 1$  to  $N$  do
    Initialization of level set function  $\boldsymbol{\phi}(i, j)^0 = \boldsymbol{\phi}(i, j)_0$ ;
    Initialization of object size  $\mathbf{D}(x, y)$ ;
    for  $k = 0$  to  $k_{max}$  do
      Calculate  $H(\boldsymbol{\phi}^k(y))$  using eq. (3.40);
      Convolve  $\mathbf{D}(x, y)$  with  $H(\boldsymbol{\phi}^k(y))$ ;
      Convolve  $\mathbf{D}(x, y)$  with  $H(\boldsymbol{\phi}^k(y)) \cdot \mathbf{I}(y)$ ;
      Compute  $u_x$  and  $v_x$  using the two above convolutions in eqs. (3.53) and (3.54);
      Compute either alg. 8 or alg. 9, depending on the desired energy model;
    end
  end
end

```

Algorithm 8: Local CV energy model

```

Compute  $\nabla_{\boldsymbol{\phi}(y)} F_{CV}$  using eq. (3.56);
Use  $\nabla_{\boldsymbol{\phi}(y)} F_{CV}$  to solve eq. (3.57), and thereby determine  $\boldsymbol{\phi}^{k+1}$ ;

```

Algorithm 9: Local MS energy model

```

Compute  $A_u$  and  $A_v$  using eqs. (3.61) and (3.62);
Use  $A_u$  and  $A_v$  to solve eq. (3.60), and thereby determine  $\boldsymbol{\phi}^{k+1}$ ;

```

First the algorithm is initialized by the placement of the initial contour $\boldsymbol{\phi}_0$, defining the zero-level set for the given image. In addition the size of the object $\mathbf{D}(x, y)$ is calculated. The inside of the contour for the given iteration is calculated. To ensure that only local properties are used in the evolution computation, the object $\mathbf{D}(x, y)$ is convolved with $H(\boldsymbol{\phi}^k(y))$ and $H(\boldsymbol{\phi}^k(y)) \cdot \mathbf{I}(y)$. Hereafter, the local average intensity values u_x and v_x are calculated for the given placement of $\boldsymbol{\phi}^k$. For both cases of energy models, the two local constants are used to estimate the evolution of $\boldsymbol{\phi}$, using eq. (3.57) for Local CV and eq. (3.60) for Local MS. This procedure is conducted for the given k_{max} amount of iterations, yielding the finalized contour $\boldsymbol{\phi}^{k_{max}}$.

3.4.6 Segmentation Validation

Segmentation evaluation is an important step in order to verify and compare segmentation methods. The subject of segmentation evaluation is much discussed as it is considered a difficult task. Image segmentation is strongly depended on the HVS, and is highly subjective, and thus it is difficult to create a valid evaluator.

Overall, segmentation evaluation can be divided into two categories, objective and subjective [74]. Subjective methods are based on a fully human evaluation. However, this is a disadvantageous approach as the same segmentation might be scored differently by different evaluators, because of the human interpretation [74]. In order to have a non biased subjective evaluation, a large evaluator group as well as a high number of images for evaluation should be available. This makes subjective evaluation highly time consuming and tedious [74].

The counter part, namely objective evaluation, does not use human evaluation but rather methods creating consistent unbiased results. Objective methods is therefore, when compared with the subjective methods, faster and simpler to use. However, defining an objective method capable of correct evaluating might be more challenging, as segmentation is a subjective matter in general.

Objective evaluation can be further divided into supervised and unsupervised methods. Supervised methods utilizes a ground truth or a golden standard as comparison for the segmentation evaluation, whereas unsupervised evaluators use no reference. A lot of different unsupervised evaluation methods exists [74]. These can be highly effective in a scenario where different segmentation methods are to be compared, or a single segmentation method is tested with different parameters. However, none of the existing methods shows exceptional performance and is neither consistent nor robust [74].

Objective supervised evaluation is used in this study, mainly because the subjective evaluation is highly time consuming and tedious. Secondly, because non of the unsupervised methods shows promising results.

Segmentation must be evaluated on three different parameters, namely; accuracy, precision and efficiency [75]. The accuracy covers how far the results are from the ground truth. The precision of a segmentation concerns how consistent it is when repeated and using different inputs. And finally, the efficiency refers to the practical use of the method [75]. Two common types of metrics are used in this study to evaluate the segmentation, namely distance-based metrics and volume-based metrics.

Distance-based metric

Distance-based metrics are used to measure the delinearity in the boundary of a segmentation, thus the distance between the ground truth boundary and the segmented result [75]. One such distance-based metric is the Hausdorff distance [76]. The Hausdorff distance measures the maximum difference error in a segmentation. All minimum distances, the infimum $\{d(i, j)\}_{\mathbf{B}_{seg} \rightarrow \mathbf{B}_{GT}}$, for each point $\mathbf{B}_{seg}(i, j)$ in the segmentation result contour \mathbf{B}_{seg} of size $M \times N$, to the nearest point $\mathbf{B}_{GT}(i, j)$ in the ground truth contour \mathbf{B}_{GT} of size $M \times N$ is calculated. Likewise the infimum $\{d(i, j)\}_{\mathbf{B}_{GT} \rightarrow \mathbf{B}_{seg}}$ is calculated as these might be different. The Hausdorff distance $d_H(\mathbf{B}_{seg}, \mathbf{B}_{GT})$ is then given by the maximum, the supremum, of the two infimums $\{d(i, j)\}_{\mathbf{B}_{seg} \rightarrow \mathbf{B}_{GT}}$ and $\{d(i, j)\}_{\mathbf{B}_{GT} \rightarrow \mathbf{B}_{seg}}$ [57]. The final formula for the Hausdorff distance is given by eq. (3.63) [57]:

$$d_H(\mathbf{B}_{seg}, \mathbf{B}_{GT}) = \max \left\{ \sup_{\mathbf{B}_{seg}(i,j) \in \mathbf{B}_{seg}} \inf_{\mathbf{B}_{GT}(i,j) \in \mathbf{B}_{GT}} d(\mathbf{B}_{seg}(i, j), \mathbf{B}_{GT}(i, j)), \right. \\ \left. \sup_{\mathbf{B}_{GT}(i,j) \in \mathbf{B}_{GT}} \inf_{\mathbf{B}_{seg}(i,j) \in \mathbf{B}_{seg}} d(\mathbf{B}_{seg}(i, j), \mathbf{B}_{GT}(i, j)) \right\}, \quad (3.63)$$

where, $i \in 1, 2, \dots, M$ and $j \in 1, 2, \dots, N$ are indices in the $M \times N$ contours \mathbf{B}_{seg} and \mathbf{B}_{GT} . A visual representation of the Hausdorff distance and its asymmetry is seen in fig. 3.17. The Hausdorff distance is useful for assessing the border differences between two contours, which is especially important in this study, as the border of the segmentation is considered the most crucial part.

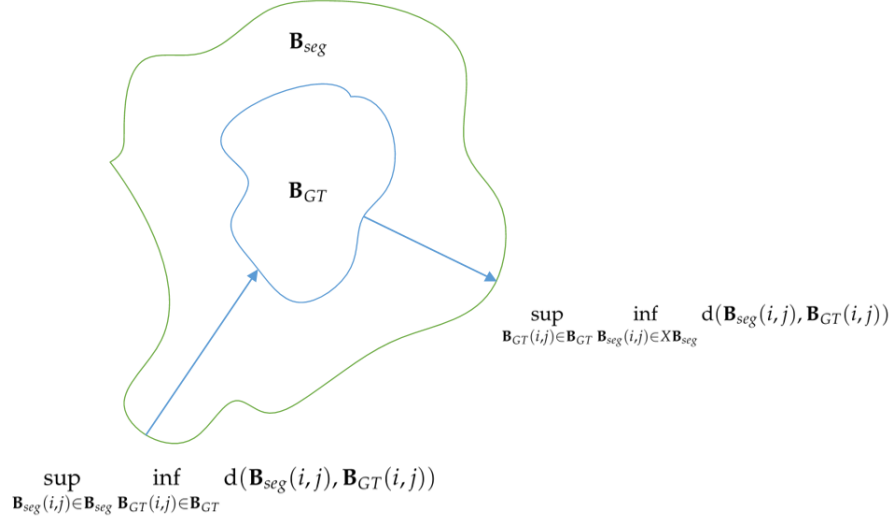


Figure 3.17: Visual representation of the Hausdorff distance for a segmentation result contour \mathbf{B}_{seg} and a ground truth contour \mathbf{B}_{GT} .

Volume-based metric

Volume-based metrics measures the area or volume difference between two contours. Area evaluation results can statistically be divided into four cardinalities; true positive (TP), true negative (TN), false positive (FP) and false negative (FN). These four categories are given by eqs. (3.64) to (3.67):

$$\mathbf{A}_{TP} = \mathbf{A}_{seg} \cap \mathbf{A}_{GT}, \quad (3.64)$$

$$\mathbf{A}_{TN} = \mathbf{A}_{Scene} - \mathbf{A}_{seg} - \mathbf{A}_{GT}, \quad (3.65)$$

$$\mathbf{A}_{FP} = \mathbf{A}_{seg} - \mathbf{A}_{GT}, \quad (3.66)$$

$$\mathbf{A}_{FN} = \mathbf{A}_{GT} - \mathbf{A}_{seg}. \quad (3.67)$$

For a segmented result area \mathbf{A}_{seg} and a ground truth area \mathbf{A}_{GT} , the \mathbf{A}_{TP} area is the intersection of the two, and defines the correctly segmented area. The \mathbf{A}_{TN} is the correctly rejected segmented area, and is the two areas subtracted the \mathbf{A}_{Scene} which is the rest of the image. The \mathbf{A}_{FP} defines over segmentation meaning the area of \mathbf{A}_{seg} not part of \mathbf{A}_{GT} . Lastly \mathbf{A}_{FN} is the under segmentation meaning the area of \mathbf{A}_{GT} not part of \mathbf{A}_{seg} . \mathbf{A}_{FP} and \mathbf{A}_{FN} can provide an adequate estimation of the tendencies of a segmentation algorithm, and can efficiently be used to adjust different parameters. A representation of the four types of areas is given in fig. 3.18.

These four cardinalities can further be used to specify the ratios of accuracy for the segmentation, defined as eqs. (3.68) to (3.71):

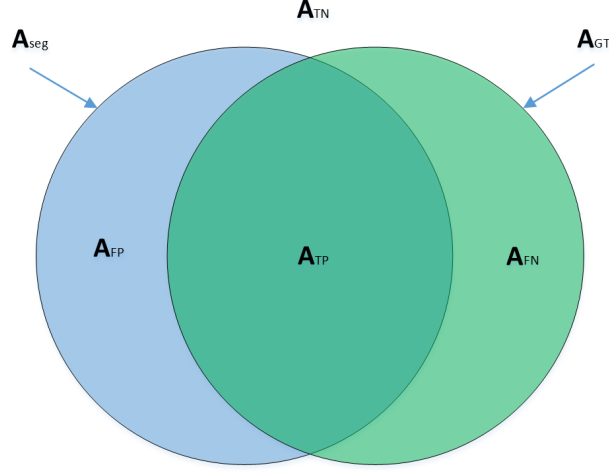


Figure 3.18: Visual representation of the TN, TP, FP and FN for a segmentation result contour \mathbf{B}_{seg} and a ground truth contour \mathbf{B}_{GT}

$$TPR = Sensitivity = \frac{\mathbf{A}_{TP}}{\mathbf{A}_{TP} + \mathbf{A}_{FN}}, \quad (3.68)$$

$$TNR = Specificity = \frac{\mathbf{A}_{TN}}{\mathbf{A}_{TN} + \mathbf{A}_{FP}}, \quad (3.69)$$

$$FPR = Fallout = \frac{\mathbf{A}_{FP}}{\mathbf{A}_{FP} + \mathbf{A}_{TN}} = 1 - TNR, \quad (3.70)$$

$$FNR = \frac{\mathbf{A}_{FN}}{\mathbf{A}_{FN} + \mathbf{A}_{TP}} = 1 - TPR. \quad (3.71)$$

These ratios give a better representation of the individual cardinalities, in relation to the segmented image. One of the most common and used volume-based metrics, used for medical image segmentation evaluation [77], is the Dice coefficient [78] which is defined as eq. (3.72) [77]:

$$D = \frac{2 \cdot |\mathbf{A}_{seg} \cap \mathbf{A}_{GT}|}{|\mathbf{A}_{seg}| + |\mathbf{A}_{GT}|} = \frac{2 \cdot \mathbf{A}_{TP}}{2 \cdot \mathbf{A}_{TP} + \mathbf{A}_{FP} + \mathbf{A}_{FN}} \quad (3.72)$$

The Dice coefficient provides a value between 0 and 1, where 0 represents no overlap and 1 total overlap. The volume-based metrics can give a good general indication of the differences in two segmentations.

3.5 Registration

Registration within medical images is the process concerning the alignment of two or more images. The alignment means that features, present in two or more images, are aligned so their coordinates become equal. In image registration there is distinguished between the fixed image, which stays stationary through the alignment process, and the moving image applied with the alignment transformation.

The process of image registration is often important and needed in medical image processing. Registration has a large application range, from aligning images with different modalities to the alignment of two 3D structures. The importance of image registration in this study, is due to the HR-pQCT image dataset acquisition. The image datasets are acquired in 3 sets of 110 images, which each takes around 3 min to compute. Because of this relatively long acquisition time, it is practically impossible for the patient undergoing the scan, to remain completely still in the scanned area. This results in movement a rotation in the bone placement between the 110 image acquisitions, as seen in fig. 3.19. The alignment of the bone structures in the image is important for further analysis, both in subjective and objective erosion detection.

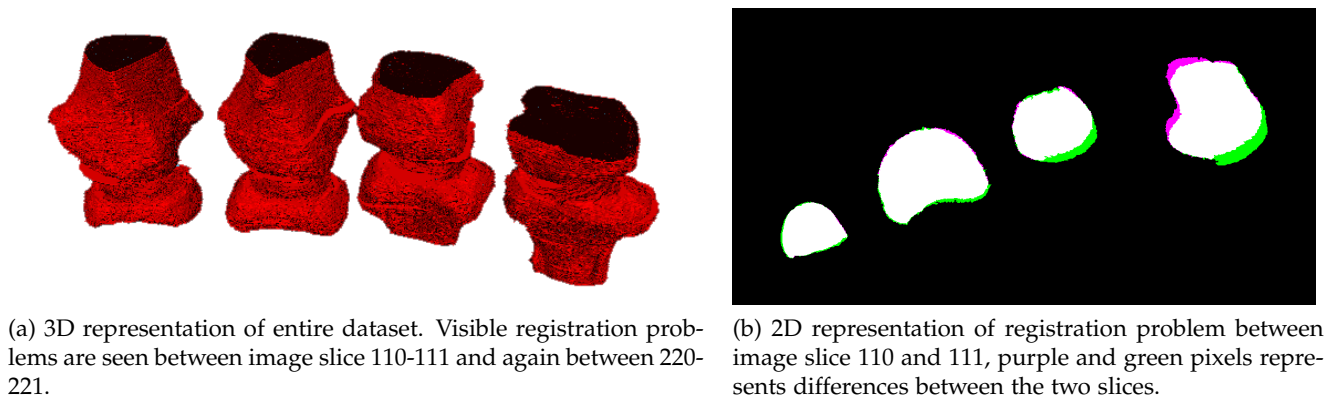


Figure 3.19: 3D and 2D representations of the registration problems.

As explained, image registration is a broad image processing subject, both in techniques and applications. Because of this, a classification was performed in [79], and further classified with subcategories by [80], and explained by [81, 82, 83]. The registration categorization is a high level division containing nine overall categories, each with their own subcategories. The categories are seen in list 3.2.

The dimensionality of a registration is the number of dimensions in the images to be aligned e.g. 2D-2D, 2D-3D or 3D-3D. Higher dimensions are intuitively more complex. Time can also be a factor in the dimensionality of a registration, also adding to the complexity. The nature of registration basis can be either extrinsic or intrinsic. Extrinsic means images are aligned according to foreign objects in the image e.g. screws, fixtures or frames. Intrinsic methods only use patient information in the images to determine the transformation, and can be subdivided into landmark, segmentation, voxel property and classification based methods.

Landmark based methods use a limited set of points, corresponding to equal positions in the moving and fixed image. The points can either be anatomical, typically selected subjective, or geometric, typically selected automatic. Segmentation based methods utilize similar segmented areas in the moving and fixed image, and use these areas as basis for the transformation. Voxel intensity based methods use the information from all the voxel or pixels in the moving and fixed image. Voxel intensity based methods typically consist of an image metric, describing the correlation between the moving and fixed image, and an optimization process finding the best image metric. Lastly, is the clas-

List 3.2: Registration categorization

- | | |
|-------------------------------------|-------------------------|
| 1. Dimensionality | 6. Optimization |
| (a) Spatial | (a) Computed |
| (b) Time | (b) Searched |
| 2. Nature of the registration basis | 7. Modalities involved |
| (a) Extrinsic | (a) Monomodal |
| (b) Intrinsic | (b) Multimodal |
| 3. Nature of the transformation | 8. Subject |
| (a) Rigid | (a) Intrasubject |
| (b) Affine | (b) Intersubject |
| (c) Projective | (c) Atlas |
| (d) Curved | |
| 4. Domain of the transformation | 9. Object |
| (a) Global | (a) Head |
| (b) Local | (b) Thorax |
| 5. Interaction | (c) Abdomen |
| (a) Interactive | (d) Pelvis and perineum |
| (b) Semi-automatic | (e) Orthopedic |
| (c) Automatic | (f) Spine and vertebrae |

sification based methods, which extract a finite number of features from both the fixed and moving images. These features are then compared, to find similar features, thereby resulting in the optimum transformation.

The nature of transformation describes the transformation applied to the moving image. This can be either rigid, affine, projective or curved. The effect of each type of transformation is seen in fig. 3.20. The domain of the transformation can either be global or local, which is also illustrated in fig. 3.20:

The interaction of the registration, is the amount of user interaction involved in the process. This can be interactive, semi-automatic or automatic. The amount of user interaction is also a complexity reference, as the more automatic the registration is the more complex. The optimization of a registration is different based on the nature of the registration. For landmark based methods, the transformation can typically be computed, whereas for segmentation, voxel intensity and classification based methods, the transformation is searched for through optimization algorithms. The modality of a registration concerns the modalities of the images used in the registration. If the images are of the same modalities, they are referred to as monomodal, whereas multiple modalities are referred to as multimodal. If the registration is either monomodal or multimodal, different types of both nature of transformation, optimization and transformation are used. Multimodal images tend to be more complex, as simple reference points or voxel intensities are not similar. The subject of a registration refers to the person involved in the registration. It can either be intrasubject if the images origin from the same person, intersubject if the images are from different persons, or atlas if a persons images are

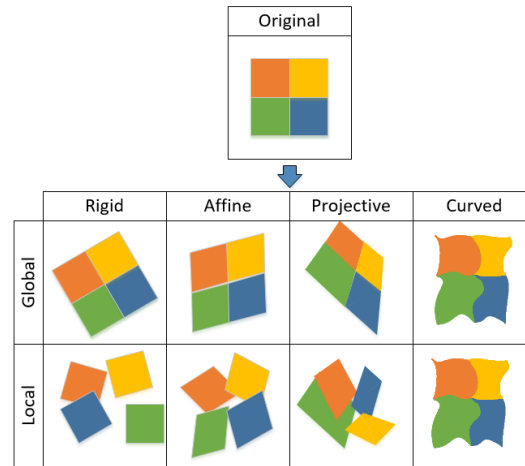


Figure 3.20: Points mapped from one image to another, using the rigid transformation have the same distance between them. In an affine transformation, parallel lines from one image is mapped to parallel lines in another image. Projective transformation maps lines in one image to lines in another image. Finally, curved transformation maps lines in one image to curves in another image. These transformations can either be performed globally on the entire image or locally applied to sections of the image.

registered to a constructed model. Lastly, the object of a registration is the anatomically object e.g. head, thorax, pelvis or abdomen [83].

Based on the categories presented and a preliminary research and development study [84], a classification of the registration problem for this study is conducted, and seen in table 3.1:

Table 3.1: Registration categorization for HR-pQCT image dataset

Dimensionality	Spatial 2D-2D
Registration basis	Intrinsic voxel intensity based
Transformation	Rigid
Domain	Global and local
Interaction	Automatic
Optimization	Searched
Modality	Mono-modal HR-pQCT
Subject	Intrasubject
Object	Orthopedic Hand

The dimensionality is 2D-2D, as the only registrations needed are between slice 110 and 111 and between 220 and 221. The nature of transformation is defined as voxel intensity based, as it is commonly used and shows reliable results, both in accuracy, precision and computationally complexity [84]. The domain of the transformation is limited to rigid transformation, as other transformation types may disrupt the integrity of the information in the images, which will decrease the prognosis reliability. The domain of the transformation is both local and global, as both types will be tested. Tests concerning global transformation of the whole image, will be compared to local transformations of the individual joints. The reason for the local transformation is that the patient movement may not produce the same transformation in the individual joints. The interaction of the algorithm shall be automatic. Because of the choice of voxel intensity based methods, the optimization process is searched. As the images are all HR-pQCT images, the modality is monomodal. The individual datasets origins from the same patient, meaning the subject is intersubject. Lastly, the object is the hand.

3.5.1 Proposed Registration Method

Based on the classification of the registration needed, as presented in section 3.5, a registration method is proposed. As the patient motion resulting in the registration problem may produce different transformations for each joint, local registration for each joint may be desired. In order to create a local registration for each joint, a clear segmentation and separation of each joint is needed. This means that the registration should be carried out after the segmentation. For the proposed registration method the binary images, results from the segmentation method. This is done, as their borders are the periosteal border, which is the border desired to be aligned. Therefore, the assumption is that the segmentation provides a clear segmentation of the periosteal bone, as the registration otherwise will produce false alignment. The binary image is selected, as a clear monomodal separation is then obtained, thereby eliminating registration errors produced by image noise and artifacts. Simple registration techniques can also be used, as the image will have a clear optimization minimum, which also implies faster execution time. The final proposed method, either global or local, are to be selected through experiments, testing both methods performances. A simple run-through of the global registration process in algorithmic form is seen in alg. 10.

Algorithm 10: Global registration process algorithm

```

transformation = registration(dataset(110),dataset(111));
for i = 111 to 220 do
  | dataset(i) = interpolate(dataset(i),transformation)
end
transformation = registration(dataset(220),dataset(221));
for i = 221 to 330 do
  | dataset(i) = interpolate(dataset(i),transformation)
end

```

The global registration initiates with the registration of image slice 110 as the fixed image and the image slice 111 as the moving image. The registration returns a transformation aligning the moving and fixed image. Each image in the segmented binary dataset between image slice 111 and 220 are then interpolated using the transformation. Following is a new registration of dataset image slice 220 as the fixed image and the dataset image slice 221 as the moving image. The segmented binary dataset images between 221 and 330 are then interpolated with the returned transformation. A simple run-through of the local registration process is also presented in algorithmic form in alg. 11.

The local registration starts with the separation of each joint in the binary segmented dataset, using the function *cropJoints*. This function returns four binary segmented datasets of same size as of the original dataset, each containing one of the four joint contours. A registration process with image slice 110 as the fixed image, and image slice 111 as the moving image, is applied for each joint dataset, thereby providing four different transformations. Each joint dataset image slices between image slice 111 and 220, are then interpolated using their corresponding transformation. Following a registration process, with joint dataset image slice 220 as the fixed image and joint dataset image slice 221 as the moving image, are carried out for each joint dataset, resulting in four new different transformations. The joint dataset image slices between 221 and 330 are then interpolated with their corresponding transformation.

Algorithm 11: Local registration process algorithm

```

[joint1, joint2, joint3, joint4] = cropJoints(dataset);
transformation1 = registration(joint1(110), joint1(111));
transformation2 = registration(joint2(110), joint2(111));
transformation3 = registration(joint3(110), joint3(111));
transformation4 = registration(joint4(110), joint4(111));
for i = 111 to 220 do
    joint1(i) = interpolate(joint1(i), transformation1);
    joint2(i) = interpolate(joint2(i), transformation2);
    joint3(i) = interpolate(joint3(i), transformation3);
    joint4(i) = interpolate(joint4(i), transformation4);
end
transformation1 = registration(joint1(220), joint1(221));
transformation2 = registration(joint2(220), joint2(221));
transformation3 = registration(joint3(220), joint3(221));
transformation4 = registration(joint4(220), joint4(221));
for i = 221 to 330 do
    joint1(i) = interpolate(joint1(i), transformation1);
    joint2(i) = interpolate(joint2(i), transformation2);
    joint3(i) = interpolate(joint3(i), transformation3);
    joint4(i) = interpolate(joint4(i), transformation4);
end

```

3.5.2 Registration Framework

Through the categorization of the registration problem, voxel intensity based methods were chosen as the nature of the transformation. Voxel intensity based methods can all be described through a framework, which is seen in fig. 3.21.

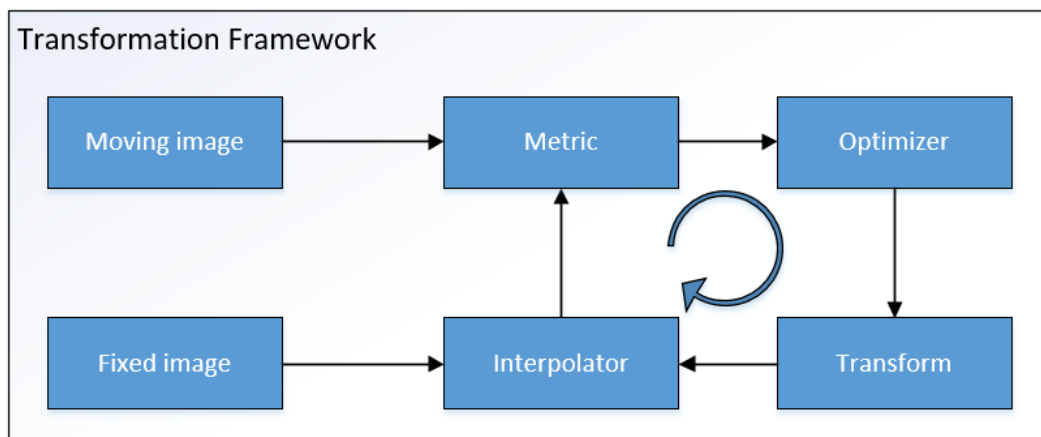


Figure 3.21: Registration framework.

The framework consists of several components, each having their own responsibilities in the registration process. The metric component calculates a similarity metric based on the moving and fixed image. The metric gives an indication of how similar the images are, and the process then finds the transformation that gives the best possible metric. A lot of different metrics exist, some of the simplest

are mean square, sum of squared difference, cross-correlation and ratio image uniformity [85], which are typically used for simpler registrations like monomodal registrations. The reason for this is that the image intensity values are similar, and a global point where the intensities are overlapping exists. If the images are multimodal, they might consist of significantly different intensity values, meaning no global intensity overlap exists. This problematic in multimodal image registration calls for other similarity metric, most commonly based on information theory. The first proposed method using mutual information in the images was proposed by Maes et al. [86]. This technique is based around Shannon's entropy, but other information theory metrics using other entropies exist [82].

The metric is optimized through the optimizer, and is typically an iterative process, finding either a maximum or minimum of the selected metric. Like the metric, several methods of optimization exist. The optimizer and its performance highly depends on both the metric and the transformation applied. If the images are monomodal and only a rigid transformation is applied, a local minimum or maximum is easily found. On the other hand, if images are multimodal and a curved transformation is applied, there may exist multiple local minima and maxima, making the optimization nontrivial. The transformation calculated by the optimization, can be either of the transformation types described in section 3.5. The complexity of the registration follows the amount of degrees of freedom in the transformation, making global rigid transformations the simplest and local curved transformations elaborate. The final component of the voxel intensity framework is the interpolation, which applies the transformation to the image. The interpolation is necessary as the transformation does not directly apply to pixel coordinates, therefore an approximating pixel placement is needed. Because of the approximation factor of the interpolation, some image information is changed or removed, thereby degrading the reliability of the image information. The interpolation can also have different types of complexity varying based on its type e.g. linear or spline interpolation. For this study a linear interpolator is used, as the transformation is simple.

3.5.3 Transform

The transform component creates the specific transformation which is to be applied to the moving image. As explained in the categorization of this studies registration section 3.5, the transformation used is rigid. A rigid transformation is the simplest transformation type and consist of translation and rotation. A translation i 2D can be specified accordingly to eq. (3.73) [81]:

$$\mathbf{T}_\delta\left(\begin{pmatrix} x \\ y \\ 1 \end{pmatrix}\right) = \begin{pmatrix} 1 & 0 & \delta_x \\ 0 & 1 & \delta_y \\ 0 & 0 & 1 \end{pmatrix} \begin{pmatrix} x \\ y \\ 1 \end{pmatrix}, \quad (3.73)$$

where $\mathbf{T}_\delta\left(\begin{pmatrix} x \\ y \\ 1 \end{pmatrix}\right)$ is the translated coordinates for x and y . The parameters δ_x and δ_y are the translations in x and y direction, respectively. A rotation transformation is achieved through eq. (3.74) [81]:

$$\mathbf{T}_\theta\left(\begin{pmatrix} x \\ y \\ 1 \end{pmatrix}\right) = \begin{pmatrix} \cos \theta & -\sin \theta & 0 \\ \sin \theta & \cos \theta & 0 \\ 0 & 0 & 1 \end{pmatrix} \begin{pmatrix} x \\ y \\ 1 \end{pmatrix}, \quad (3.74)$$

where θ is the degree of rotation, from the origo of the image. A combined rigid transformation is achieved through a matrix multiplication as seen in eq. (3.75):

$$\mathbf{T}_{rigid} \begin{pmatrix} x \\ y \\ 1 \end{pmatrix} = \begin{pmatrix} \cos \theta & -\sin \theta & 0 \\ \sin \theta & \cos \theta & 0 \\ 0 & 0 & 1 \end{pmatrix} \begin{pmatrix} 1 & 0 & \delta_x \\ 0 & 1 & \delta_y \\ 0 & 0 & 1 \end{pmatrix} \begin{pmatrix} x \\ y \\ 1 \end{pmatrix}. \quad (3.75)$$

The order of multiplication of the rotation and translation matrices, specifies the appliance order of the transformation.

3.5.4 Metric

The metric determines the similarity in the moving and the fixed images, and is either maximized or minimized through transformation and optimization. Through the preliminary research and development study [84], several different metrics were tested, including mean square, correlation coefficient and mutual information. Through various experiments, the mean square metric, was deemed best based on the results. For this study this metric is therefore selected. The mean square metric calculates the mean squared intensity difference between the fixed and moving image. The metric $J(\mathbf{T}_{rigid})$ can be formulated as a function of the applied transformation as seen in eq. (3.76):

$$J(\mathbf{T}_{rigid}) = \frac{1}{M \cdot N} \sum_{i=1}^M \sum_{j=1}^N (\mathbf{I} - \mathbf{T}_{rigid}(\hat{\mathbf{I}}(i, j)))^2, \quad (3.76)$$

where $i \in 1, 2, \dots, M, j \in 1, 2, \dots, N$ are indices of an $M \times N$ image, the moving image is $\hat{\mathbf{I}}$ and the fixed image is \mathbf{I} .

3.5.5 Optimizer

The optimizer is responsible of finding the best possible transformation that gives the best metric. Through the preliminary research and development study [84] two different optimizers was evaluated, namely gradient decent and regular step gradient descent. Gradient decent is one of the most used optimizers existing, and is a first-order optimization, that optimizes towards a local minimum using the gradient of a cost function. In this setup the cost function is the metric calculation. The gradient decent calculation of a new transformation matrix through each iteration is seen in eq. (3.77):

$$\mathbf{T}_{rigid} = \mathbf{T}_{rigid} - \alpha \frac{\partial}{\partial \mathbf{T}_{rigid}} J(\mathbf{T}_{rigid}), \quad (3.77)$$

where \mathbf{T}_{rigid} is the rigid transformation performed on the image, $\frac{\partial}{\partial \mathbf{T}_{rigid}} J(\mathbf{T}_{rigid})$ is the gradient of the metric, thereby ensuring that the optimizer travels towards the minimum of the metric value. The learning rate α regulates the optimizers convergence rate towards the local minimum. If the learning rate is too high, the optimizer might surpass the minimum, thereby never converging, and likewise, if too low never reach the minimum. Along with the gradient descent is a gradient magnitude tolerance, controlling the stopping criteria for the optimizer. When the gradient is smaller than the gradient magnitude tolerance, the optimizer stops. The learning rate for the normal gradient descent is typically hard to choose, therefore different other gradient descent optimizer variants exist, each having their own learning rate calculation. One of those is the regular step gradient descent, which reduces the learning rate with a relaxation factor, each time the direction of the gradient is changed, thereby resulting in a better convergence [87]. As a result of the preliminary research and development study [84], the regular step gradient descent was deemed best, and is therefore used in this study. The values for the parameters of the regular step gradient decent is seen in table 3.2. The constant values were based on both manufacturer values [87] and initial experimentation testing.

Table 3.2: The constant parameters for the registration optimizer

	Final
Maximum step length	0.3
Maximum iterations	140
Relaxation factor	0.3
Gradient Magnitude	1e-5

3.5.6 Registration Validation

A difficult process in the registration of medical images is the validation of the registration. This is a difficult matter because of the typical lack of a golden reference used for comparison. It is typically a subjective evaluation of the registration based on a visual inspection. Medical image registration evaluation consist of many factors, which were presented by Maintz et al. [83]. They presents a list consisting of eight different factors and catagories of validation. The categories can be seen below in section 3.5.6.

1. Precision
2. Accuracy
3. Robustness/stability
4. Reliability
5. Resource requirements
6. Algorithm complexity
7. Assumption verification
8. Clinical use

The precision and accuracy of medical image registration are the most important factors. The accuracy indicates how close the registration is to the ground truth, and the precision represents the consistency of the registration in its prediction capabilities. The robustness of a registration explains how well it performs with variations in the input data e.g. different orientations, noise and artifacts. The reliability of a registration defines its ability to produce the same results for the same type of data. Resource requirements indicates the needed resources for the registration to perform e.g. images or personal. The algorithm complexity is concerned with both the space and time complexity of the registration, which is highly related to the application area e.g. real time applications. Assumption verification is related to eventual mathematical assumptions made, based on the registration, which needs to be verified, in order to prove the collected verification of the registration. Lastly, the clinical use refers to the need of the registration in clinical context [83].

3.6 Erosion Detection and Quantification

The final step of the overall proposed method is the erosion detection and quantification. The detection is the ability to locate the erosions in the joints, whereas the quantification is the determination of relevant metrics regarding the erosions. In order of an erosion to be detected, a clear definition is necessary, as not all cortical breaks are considered a result of RA, e.g. cysts which are non-pathological break. A clear definition of a pathological cortical bone disruption as a result of RA in HR-pQCT images has been accepted by the SPECTRA (Study group for xtrEme-Computed Tomography in Rheumatoid Arthritis) collaboration. The definition is primarily dedicated manual erosion detection, and consists of five criteria, which must be satisfied for a cortical break to be considered a result of RA. These five criteria are presented in list 3.3 [13]:

List 3.3: SPECTRA erosion criteria list.

1. Presence of a definite interruption in the cortical bone.
2. Cortical break must extend over at least 2 consecutive slices.
3. Cortical break must be detectable in 2 perpendicular planes.
4. Loss of underlying trabecular bone at the cortical break.
5. Nonlinear in shape (to differentiate from vascular channels penetrating the cortices.)

These five criteria will be used for the proposed automatic detection method. In addition to the guidelines corresponding to erosion detection, the SPECTRA collaboration also accepted procedures for 2D erosion quantification. These procedures include measuring of the width and depth of a cortical break. The two procedures are listed in list 3.4 [13]:

List 3.4: SPECTRA erosion quantification procedures list.

1. The maximum width of the cortical break is determined by drawing and measuring the length of a straight line between the 2 margins of the break, in both axial and corresponding perpendicular planes independently.
2. The depth measurement of the cortical break is taken at an 90° angle to the drawn width line, extending to the deepest point in the erosion.

For the proposed erosion quantification method, these procedures will be used to define the width and depth of the erosions. In addition to the width and depth, the volume and centroid of the erosions are to be determined as well.

3.6.1 Proposed Erosion Detection and Quantification Method

Using the segmented and registered binary images as a starting point, the erosion detection and quantification method is based upon a series of image manipulation steps, primarily morphological operations as presented in section 3.4.4. The steps defining the detection method is described first, followed by the quantification method.

Detection

The detection method is presented through four main steps, which are explained below, and presented in fig. 3.22.

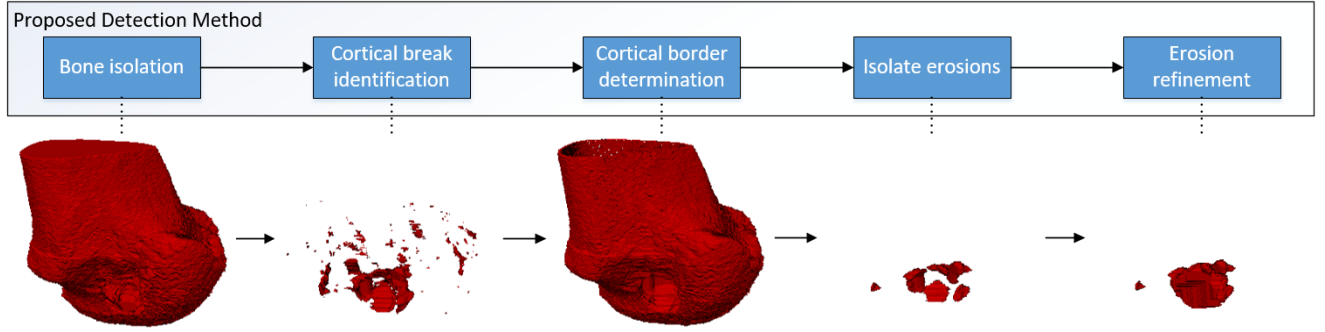


Figure 3.22: Overview of the main steps in the proposed detection method. First step consists of the isolation of the individual bones, secondly identification of cortical breaks followed by the third step which is determination of the cortical border. Based on the cortical border, step four consists of isolation of erosions meeting SPECTRA criteria, and lastly a refinement process to obtain the true volumes of the detected erosions.

Step 1 - Cortical break identification: The first step of the detection method finds all cortical breaks present in the segmented and registered binary dataset, thereby providing a basis for all plausible erosions. The identification of the cortical breaks are based upon the usage of the morphological close operation, which closes all cavities in the segmented periosteal surface.

To avoid erroneous closing in the regions of the scan containing joint changes, each finger bone is isolated and manipulated independently, as seen in first step of fig. 3.22. During this process, it was decided to remove the 20 slices closest to the joint change for both bones within the joint. The reason for this is twofold, first to create such a large separation between the objects, so that closing will not connect the two, and secondly to avoid incorrect detections within this area due to the low image quality seen for joint changes. This decision introduces a limitation of the method, which disables it from detecting erosions in these areas. However, due to the image quality, the reliability of such a detection would be low if introduced.

Because of eventual registration error, which is not corrected during the registration process, each of the independent joints are manipulated in the axial slice planes 0 – 110, 111 – 220 and 221 – 330.

Each of these bone structures are applied with 2D morphological close operations, using a disk structuring element with a radius of 20 voxels, in each plane (axial, coronal and sagittal) resulting in three independently closed structures. In order to meet item 3 in list 3.3, each element detectable in two of the closed dimensions are kept, which is ensured through eq. (3.78):

$$\mathbf{B}_{Closed}(i, j) = \mathbf{B}_{ClosedX}(i, j) \cdot \mathbf{B}_{ClosedY}(i, j) + \mathbf{B}_{ClosedX}(i, j) \cdot \mathbf{B}_{ClosedZ}(i, j) + \mathbf{B}_{ClosedY}(i, j) \cdot \mathbf{B}_{ClosedZ}(i, j), \quad (3.78)$$

where $i \in 1, 2, \dots, M$ $j \in 1, 2, \dots, N$ of an $M \times N$ image, $\mathbf{B}_{Closed}(i, j)$ is the resulting closed binary image, $\mathbf{B}_{ClosedX}(i, j)$ is the binary image closed in axial plane, $\mathbf{B}_{ClosedY}(i, j)$ is the binary image closed in coronal plane and $\mathbf{B}_{ClosedZ}(i, j)$ is the binary image closed in sagittal plane.

In order to isolate the cortical breaks, the closed structure is subtracted from the original non-closed structure, as seen in the second step of fig. 3.22. Due to small irregularities in the periosteal surface structure, a large amount of undesired structures are present in the isolated cortical breaks

as a result of the close operations. To obtain a cleaned set of cortical breaks, a 3D cleaning of these structures is applied. The structural cleaning is done by only keeping voxels, of which 14 or more of its surrounding 3-by-3-by-3, 26-connected neighbors are other binary true voxels, which result is the second step of fig. 3.22.

Step 2 - Cortical border determination: The second step concerns the determination of the cortical thickness. The cortical border is found by first combining binary bone structures with the set of cavities produced in step 1, resulting in a solid version of step 3 of fig. 3.22. These closed bones are seen as the complete periosteal surface without any cortical breakage, thereby creating a basis from which the cortical border is determinable. Using the assumption made by Peters et al. [5] defining the average cortical thickness in the MCP joints as $0.39mm$, the thickness of the cortical border in the images is defined as 4 voxels equivalent to $0.328mm$ [5]. By using the morphological erode operation with a sphere structuring element of radius 4 voxels, followed by a subtraction from the original binary structure, the cortical border is obtained as seen in step 3 in fig. 3.22.

Step 3 - Isolate erosions: The third step of the erosion detection, is to isolate cortical breaks meeting the criteria item 1 and item 4 listed in list 3.3. This step starts by subtracting the cortical borders produced in step 2 from the cortical breaks identified in step 1, which removes all cortical breaks not reaching the trabecular bone structures, as seen in step 4 of fig. 3.22. This procedure ensures item 1 and item 4 in list 3.3 is satisfied. A clear definition of how much trabecular bone loss is necessary for an cortical break to be a erosion is not specified. Thus an assumption is made defining that an erosion shall have a trabecular bone loss volume of minimum 100 voxels. This parameter can be changed to regulate the threshold of trabecular loss for the detected erosions. To fulfill this assumption, the minimum object removal method defined in section 3.4.4, is used to remove all erosions with a trabecular bone volume of less than 100 voxels, as seen in fig. 3.22. The remaining objects are hereafter considered valid erosions. These valid erosions are then applied with their removed cortical border, to return them to their original detected volumes, as seen in step 4 of fig. 3.22.

Step 4 - Erosion refinement: The last step of the proposed detection method is the refinement of the detected erosions. The morphological close operation utilized in step 1, merely closes minor erosions completely, resulting in large erosions being unclosed. To solve this, a refinement step with the purpose of completely closing the erosions were added to the chain.

During this step, the original structure is first filled through a 3D morphological close operation, with a sphere structuring element of radius 50 voxels. The 3D closed structure is then subtracted with the original structure, resulting in a set of large filled areas. Next, a run-through is made to check if two or more detected erosions from step 3 is located within a large closed volume. In such a scenario, an assumption is made that the given volume is a single large unclosed erosion, resulting in an addition of the larger volume to the erosion structure. This process is illustrated on fig. 3.22 step 4 to 5.

Due to noisy elements, such as patient motion and ring artifacts, some erosions were erroneous detected on the outside of the true periosteal surface. In order to eliminate these false positives, the width and depth measurements of the erosions, which are described further in this section, was utilized. First, the coordinates of the deepest point of the erosion is found as P_1 on fig. 3.23, and P_2 as the bone center coordinates of the respective image slice. Now, by comparing the distance between the two points, with the distance from the center coordinate P_2 to the outer coordinates of the erosion width measurement, it can be determined whether the erosion is located outside or inside of the cortical border. In such as case, as illustrated on fig. 3.23, where the length of the blue dotted line exceeds the length of the maximum of the two black dotted lines, the erosion is discarded.

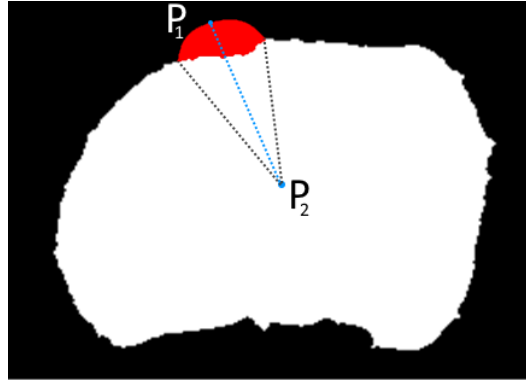


Figure 3.23: Illustration of refinement process to eliminate erosions located outside the cortical border. P_1 is the deepest voxel of the red erroneously detected erosion, P_2 represents the center coordinates of the bone in the axial plane. The lengths marked with black dots illustrates distances from the center coordinates to the two outer coordinates of the erosion width measurement. Lastly, the blue dotted line shows the distance from the two points.

Finally, the remaining erosions are used to extract the associated properties as described below.

Quantification

The quantification method should be able to detect four different properties of the detected erosions, namely the location through center coordinates, volume, width and depth.

Coordinates: The quantification method should be able to locate the placement of the erosion, in regards to both the MCP joint and the location on the bone. This is obtained by determining the 3D center coordinates of the erosion objects provided by the detection. These coordinates can hereafter be used to specify the location within the dataset.

Volume: To quantify the volume of the individual erosions, the regional properties of the detected objects are found, specifying the volume, which are then converted from voxels to mm^3 . The volume is found as the total sum of all voxels within the detected erosion.

Width: The maximum axial width of the erosions is found in accordance with the SPECTRA collaborations procedure item 1 in list 3.4, by measuring the direct length between the cortical break's periosteal surface points. This length is calculated in the axial plane in the axial center of the erosion. The width is calculated using the distance formula between two points $P_1 = (i_1, j_1)$ and $P_2 = (i_2, j_2)$ eq. (3.79):

$$w(P_1, P_2) = \sqrt{(i_2 - i_1)^2 + (j_2 - j_1)^2}. \quad (3.79)$$

Depth: The depth is found, likewise the width in accordance with the SPECTRA collaborations procedure item 2 in list 3.4. The depth is found as the maximum orthogonal line drawn from the earlier obtained width, reaching the inner tubercular border of the erosion. The following equation defines the distance between a point perpendicular to a line, defined by two points, is given by eq. (3.80):

$$d(P_1, P_2, (i_0, j_0)) = \frac{|(j_2 - j_1)i_0 - (i_2 - i_1)j_0 + i_2j_1 - j_2i_1|}{\sqrt{(j_2 - j_1)^2 + (i_2 - i_1)^2}}, \quad (3.80)$$

where $P_1 = (i_1, j_1)$ and $P_2 = (i_2, j_2)$ defines the line for the width found in eq. (3.79) and thereby the depth is found as the maximum distance to the point (i_0, j_0) .

3.6.2 Erosion Detection and Quantification Validation

The validation of the proposed erosion detection and quantification method is twofold. Both detection and quantification is validated individually, to fully verify the methods effectiveness.

A golden reference manual erosion detection and quantification, which is used to validate the methods, were conducted by domain personal. The procedure of the manual detections is carried out in accordance with the SPECTRA criteria and principles listed in lists 3.3 and 3.4. In total 104 individual datasets was covered in the manual detection, deriving from 44 patients. For each of these datasets, each erosion present were recorded with a centroid coordinate, along with width, depth and volume. To cover the most important metrics in both detection and quantification capabilities different methods were used to validate these.

Detection

The detection capabilities of the method defines the ability to correctly find erosions. The validation of the method is based on how many correct and incorrect detections the method produces. For this, two different metrics are used, namely sensitivity and precision. The sensitivity, also know as the true positive rate, is the proportion of correctly identified erosions, and is given by eq. (3.81):

$$Sensitivity = \frac{TP_{erosions}}{(TP_{erosions} + FN_{erosions})}, \quad (3.81)$$

where $TP_{erosions}$ is the amount of correctly identified erosions and $FN_{erosions}$ is the amount of incorrectly rejected erosions. The precision, also know as positive prediction value, measures the proportion of identified erosion which are correct identifications, and is given by eq. (3.82):

$$Precision = \frac{TP_{erosions}}{(TP_{erosions} + FP_{erosions})}, \quad (3.82)$$

where $TP_{erosions}$ is the amount of correctly identified erosions and $FP_{erosions}$ is the amount of incorrectly identified erosions. Since the manual detections is not an exhaustive examination of all erosions in the individual datasets, but merely a indicator of examples of erosions, the expected performance of the detection method should have a high sensitivity and a low precision.

Quantification

Each of the four quantification metrics shall be validated independently. For the volume, width and depth the accuracies and precisions of the quantification method are determined. The accuracy specifies how close the quantification method is to the golden reference. The precision specifies the consistency of the quantification method. The accuracy is specified through the accuracy error AE , and is calculated as the error between the mean of the method and the golden reference, which is given by eq. (3.83):

$$AE = \mu_{predicted} - \mu_{observed} = \frac{1}{N} \sum_{i=1}^N \mathbf{m}_{predicted}(i) - \frac{1}{N} \sum_{i=1}^N \mathbf{m}_{observed}(i), \quad (3.83)$$

where N is the sample size, $\mathbf{m}_{predicted}$ is the golden reference vector of a specific metric and $\mathbf{m}_{observed}$ is the vector of a specific metric calculated by the method. The accuracy error is also calculated as a ratio of the error AER , which gives a better overview of the deviation percentage of the method, which is given by eq. (3.84):

$$AER = \frac{AE}{\mu_{predicted}} \cdot 100\% = \frac{AE}{\frac{1}{N} \sum_{i=1}^N \mathbf{m}_{predicted}(i)} \cdot 100\%, \quad (3.84)$$

where AE is as specified in eq. (3.83). The precision of the quantification is found through the precision error which is calculated as the root mean square. The precision error PE formula is seen in eq. (3.85):

$$PE = \sqrt{\frac{1}{N} \sum_{i=1}^N \left(\mathbf{m}_{observed}(i) - \mathbf{m}_{predicted}(i) \right)^2}. \quad (3.85)$$

The precision error is likewise calculated as a ratio. The formula for the precision error ratio PER is seen eq. (3.86):

$$PER = \sqrt{\frac{1}{N} \sum_{i=1}^N \left(\left(\frac{\mathbf{m}_{observed}(i) - \mathbf{m}_{predicted}(i)}{\mathbf{m}_{observed}(i)} \right)^2 \right)} \cdot 100\%. \quad (3.86)$$

These metrics AE, AER, PE and PER are used for the volume, width and depth. For the centroid, another approach is taken. Here the absolute distance error is calculated between the golden reference centroid and the centroid acquired by the method. This distance error $dist(P_{predicted}, P_{observed})$ is calculated accordingly to eq. (3.87):

$$dist(P_{predicted}, P_{observed}) = \sqrt{(i_{observed} - i_{predicted})^2 + (j_{observed} - j_{predicted})^2 + (k_{observed} - k_{predicted})^2}, \quad (3.87)$$

where $P_{predicted} = (i_{predicted}, j_{predicted}, k_{predicted})$ and $P_{observed} = (i_{observed}, j_{observed}, k_{observed})$ is the golden reference centroid and the centroid found by the method, respectively. Using these distance errors the accuracy $AE_{centroid}$ is found as the mean using eq. (3.88):

$$AE_{centroid} = \frac{1}{N} \sum_{i=1}^N dist(\mathbf{p}_{predicted}(i), \mathbf{p}_{observed}(i)), \quad (3.88)$$

where $\mathbf{p}_{predicted}$ and $\mathbf{p}_{observed}$ is the vectors of centroids of the golden reference and method respectively. The precision of distance errors $PE_{centroid}$ is found as the root mean square, as formulated in eq. (3.89):

$$PE_{centroid} = \sqrt{\frac{1}{N} \sum_{i=1}^N dist(\mathbf{p}_{predicted}(i), \mathbf{p}_{observed}(i))^2}. \quad (3.89)$$

These presented accuracy and precision calculations should provide a reliable indication of the quantifications capability in relation to the manual method.

Chapter 4

Experiments and Results

The following chapter covers the experiments and results related to the validation of the proposed method and its subcomponents. Each experiment is presented, first along with its associated component, execution description and evaluation metrics, whereafter the results concerning the experiment is presented and discussed, to give a better overview of the individual validation. To give an overview of the manual labeling used for the segmentation validation, section 4.1 describes how these came to existence.

4.1 Manual Labeling

To enable parameter adjustment as well as method selection of the proposed hybrid segmentation method, a ground truth training dataset was needed. It was decided to adjust the parameters and methods in a supervised manner, utilizing only labeled data for the method adjustment and selection process.

The amount of ground truth data available within this process, dictates the covered amount of features, and thereby yields the robustness of the resulting method. However, as manual labeling is considered a very time-consuming task, the amount of data to be labeled were to be kept at an absolute minimum. To quantify the needs regarding the data selected for the segmentation validation, a list of requirements were constructed, which is seen in section 4.1:

1. The data shall cover at least an entire dataset, in order to verify the segmentation over a complete scan.
2. The data shall cover each noted noise artifact type as presented in sections 3.1 and 3.4.1, in order to verify the robustness of the segmentation.
3. The general image quality of the data shall represent the worse case of the expected image quality that the method shall be able to process.
4. The data shall contain at least one case of erosions.

Based upon these requirements an analysis of the datasets were produced, resulting in the selection of a specific training dataset. The selected dataset fulfills the requirements presented above, which can be visually seen in appendix A.

The manual labeling were conducted using the MATLAB Image Labeler [88] from the Computer Vision Toolbox. The tool allows for pixel-wise ground truth labeling of images, ensuring a high precision. To ease the labeling process, the tool offers a flood-filling device, which is capable of

flooding larger sections of the image based on pixel-intensities, whereafter manual adjustments can be used.

4.2 Segmentation Experiments and Results

The following section presents the experiments and results conducted in relation to the proposed segmentation method. The proposed method is tested as a chain of the internal segmentation components.

Firstly, experiments concerning the performance of the individual thresholding methods, presented in section 3.4.3, is conducted. Secondly, the morphological operations are tested in conjunction with each of the thresholding methods in section 4.2.2. The reason for doing so, is that the performance of the morphological operations might change for the individual thresholding methods, even though their individual performance seems disadvantageous for the combined method. Based on these experiments, a selection of a thresholding method and morphological operation parameters is produced. The next set of experiments is associated with the selection of both method and individual parameters for the active contour, and is presented in section 4.2.3. These are conducted on the basis of the results found for the thresholding and morphological operations. The reason for this, is that the active contours performance is highly dependable on the initial contour [69, 70], as a better basis leads to performance increase. An experiment proving this statement, is also performed and presented within this section. Finally, in section 4.2.4, an experiment visually validating the overall segmentation performance is conducted, thereby giving an overview of the limitations of the proposed segmentation method. Each of the segmentation steps are tested using the validation metrics, presented and explained in section 3.4.6, in combination with the manual labeled image dataset, explained in section 4.1.

4.2.1 Thresholding Experiments and Results

The first step of the proposed segmentation method is the thresholding, which has the purpose of creating an initial segmented contour, which is further closed by the morphological operations step. It is therefore important to find a thresholding method which is able to create a good initial contour, without the minimum noise inclusion.

Experiment - Thresholding: For this experiment, each of the methods presented in section 3.4.3, namely the Gaussian characteristic, Entropy, Otsu and Niblack thresholding, is tested. Through the experiments, each of the methods are applied on each individual image slice in the dataset corresponding to the manual labeled dataset. Each segmented image slice for each segmentation method is validated with the volume-based metrics, as presented in section 3.4.6. Statistics are calculated on basis of each image slice volume-based metrics, namely the mean and standard deviation. The purpose of the experiment, is to find the thresholding method producing the highest TPR segmentation and lowest FPR segmentation. Because of this, receiver operating characteristics (ROC) curve is used to present the results for each method. A ROC curve presents the FPR as a function of TPR, meaning the closer a result is to the upper left corner, the better it is. The k value for the Niblack method is variable, and was selected to the value of 1.5, as this produced the best results.

Results - Thresholding: A ROC curve of the mean TPR and FPR for each of the thresholding methods is presented in fig. 4.1.

It is noteworthy that the ROC curve is zoomed on the results, as its axes normally reaches from 0 to 1. It is seen that the Gaussian characteristic, Entropy and Niblack thresholding methods have

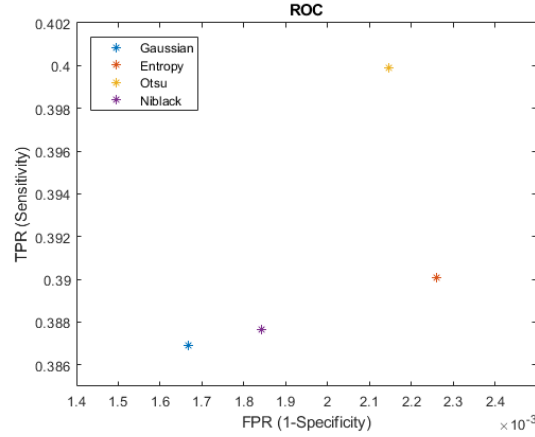
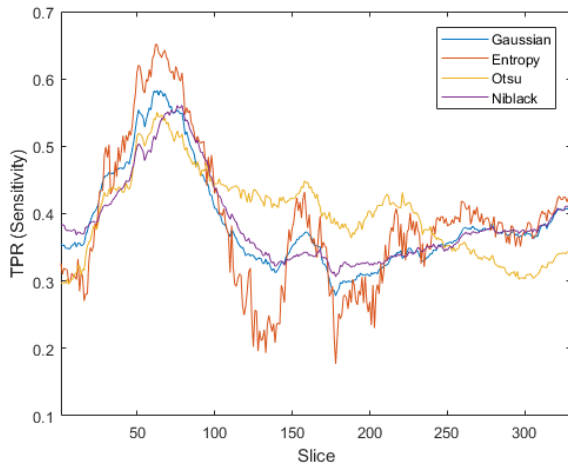
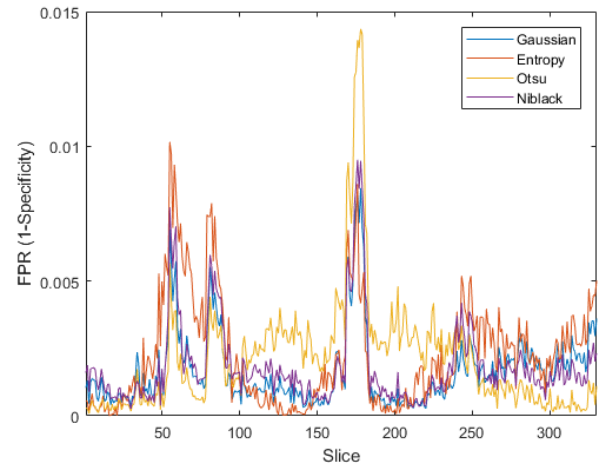


Figure 4.1: ROC curve of the mean values for the four thresholding methods Gaussian characteristic, Entropy, Otsu and Niblack. The ROC curve represent the sensitivity as a function of 1-specificity.

approximately the same TPR but differs in their FPR. From this the Gaussian characteristics method is determined to have the best performance. The Otsu outscores the other approaches in TPR but still has a relatively high FPR compared to the other methods. In addition, it should be noted that all four methods are very similar, when considering the FPR, as they only differ in a scale of 10^{-3} .



(a) The TPR as function of the image slice



(b) The FPR as function of the image slice

Figure 4.2: The TPR fig. 4.2a and FPR fig. 4.2b as function of the image slice for each of the thresholding methods; Gaussian characteristics, Entropy, Otsu and Niblack

Seen on fig. 4.2a is the TPR for each slice for each method. Likewise on fig. 4.2b is the FPR for each slice for each method. It is seen that the Gaussian characteristic and Niblack methods are very similar in their values and are more stable in both TPR and FPR than the Otsu and Entropy methods. There are relatively high changes in slice 45 – 75, 120 – 140 and 175 – 210. These indicate the joint shifts in the MCP, where the manual labeling and thresholding are imprecise as a result of overlapping intensity values, as described in section 3.4.1. Based on the results presented through this experiment, the Gaussian characteristics thresholding method is considered the most promising. However, the other methods might show better results, after appliance of the morphological operation step.

All volume-based metric mean and standard deviation results for each thresholding method is seen in table 4.1.

Table 4.1: Mean and standard deviation for each thresholding method for each volume-based metric.

	<i>Gaussian</i>		<i>Entropy</i>		<i>Otsu</i>		<i>Niblack</i>	
	Mean	Std	Mean	Std	Mean	Std	Mean	Std
TPR	0.3869	0.0733	0.3901	0.1046	0.3999	0.0629	0.3876	0.0637
TNR	0.9983	0.0014	0.9977	0.0020	0.9979	0.0022	0.9982	0.0016
FPR	0.0017	0.0014	0.0023	0.0020	0.0021	0.0022	0.0018	0.0016
FNR	0.6131	0.0733	0.6099	0.1046	0.6001	0.0629	0.6124	0.0637
DICE	0.5491	0.0697	0.5458	0.0987	0.5626	0.0618	0.5502	0.0601

4.2.2 Morphological Experiments and Results

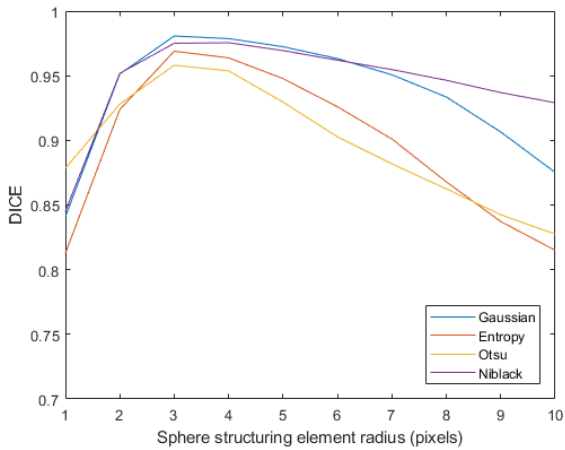
The next part of the proposed segmentation method is the morphological operations, which includes four internal steps, as presented in section 3.4.4. The purpose of the morphological operations, is to fully close the joint structures in the images on basis of the initial thresholding segmentation. The morphological operations shall therefore produce the highest possible TPR, with as little FNR as possible. For the morphological operations two uncertainties exist, which needs to be analyzed through experiments. These uncertainties are the size of the structuring element for the dilation and erosion and the minimum object threshold. This section will explain the experiments and the results associated with these uncertainties.

Experiment - Sphere structuring element radius: As explained in section 4.2.1, each thresholding method might perform differently when conjoined with the morphological operations. This means that each of the thresholding methods, Gaussian characteristics, Entropy, Otsu and Niblack is tested in this experiment. The experiment is carried out on each image slice in the original dataset corresponding to the manual segmented dataset. First, the thresholding methods is applied followed by the morphological operation steps, absent the minimum object removal. Each segmented image slice is validated through the volume-based metrics, presented in section 3.4.6. The mean and standard deviation are calculated for the volume-based metrics for each thresholding method. The above explained procedure is carried out for different radii for a sphere structuring elements. The sphere structuring element radius for each thresholding method is varied from 1 to 10 voxel and increased 1 voxel per step.

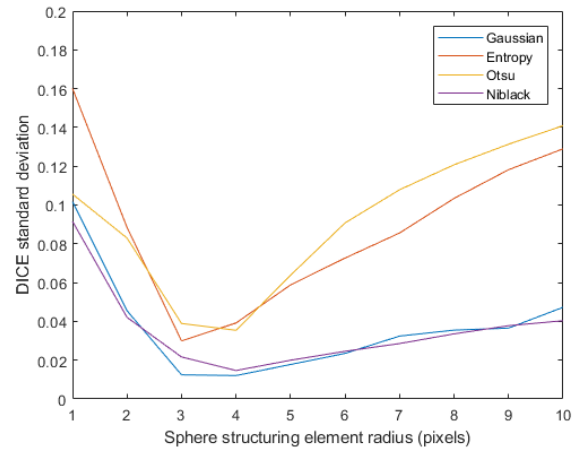
Results - Sphere structuring element radius: The mean DICE value and the associated standard deviation, related to each of the thresholding methods for each structuring element radii, is seen in fig. 4.3.

As seen on the figure, each of the thresholding methods drastically improves their mean DICE values up to a sphere structuring element radius of 3 pixels. All structuring element radii above 3 voxels degrades the mean DICE value. The standard deviation for the structuring element radii is also best around 3 – 4 and increases hereafter. The reason for this might be, that the sphere structuring element with a radius of 3 voxels, precisely fills the joint structures. This means that all structuring element radii above adds false contour, thereby degrading the mean DICE value as the FPR increases. This is also seen in the FPR and the TPR, plotted as a function of the structuring element radii, seen in fig. 4.3.

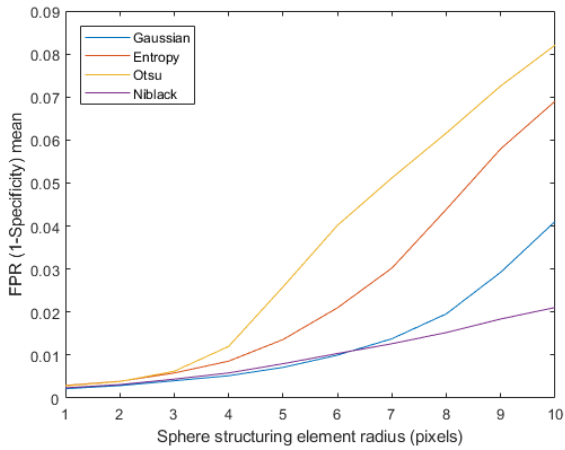
The mean TPR fig. 4.3d increases and approach 1 around the structuring element size of 3 – 4 pixels, for the Gaussian characteristic, Entropy and Niblack. The Otsu on the other hand, first approximates around a structuring element size of 6. The increase in TPR mean is caused by the filling and closing of the morphological operations. The FPR fig. 4.3c also increases, as the cavities and details of the structures also gets filled.



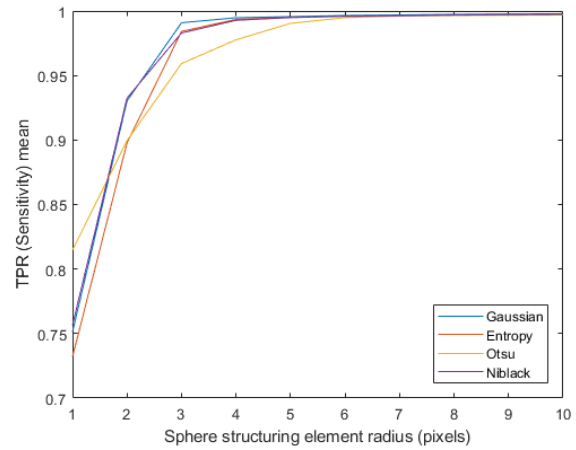
(a) The DICE mean of the sphere structuring element radius experiment.



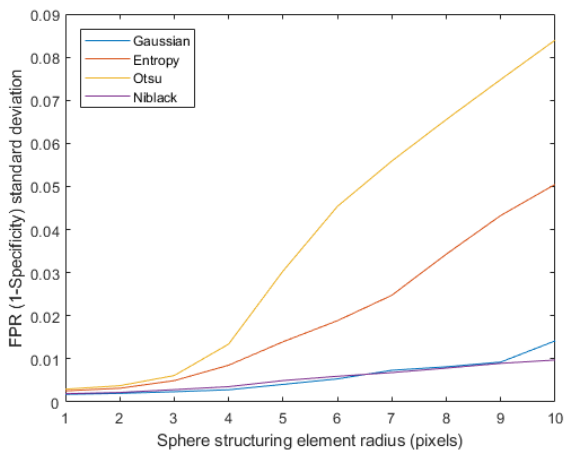
(b) The DICE standard deviation of the sphere structuring element radius experiment.



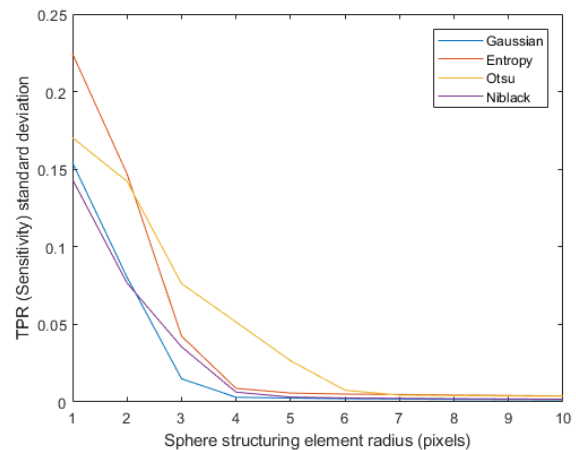
(c) The FPR mean of the sphere structuring element radii.



(d) The TPR mean of the sphere structuring element radii.



(e) The FPR standard deviation of the sphere structuring element radii.



(f) The TPR standard deviation of the sphere structuring element radii.

Figure 4.3: Mean DICE value fig. 4.3a, DICE standard deviation fig. 4.3b, mean FPR fig. 4.3c, mean TPR fig. 4.3d, standard deviation FPR fig. 4.3e and standard deviation TPR fig. 4.3f of a dataset for the thresholding methods; Gaussian characteristics, Entropy, Otsu and Niblack, followed by morphological operations with different radii sphere structuring element.

Especially the Otsu and the Entropy thresholding methods have a high increase in FPR, which is probably a result of noise from the thresholding, which then gets included into the structure. The standard deviations for the FPR and TPR figs. 4.3e and 4.3f follow the mean values, where the FPR standard deviation increases and the TPR standard deviation decreases. Based on this experiment, the Gaussian characteristic thresholding approach still produces the best overall DICE value.

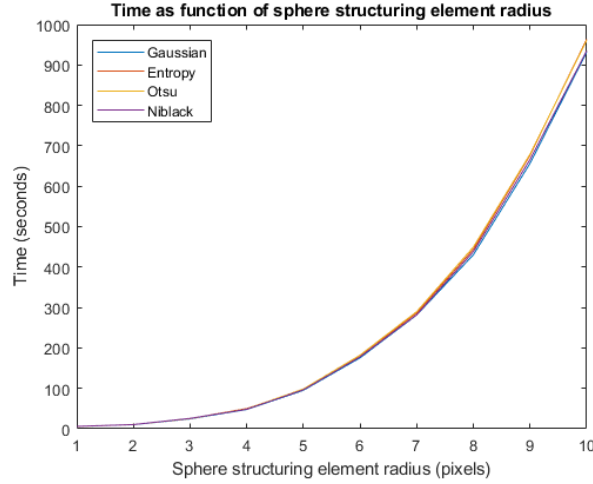


Figure 4.4: Mean DICE value fig. 4.3a and Standard deviation fig. 4.3b of a dataset for the thresholding methods; Gaussian characteristics, Entropy, Otsu and Niblack, followed by morphological operations with different radii sphere structuring element

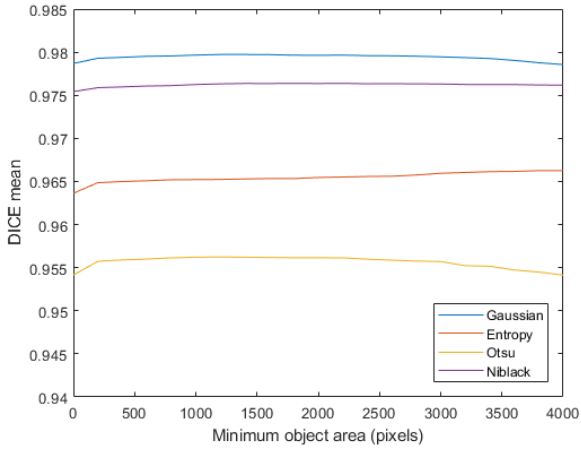
The execution time of the morphological operation as function of the radii of the sphere structuring element is seen in fig. 4.4. The time for each of the thresholding method is the same as expected, and the time complexity of the radius follows $\mathcal{O}(n^3)$ as the volume of the sphere structuring element as function of the radius is $V = 4/3 \cdot r^3$, where r is the radius and V is the volume.

Experiment - Minimum object threshold: The second experiment for the morphological operations, is to find the best minimum object threshold for the minimum object removal which is applied after the erosion step. The purpose of the minimum object removal, is to remove noise objects from the contour, thereby improving the true segmentation of the joints. This test is carried out, following the same procedure as the experiment explained above, only this time the minimum object removal is included. The threshold value is varied from 0 to 4000 pixels with a step size of 200 pixels. The morphological structuring size is kept constant at 4 for all four thresholding methods, as this value resulted in the best TPR.

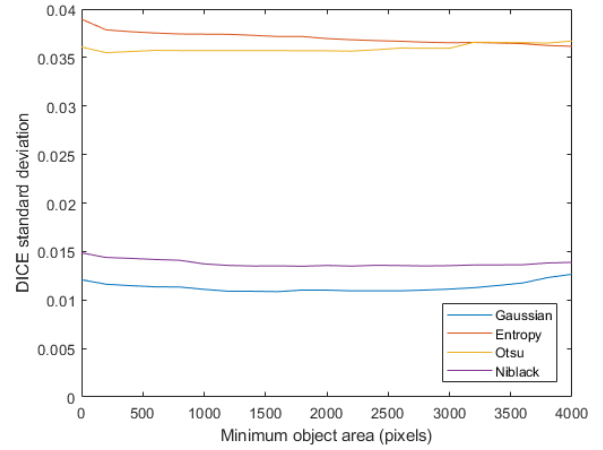
Results - Minimum object threshold: The DICE mean and standard deviation related to each of the thresholding methods for each minimum object threshold is seen in fig. 4.5.

Each of the thresholding methods is relatively constant for each minimum object threshold, each with a small improvement in the start and then a small degradation in the end. The same applies for the standard deviations which follows the mean values. The Gaussian characteristics method has the best overall mean value and the best overall standard deviation.

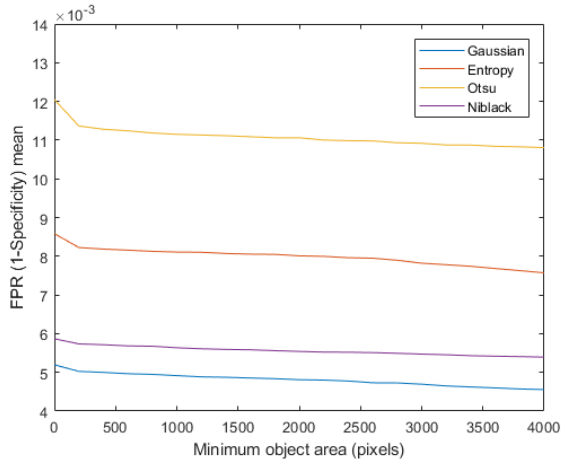
The TPR and FPR means for the minimum object threshold are seen in figs. 4.5c and 4.5d. The FPR and TPR degrades for each minimum object size. This is explainable in the fact that the minimum object removal, removes objects, which are both noise and actual structure. The standard deviations for the FPR and TPR are seen in figs. 4.5e and 4.5f, and they follow their corresponding mean values.



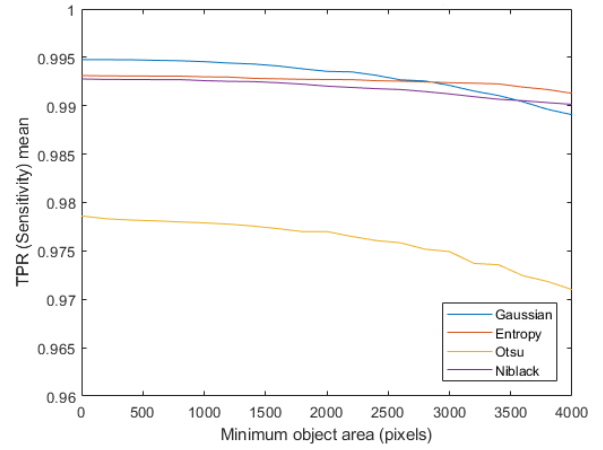
(a) DICE mean of the minimum object threshold.



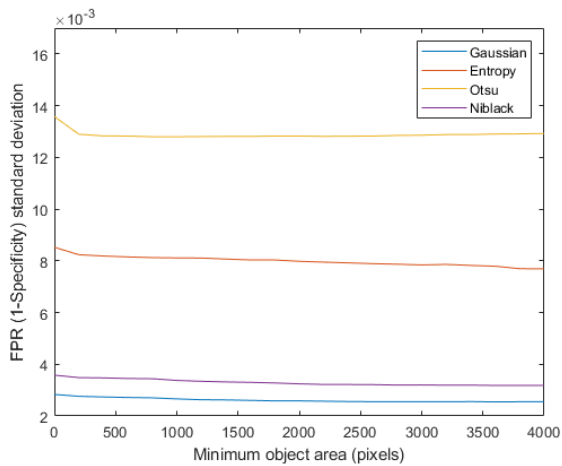
(b) DICE standard deviation of the minimum object threshold.



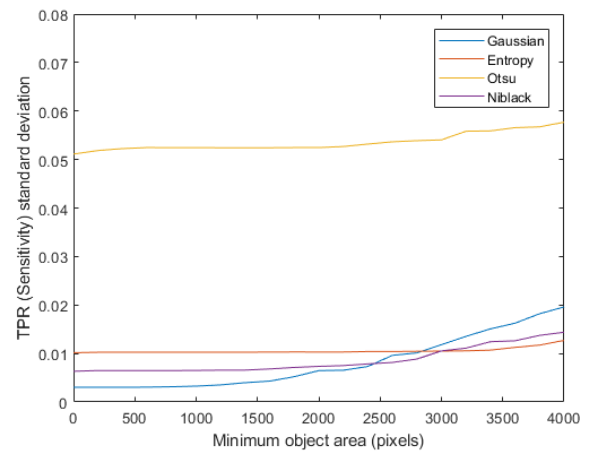
(c) The FPR mean for the minimum object thresholds.



(d) The TPR mean for the minimum object thresholds.



(e) The FPR standard deviation for the minimum object thresholds.



(f) The TPR standard deviation for the minimum object thresholds.

Figure 4.5: The DICE mean fig. 4.5a and standard deviation fig. 4.5b. Followed by the FPR mean fig. 4.5c, TPR mean fig. 4.5d, FPR standard deviation fig. 4.5e and TPR standard deviation fig. 4.5f for each of the thresholding methods; Gaussian characteristics, Entropy, Otsu and Niblack as function of the minimum object threshold.

Based on these presented results, the Gaussian characteristics method is still showing the best performance, leading to its selection for the final proposed segmentation method. The structuring element size is selected to 4, as this presented the best results, and finally the minimum object threshold is selected as 2000, as this shows most promising results. The final selected values and thresholding method is presented in table 4.2

Table 4.2: The final parameters for the thresholding and morphological operations in the segmentation method.

	Thresholding method	Structuring element radius	Minimum object threshold
Final Process	Gaussian characteristics	4	2000

4.2.3 Active Contour Experiments and Results

The final part of the proposed segmentation method is the active contour, which purpose is to finalize the segmentation mask, which was initialized by the thresholding and morphological operations. During the closing through morphological operations, some areas of the mask may exceed or elude from the actual periosteal surface, therefore border refinement is desired through active contour. To evaluate the optimum result of the active contour, volume-based as well as distance-based metrics are used, as presented in section 3.4.6.

Experiment - Parameter adjustment: The first experiment for the active contour, covers the parameter adjustment for the three methods presented in section 3.4.5, namely *Local CV*, *Local MS* and *Global CV*. Two parameters are variable in the local methods, the size of the localizing object given by the side length of a square window and the smoothing term α . For the global method, the localizing object is not present, and thus only the smoothing term is adjusted.

The tests are conducted by first applying the thresholding and morphological operations with the results produced in sections 4.2.1 and 4.2.2 on the original dataset, corresponding to the manual segmented dataset, and hereafter applying the three active contour methods individually. For the local methods, one parameter is kept constant while the other is varied. For the two local methods, the smoothing term is varied between 0 and 0.15 with an increase of 0.01 for each step, and the side length of the localizing object is varied between 0 and 20 pixels, increasing with a single pixel for each step. The smoothing term for the global method is varied between 0 and 4000, using a step size of 1000. The local methods are iterated 40 times for each test, whereas the global method is iterated 10 times.

To validate the parameters, each image slice within the dataset is evaluated based on the DICE metric, which is compared to the starting point provided by the morphological operations. Hereafter, the mean DICE value for the entire dataset at each parameter step is calculated, of which the parameters are adjusted against.

Results - Parameter adjustment: The results of the parameter adjustment for the three active contour methods are summarized in tables 4.3 to 4.5. The associated figures representing the parameter tendencies as functions of the DICE values, are all found in appendix B, from where the maximum DICE values dictates the selected parameters.

Table 4.3 shows the two tests performed for the Local CV method. Reading the table, X indicates the parameter adjusted, which is further selected as the associated maximum DICE value. For Local CV, the smoothing term is selected to 0.08, and the side length of the localization object to 18 pixels. Equivalent to the Local CV, the Local MS parameters are found during similar tests, whereas the results are summarized in table 4.4: Here, the smoothing term is selected to 0.07, and the side length

Table 4.3: Local CV Parameter adjustment, where 'X' indicates the variable parameter, and bold represent final parameters.

	Constants			Variable			Results	
	Iterations	Side length	Smoothing term	Min	Max	Step Size	X	max Δ Dice
Test 1	40	17	X	0	0.15	0.01	0.08	0.01003
Test 2	40	X	0.08	0	20	1	18	0.01116

Table 4.4: Local MS Parameter adjustment, where 'X' indicates the variable parameter, and bold represent final parameters.

	Constants			Variable			Results	
	Iterations	Side length	Smoothing term	Min	Max	Step Size	X	max Δ Dice
Test 1	40	9	X	0	0.15	0.01	0.07	0.00572
Test 2	40	X	0.07	0	20	1	19	0.00972

of the localization object to 19 pixels. For Global CV, a single parameter is to be adjusted, namely the smoothing term, which is selected to 2000, as shown in table 4.5:

Table 4.5: Global CV Parameter adjustment, where 'X' indicates the variable parameter, and bold represent final parameters.

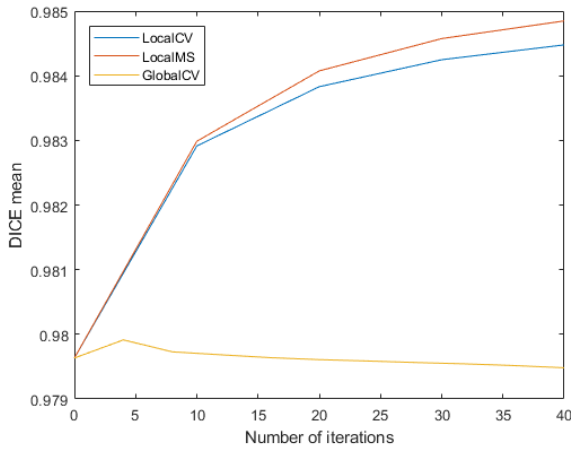
	Constants		Variable			Results	
	Iterations	Smoothing term	Min	Max	Step Size	X	max Δ Dice
Test 1	10	X	1	5000	1000	2000	0.00011

Experiment - Method comparison: In this experiment, the parameter adjusted methods are validated, in order to select the best performing active contour. To compare the three presented methods, the same experiment setup, as for the parameter adjustment, is used. However, now stepping the amount of iterations, to see how the methods perform over time. The number of iterations for each method is varied between 0 and 40. The two local methods are varied with 10 iterations per step, and the global method is varied with 4 iterations per step.

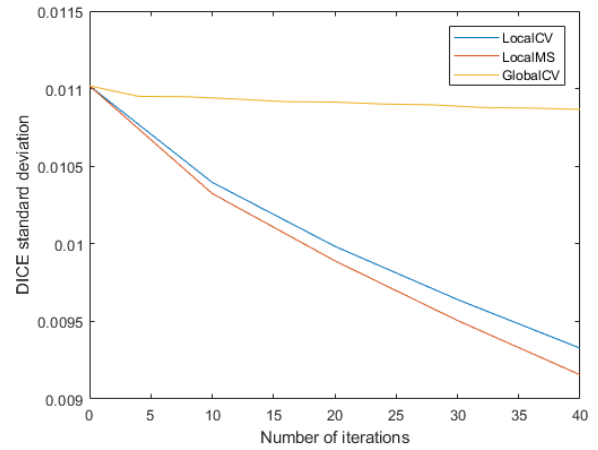
The mean DICE value for the entire dataset is calculated, in addition with the corresponding DICE standard deviation. The Hausdorff distance is additionally calculated for each image slice to validate the methods capabilities in cleaning up the erroneous masks produced by the morphological operations.

Results - Method comparison: By iterating the three methods, their respective DICE mean and standard deviations for each iteration steps is presented on figs. 4.6a and 4.6b. It is observed that the two local methods increases their DICE value in combination with the increase of iterations, whereas the Global CV method reaches an optimum at 4 iterations, whereafter its DICE value decreases. In addition, both local methods shares tendencies in regards of their DICE standard deviations, both decreasing with the increase of iterations. Here, the Global CV methods standard deviation is kept approximately constant. Next, the mean DICE values are compared to the absolute processing times, as presented on fig. 4.6e.

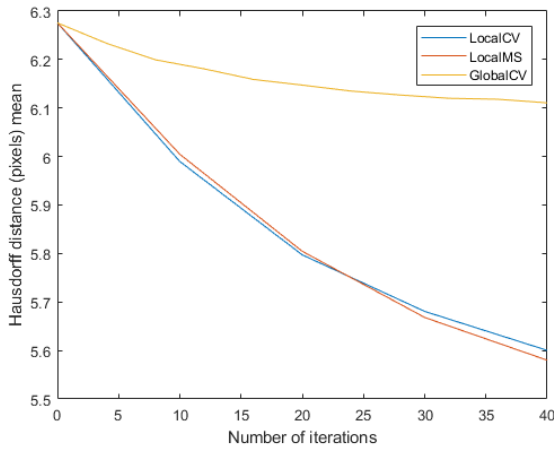
The Global CV method processing time per iteration for the entire dataset is approximately 31 seconds, where Local CV takes roughly 187 seconds, and Local MS 270 seconds. The decrease of mean DICE value seen in Global CV, removes it as a valid method, as the impact of the method is considered almost non existing. However, the two local methods have an increase in DICE mean value as a function of the processing time.



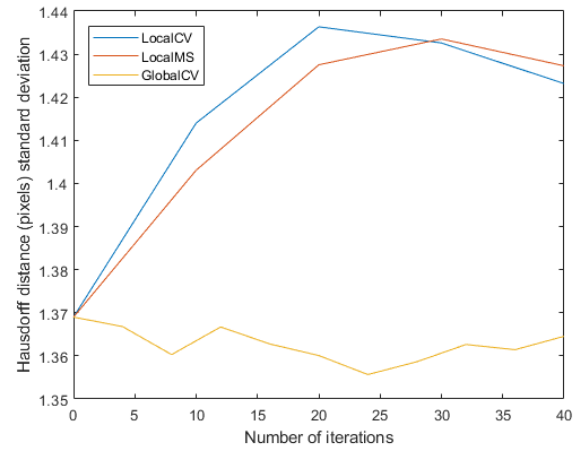
(a) DICE mean of the number of iterations.



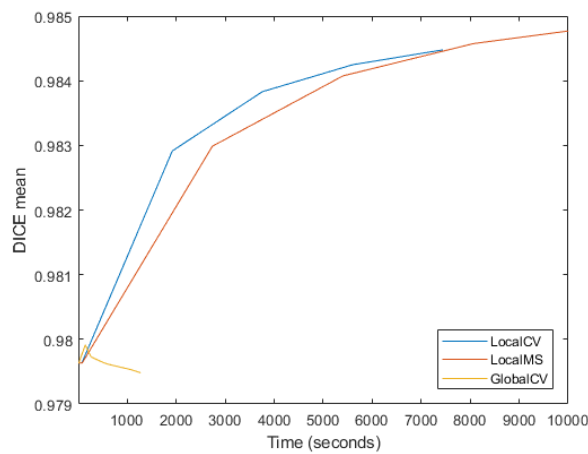
(b) DICE standard deviation of the number of iteration.



(c) Hausdorff distance mean of the number of iterations.



(d) Hausdorff distance standard deviation of the number of iterations.



(e) DICE mean value as function of processing time for each of the three active contour methods stepping from 0 to 40 iterations.

Figure 4.6: The DICE mean fig. 4.6a and standard deviation fig. 4.6b for each active contour method. Followed by the Hausdorff distance mean fig. 4.6c and standard deviation fig. 4.6d in pixels for each active contour method; Local CV, Local MS and Global CV as function of the number of iterations.

To compare the three methods in their ability to improve periosteal surface estimation, the Hausdorff distance is seen on figs. 4.6c and 4.6d.

Here, the same tendency, as seen for the DICE metric, is seen for the local methods, with an improvement of the Hausdorff distance as function of the amount of iterations computed. In addition, the Global CV method does also improve its Hausdorff distance, but with a lower rate per iterations.

Based on the DICE value and Hausdorff distances presented, an assessment of the most ideal amount of iterations is determined. For the Global CV method, the maximum DICE value is found at 4 iterations, whereas the value keeps increasing for the two local methods. To keep the processing time as low as possible, but still maximize the increase in DICE, the amount of iterations was selected to 20 for both local methods, as the slopes for both DICE and Hausdorff decreases significantly hereafter. This results in computational times of 10 minutes for the Global CV, 62 minutes for Local CV and lastly 90 min for the Local MS method.

To consider the methods at each slice for the image set, the absolute DICE value and Hausdorff distance for each image slice is found, using the above selected number of iterations. On fig. 4.7, the tendency of the proposed methods, in comparison to the initial mask for each image slice, is presented. As seen, the DICE value is subject to major changes at slices 50-90 and 150-190. This is due

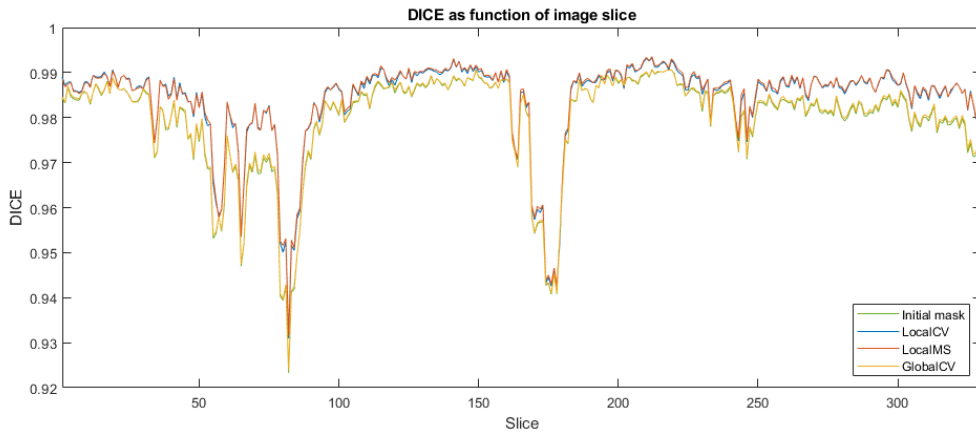


Figure 4.7: The DICE value per slice for each active contour method and the initial DICE value as a result from thresholding and morphological operations.

to the joint switches, where the ground truth manual labeling is very error prone due to noise, and therefore creates a bad validation basis. In addition, it is noted that the two local methods perform almost identical for each slice, whereas the difference between the global method and the initial mask is almost non existing.

Next, the Hausdorff distance for each slice is presented on fig. 4.8. Again, the metric shows spikes in the areas of slices 50-90 and 150-190, as a result of the joint change, which explains the high standard deviation presented on fig. 4.6d. Similar to the DICE value, the Hausdorff distance per slice is almost identical for the two local methods throughout the entire dataset.

Based on the presented results, the two local methods shows the most promising results. The major difference between the two methods are their computational complexity, with a difference around one minute per iteration when applied to the entire dataset of 330 images. As a result of this, Local CV was chosen as the active contour method for the final process, with the parameters presented on table 4.6.

The overall performance gain of the appliance of the Local CV to the proposed segmentation method is presented in table 4.7.

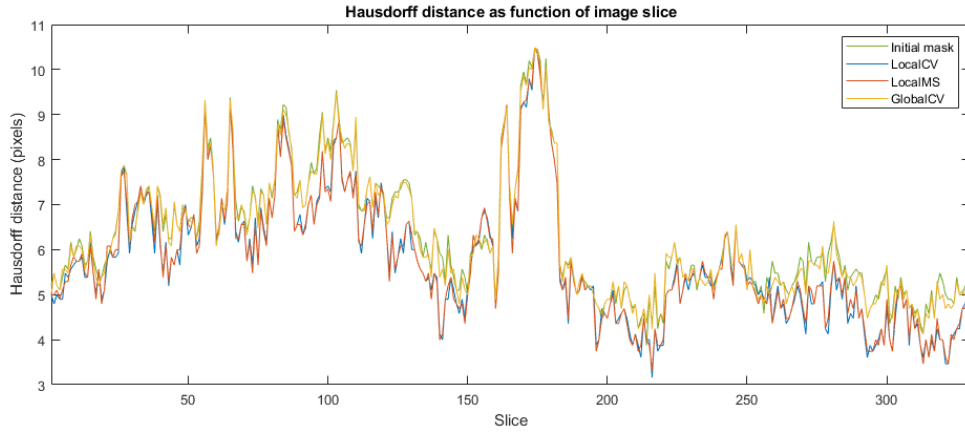


Figure 4.8: The Hausdorff distance per slice for each active contour method and the initial mask as a result of thresholding and morphological operations.

Table 4.6: The final parameters for the active contour method in the segmentation method

	Active contour method	Smoothing term	Side length	Iterations
Final Process	Local CV	0.08	18	20

Table 4.7: Mean and standard deviation for the the starting point provided by threshold and morphological operations

	<i>Threshold + MO</i>		<i>Local CV</i>		<i>Contribution</i>	
	Mean	Std	Mean	Std	Mean	Std
TPR	0.9936	$6.463 \cdot 10^{-3}$	0.9943	$6.657 \cdot 10^{-3}$	$7.419 \cdot 10^{-4}$	$1.936 \cdot 10^{-4}$
TNR	0.9952	$2.584 \cdot 10^{-3}$	0.9962	$2.583 \cdot 10^{-3}$	$9.929 \cdot 10^{-4}$	$-1.149 \cdot 10^{-6}$
FPR	$4.811 \cdot 10^{-3}$	$2.584 \cdot 10^{-3}$	$3.818 \cdot 10^{-3}$	$2.583 \cdot 10^{-3}$	$-9.929 \cdot 10^{-4}$	$-1.149 \cdot 10^{-6}$
FNR	$6.446 \cdot 10^{-3}$	$6.463 \cdot 10^{-3}$	$5.704 \cdot 10^{-3}$	$6.657 \cdot 10^{-3}$	$-7.419 \cdot 10^{-4}$	$1.936 \cdot 10^{-4}$
DICE	0.9796	0.0110	0.9838	$9.984 \cdot 10^{-3}$	$4.197 \cdot 10^{-3}$	$-1.034 \cdot 10^{-3}$
Hausdorff	6.2756	1.369	5.7971	1.4363	-0.4784	0.0673

The overall contribution as seen in the metrics is relatively small. To present the importance of the active contour method, visual image results of the active contour performance is seen in fig. 4.9.

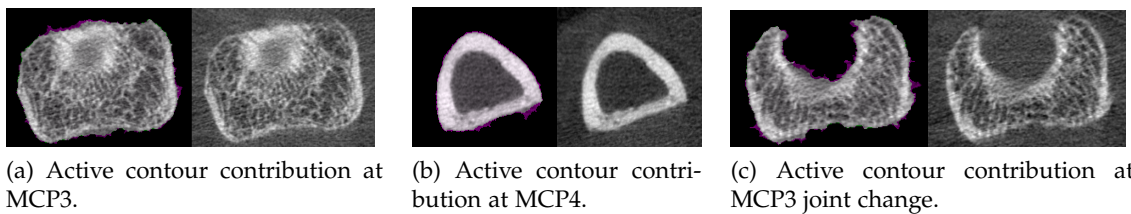
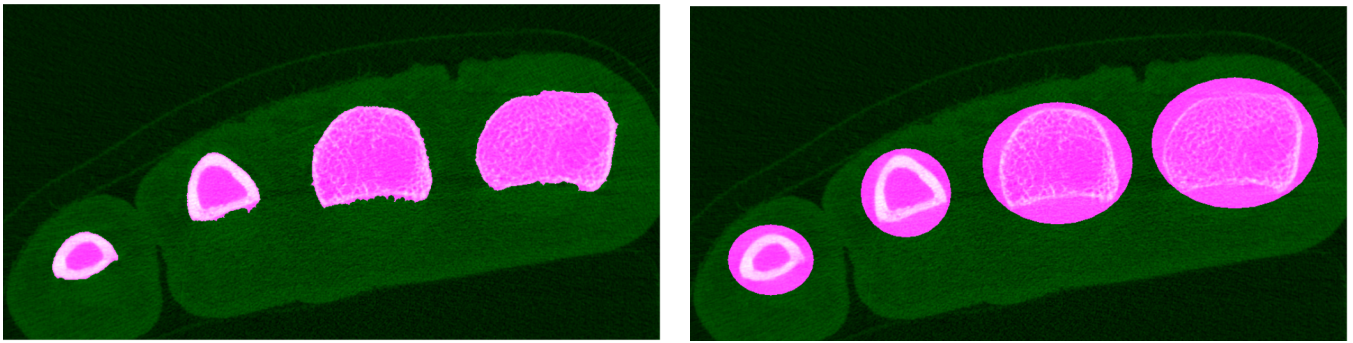


Figure 4.9: The contributions of the active contour illustrated on three examples. The segmented images are presented along with their original images. Purple and green colors on the images represent removed and added pixels respectively.

It is seen that the active contour removes undesired boundary objects, that is remaining from the previous segmentation steps. Based on these results, the addition of the method to the proposed hybrid segmentation method is deemed important.

Experiment - Initialization verification: The third experiment for the active contour, is intended to compare the initialization of the active contour performed by thresholding and morphological operations and manual initialization respectively. This is done to verify the importance of the initial segmentation step, and proving the ability of degrading the execution time for the overall segmentation.

The experiment was performed on a single image from a dataset. Two masks were created based on the image, one as a result of the thresholding and morphological operations and one manually created. The manual initialization was made by placing an ellipse around the joint, as shown on fig. 4.10b. The contour created by the thresholding and morphological operation is seen in fig. 4.10a. The selected Local CV active contour method was applied on both of the masks. The method was iterated, using both masks as initialization, until its maximum potential DICE value was reached.



(a) Mask resulting from thresholding and morphological operations.

(b) Mask resulting from manual placement.

Figure 4.10: Initial masks created from threshold and morphological operations in addition with manual ellipsis placement, shown on figs. 4.10a and 4.10b respectively.

To validate the need of the initialization through thresholding and morphological operations, the processing times of the two approaches are compared.

Results - Initialization verification: Seen in fig. 4.11, the result of the two mask approaches are plotted as function of iterations on fig. 4.11a and as function of execution time on fig. 4.11b.

From the two figures, it is seen that the initial masks create two completely different starting points, as the thresholding in addition with morphological operations are much closer to the desired contour than the manually placed. The thresholding approach reaches its maximum potential DICE value for the single image after 100 iterations, reaching the DICE value of 0.9909. The manual approach requires approximately 3000 iterations to reach its maximum DICE value at 0.9882. The thresholding approach takes approximately 70 seconds to reach its maximum, whereas the manual approach takes 35 minutes. In addition to the higher processing time, the manual approach never reaches the same DICE value as the thresholding approach. The manual placement would approximately take 193 hours, to segment an entire dataset of 330 images. These results thereby verifies the importance of the initial segmentation steps.

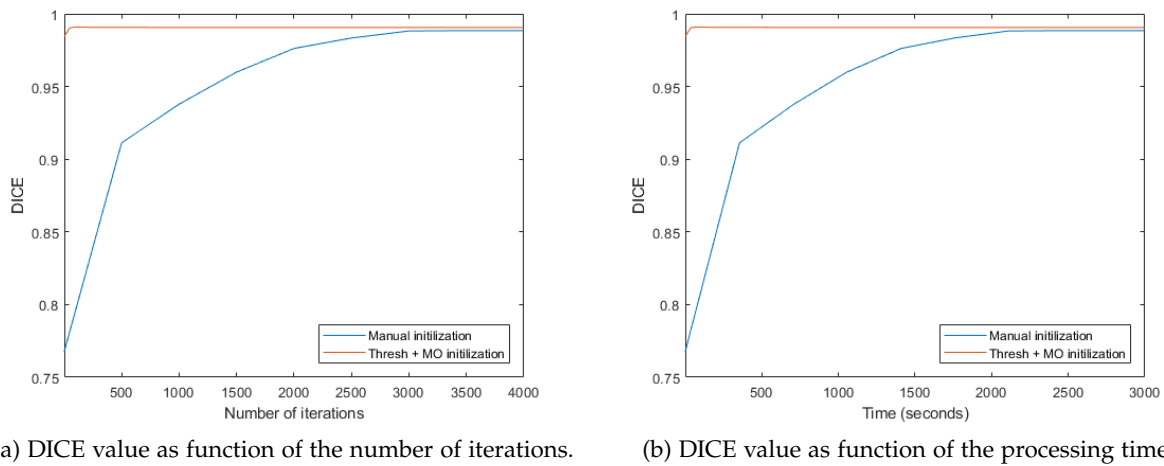


Figure 4.11: DICE value for both masks as functions of iterations seen on fig. 4.11a and execution time plotted on fig. 4.11b.

4.2.4 Visual Segmentation Results

Due to the limited amount of manually labeled segmentation data, it was decided to examine the segmented data visually, to evaluate the segmentation results. During this process, the segmented images were compared one-to-one, slice-by-slice, with the original datasets. The segmentations were rated as either correctly or incorrectly segmented. In addition, notes regarding artifacts, as presented in sections 3.1 and 3.4.1, were listed for the incorrectly segmented images. The reason for this, was to determine the factors for incorrect segmentation. A total amount of 104 datasets were segmented and visually scored, of which 88 was deemed correctly segmented and 16 incorrectly segmented, as presented in table 4.8.

Table 4.8: Correct and incorrect segmentations based on visual inspection of segmented datasets, compared to original datasets.

	Correct	Incorrect	Total
Absolute amount	88	16	104
Percentage	84.62%	15.38%	100%

Three types of artifacts were determined to be the underlying source of errors, being ring artifacts, patient motion and low-intensity borders. The distributions of the artifacts on the incorrect segmentations is seen in table 4.9. The distributions are taken as the number of incorrectly segmented images caused by the respective artifact. This implies that the same segmentation might have more than one artifact.

Table 4.9: Causation of incorrect segmentation, due to different noise artifacts.

	Ring Artifacts	Patient Motion	Low-intensity borders
Absolute amount	10	10	7
Percentage	62.5%	62.5%	43.75%

These results indicates that the overall segmentation method performance acceptable with 84.62% correctly segmented datasets. The remaining 15.38% incorrectly segmented datasets are a result of multiple types of artifacts, which can be directly linked to the image quality.

4.3 Registration Experiments and Results

According to section 3.5.6, eight different validation criteria are associated with registration. The most important criteria are the accuracy and precision. These criteria will be tested through specific experiments. The robustness and reliability of the registration are also validated through conducted experiments. The resource requirements of the registration is the binary images, provided by the segmentation. The algorithm complexity of the registration is validated by analyzing the overall processing time. The assumption verification lies in the assumption, that the binary images alone can be used for the registration. The clinical use of the registration is related to its further significance. Without the registration, different alignment problems may occur when detecting or quantifying erosions. Besides the use in the automatic erosion and quantification method, the registration is also desired in the clinical manual analysis of the dataset, since the visual representations of the joints are more natural.

Experiment - Accuracy, precision and robustness: The first experiment conducted for the registration process concerns the accuracy, precision and robustness. The test framework uses a moving and a fixed image. The moving image is applied with a random uniform rigid transformation using the integer ranges seen in table 4.10.

Table 4.10: Boundary values in rigid transformation for registration test framework.

	Min	Max
Rotation (Degrees)	-5	20
Translation X (Pixels)	-60	40
Translation Y (Pixels)	-45	40

The moving image is registered using the fixed image. After the registration the difference between the transformation, found by the registration, and the actual applied transformation are recorded. This process is carried out 1000 times with different random uniform rigid transformations. The mean and standard deviation for each transformation difference is calculated. The mean is seen as the accuracy of the registration and the standard deviation is seen as the precision. This process is carried out using two identical images, and two different images. The two different images are two consecutive image slices, implying that their contours only differs marginally. The difference in the image contours and in the rigid transformations validates the robustness of the registration.

Results - Accuracy, precision and robustness: The results of the experiment is seen in table 4.11. The rotation accuracy and precision for the identical and different images are similar, with the different images being slightly higher. For the accuracy and precision of the translation error, the identical and different images are also similar, here with the different images slightly better. The accuracy of the translation in both X and Y direction is below one pixel, which implies that the accuracy is close to optimal. The precisions are very close to 1, which indicates that the precisions are close to optimal as well. As the accuracy and precision for both test are very high and almost identical, the robustness of the registration is therefore also verified. The maximum values in the translation is around 6 to 7 pixels, which is still a high reduction compared to the translation transformation boundaries applied. The processing time of the registration has a maximum of approximately 12 seconds. As a dataset only needs two registration processes, the combined registration would, for a global registration, take approximately 24 seconds. In this scenario it is not considered computationally complex when compared to the segmentation method.

Table 4.11: Registration accuracy and precision.

	<i>Identical images</i>			<i>Different images</i>		
	Mean	Std	Max	Mean	Std	Max
Rotation (Degrees)	0.0014	0.0151	0.3751	0.0055	0.0206	0.7828
Translation X (Pixels)	0.3383	1.0184	6.8987	0.2885	0.9271	7.0931
Translation Y (Pixels)	0.3710	1.0587	7.2365	0.3673	0.9173	7.0837
Time (Seconds)	9.3063	1.7136	12.3001	7.9013	1.2488	12.4716

Experiment - Global reliability: This experiment tests the reliability of a global rigid registration applied to the images. The setup for this experiment is that single dataset is registered between image slice 110 and 111 and again between 220 and 221. The differences in the transformation applied by the registration are recorded, and the mean and standard deviation are calculated, based on 200 executions. Besides the transformation error, the DICE values and the Hausdorff distances are also calculated, to prove the improvement of the registration.

Results - Global reliability: The results of the 200 executions are seen in table 4.12. The results of both the mean DICE value and mean Hausdorff distance are improved through the registration, meaning the resulting image joints have improved their alignments. The standard deviations for the DICE values and Hausdorff distances are insignificant. This implies that each registration execution is performed equally. Likewise, the rotation, x translation and y translation have insignificant standard deviations. The global registration is therefore highly reliable. The visually improvements of the global registration is seen in fig. 4.12.

Table 4.12: Registration accuracy and precision for global joint registration. These results are based on 200 executions.

	<i>Image 110-111</i>		<i>Image 220-221</i>	
	Mean	Std	Mean	Std
DICE before	0.9381	0	0.9059	0
DICE after	0.9522	1.79e-15	0.9451	1.66e-15
Hausdorff distance before (Pixels)	9.8994	0	8.9443	0
Hausdorff distance after (Pixels)	9.5916	1.30e-14	7.0711	3.65e-14
Rotation (Degrees)	-9.61e-14	0	-9.61e-14	0
Translation X (Pixels)	5.9800	9.57e-15	-8.5000	2.84e-14
Translation Y (Pixels)	-1.9224	1.31e-15	-0.6354	1.55e-15
Time (Seconds)	6.4410	0.3562	5.9845	0.4086

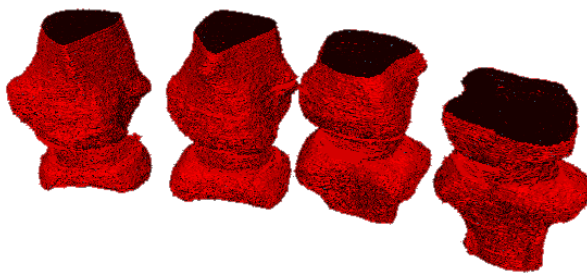
Experiment - Local reliability: Besides the global registration, a local registration is also validated for its performance and reliability. The experiment itself is identical to the global experiment, but in this experiment each joint is extracted and registered to its corresponding joint in the other image slice. Thereby different transformations are applied to each joint. Doing this might result in a better registration, as patient motion, causing the registration problem, may result in multiple different transformations for each joint. The DICE values and Hausdorff distances for the registration are recorded, along with the transformation parameters applied for each joint.

Results - Local reliability: The results for the local registration reliability experiment for 200 executions are seen in table 4.13. Both the mean DICE value and mean Hausdorff distance is improved through the registration, implying that a better alignment is achieved. For both the translations and the rotations for each joint, the standard deviations are approximately zero, meaning that the local

Table 4.13: Registration accuracy and precision from local registration of different images

	<i>Image 110-111</i>		<i>Image 220-221</i>	
	Mean	Std	Mean	Std
DICE before	0.9381	0	0.9059	0
DICE after	0.9648	2.07e-16	0.9652	1.78e-15
Hausdorff distance before (Pixels)	9.8994	0	8.9443	0
Hausdorff distance after (Pixels)	9.0553	5.92e-15	6.4807	4.45e-15
Rotation Joint 1 (Degrees)	1.73e-12	0	7.78e-14	0
Rotation Joint 2 (Degrees)	-5.86e-14	0	0.9836	0
Rotation Joint 3 (Degrees)	8.77e-15	0	2.4932	3.56e-15
Rotation Joint 4 (Degrees)	2.54e-14	0	0.5049	6.67e-16
Translation X Joint 1 (Pixels)	-0.8067	5.42e-16	-5.2432	2.13e-14
Translation X Joint 2 (Pixels)	5.1684	4.92e-15	-7.3744	1.15e-14
Translation X Joint 3 (Pixels)	78.609	8.13e-14	-7.3495	2.40e-14
Translation X Joint 4 (Pixels)	14.6060	7.84e-15	-6.7874	1.42e-14
Translation Y Joint 1 (Pixels)	0.2636	2.09e-17	-5.8219	2.13e-14
Translation Y Joint 2 (Pixels)	-3.2894	1.36e-15	0.4068	3.89e-16
Translation Y Joint 3 (Pixels)	-134.59	8.69e-14	10.712	4.27e-14
Translation Y Joint 4 (Pixels)	-17.058	0	1.6921	6.45e-15
Time (Seconds)	32.124	1.0133	41.773	1.9387

registration is highly reliable. The improvement seen in the mean DICE value and mean Hausdorff distance are higher than for the global approach, which indicates that a local registration approach is desirable. This does, however, come at the expense of a higher processing time as a dataset needs 8 instead of 2 registrations. This results in an approximately overall registration time of 40 seconds. This is, however, still not computationally complex when compared to the segmentation process. A 3D and 2D representation of the local registered dataset is seen in fig. 4.13.



(a) The 3D structure of the dataset after global registration is applied.



(b) 2D representation of the alignment of image slice 110 and 111 after the application of the global registration. Purple and green pixels represent differences between the two slices.

Figure 4.12: 3D and 2D representations of the dataset after application of the global registration method. The dataset is more aligned when compared to the initial non-registered dataset seen in fig. 3.19.

Based on the presented results, the local registration is selected for the final proposed erosion and detection method.

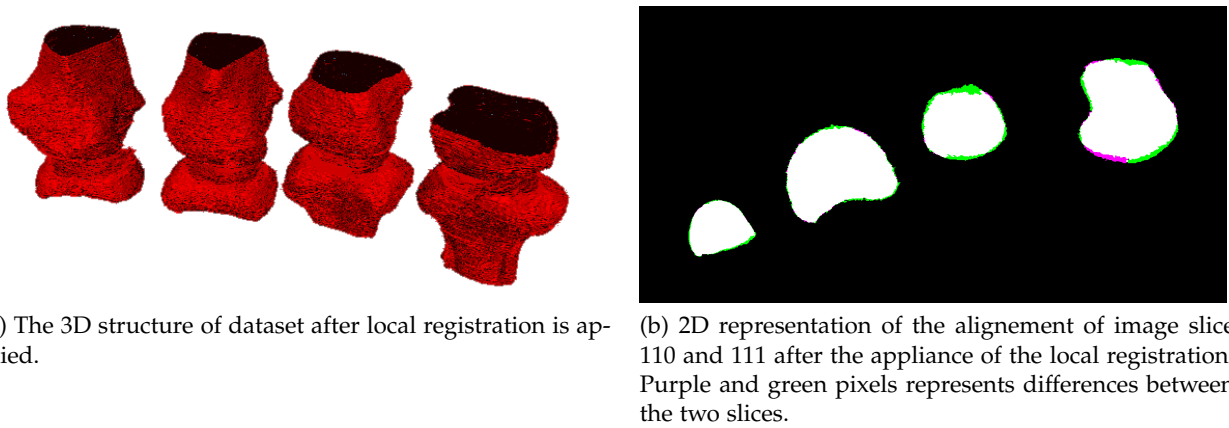


Figure 4.13: 3D and 2D representations of the dataset after appliance of the local registration method. The dataset is more aligned when compared to the initial non registered dataset seen in fig. 3.19.

4.4 Erosion Detection and Quantification Experiments and Results

The last set of experiments and results, are the ones associated with the proposed erosion detection and quantification method. The method is tested for its capabilities in detection and quantification individually, using the metrics presented in section 3.6.2. For each experiment, the method is tested against the golden reference provided through visual detection by domain personal.

4.4.1 Detection experiments and results

The first three experiments of the final part of the proposed method is related to the detection of erosions.

Experiment - Detection: For the validation of the detection capabilities of the proposed method, each available manual detected dataset were tested during the experiment. For each dataset the preprocessing, segmentation and registration methods were applied prior to the proposed erosion detection method. By appliance of the detection method on the datasets, the amount of correctly detected erosions were calculated as the TP measurement. To accept an erosion as detected, a centroid of an erosion originating from the given golden reference data was required to be located within the detected erosion volume. The amount of incorrect detected erosions, FN, were calculated along with the amount of incorrectly rejected erosions, FP. Based on these values, the sensitivity and precision of the proposed method was calculated, as specified in section 3.6.2. A total amount of 88 datasets were used to validate the detection method.

Results - Detection: The results of the detection capabilities of the proposed detection method, is presented in table 4.14: It is seen of the results that 28, of the total 48 manually detected erosions, were

Table 4.14: The TP, FN and FP measurements of the detection experiment in absolute numbers. In addition with TPR and PPV in percentage.

	TP	FN	FP	TPR (Sensitivity)	PPV (Precision)
Erosions	28	20	396	58.33%	6.6%

detected by the proposed method. Based on this, a sensitivity of 58.33% is obtained.

Moreover, a total amount of 396 FP detections were made, which results in a low precision of 6.6%. This result was, however, expected due to three reasons. First, the amount of noisy artifacts located in the processed datasets causes various scenarios of falsely created cavities. During the detection, these cavities might meet the SPECTRA criteria, and are therefore detected as erosions. Especially datasets consisting of a high amount of patient motion will result in a large amount of erosion detections. As no overall quality assessment of the datasets was available, low quality image dataset might exist in the processed datasets. Secondly, not all erosions in the datasets were registered in the golden reference, meaning actual erosions found by the method was detected as FP. Thirdly, especially sclerosis erosions, which was typically registered as one erosion in the golden reference, might be detected as multiple erosions by the method.

To visually show the capabilities of the proposed detection method, different detection sceneries are presented. A correctly detected large active erosion, located radial on the 2nd MCP, is seen on fig. 4.14a. The erosion is considered perfectly measured when compared to the trabecular structure, as well as the reconstruction of the periosteal surface.

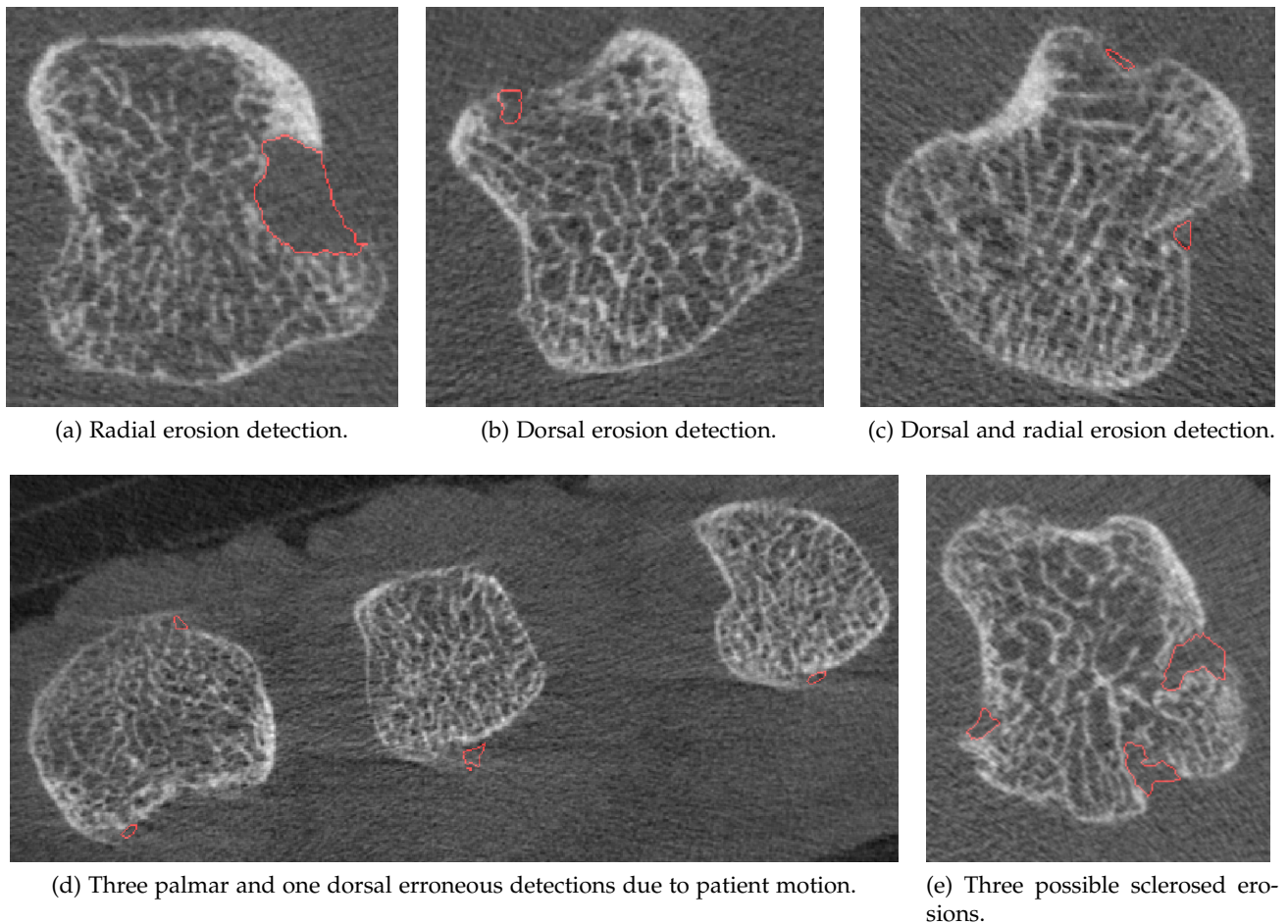


Figure 4.14: Possible erosion detections.

Figure 4.14b shows an example of an erosion which is detected by the method, but not registered in the manual golden reference. This possible erosion is detected as it meets all five SPECTRA criteria. Next, two erosions are detected on fig. 4.14c. These possible erosions are likewise not registered in the golden reference, but meets the SPECTRA criteria.

Next, fig. 4.14d shows a case of erroneous detections due to patient motion in the image data. The errors are due to the high pixel intensities in the created blurring as a result of patient motion, which are segmented as a part of the periosteal surface. Such an error is considered impossible to avoid with the current proposed method, and indicates the importance of better image acquisition.

The last example is presented on fig. 4.14e, showing three sclerosed erosions all located in the 2nd MCP.

Experiment - Visual detection error validation: Based on the results generated for the detection method, each of the false erosion rejections was visually evaluated, to find the reason for their rejection by the method.

Results - Visual detection error validation: Each of the FN erosions were evaluated and the reason for the false rejection was registered and categorized. The reason categories and the amount of erosions associated, are listed in table 4.15.

Table 4.15: Categories of false rejected erosions.

Cause	Amount
Erosion not complaint with list 3.3	9
Erosion located in joint shift	6
Erosion periosteal break to small for method	3
Erosion undetected due to registration	1
Erosion undetected due to patient motion	1

Overall, five different reasons for the false erosion rejection were found. The highest amount of erosions fell under the category of erosions not complying with the criteria specified by SPECTRA as seen in list 3.3. This was especially items 1 and 3 in list 3.3, which the erosion did not comply with. As the method was design after the criteria, these erosions were not detected. These visually assumptions was created by the authors, and may therefore be incorrect. The second category was erosions placed in a joint shift. The proposed method removes the joint shift before the detection, meaning eventually erosions in this area are undetected. The third category is erosion with extremely small openings. These openings have been closed in the morphological operation step of the proposed hybrid segmentation method, and not opened by the active contour segmentation method. The fourth category was erosions not detected because of registration problems, not fully aligned by the proposed registration method. The last category was erosions not detected because of patient motion interfering with the erosion area. The patient motion created false cortical structure in the area, which caused the method to close the area.

By removing the erosions not complying with the SPECTRA criteria in list 3.3, from the FN number, a more valid sensitivity can be calculated.

Table 4.16: TP, FN and sensitivity after removing erosions not complying with the SPECTRA criteria in list 3.3.

	TP	FN	TPR (Sensitivity)
Erosions	28	11	71.79%

The sensitivity of the detected erosions complying with the SPECTRA criteria in list 3.3, is seen in table 4.16. It is seen that there is an improvement of 13.46% in the sensitivity when compared with sensitivity seen in table 4.14.

4.4.2 Quantification experiments and results

The last experiment conducted for the erosion detection and quantification method, is related to the quantification of the erosions.

Experiment - Quantification: Based upon the resulting TP erosions acquired doing the detection experiment, a comparison to the corresponding golden reference quantification data is produced. These quantifications consist of the erosion centroid, volume, width and depth. These metrics are validated using the quantification validation methods presented in section 3.6.2.

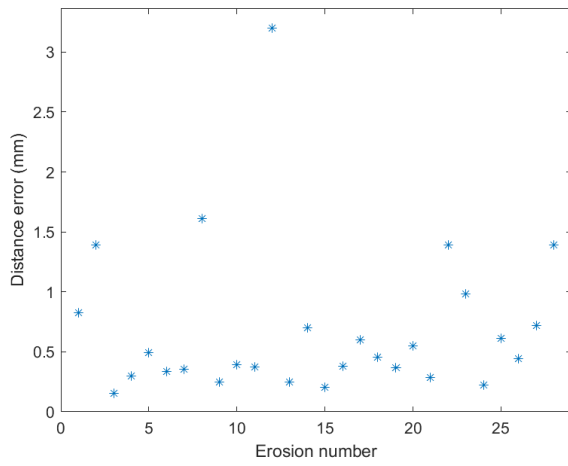
Results - Quantification reliability: The results for the centroid quantification are seen in fig. 4.15a. The distance is plotted along the y-axis and the erosion number is plotted along the x-axis. The distances are calculated in mm by multiplying the pixel distance with the voxel size of $0.082mm$. It is seen that non of the predicted centroids are exactly matching, and that all are relative small distance errors. The majority of the distances have an error between $0 - 1mm$, which is tolerable. Some outliers are seen, and may be caused by incorrect filling of the erosion or incorrect golden reference.

For the width, depth and volume, the error ratio in percentage are calculated between the predicted value and the golden reference. A positive percentage means that the predicted value is smaller than the golden reference, and a negative value means that the predicted value is higher than the golden reference. The ratios are then plotted as functions of the golden reference values, and is seen in figs. 4.15b to 4.15d. Common for both width, depth and volume is that the majority of the predictions are smaller than the golden reference. The reason for this, is that the method has a tendency to make the erosions smaller than the golden reference, as the predicted erosions are calculated in 3D. Some large outliers exist in both width, depth and volume. One reason for these outliers is that the basis for calculation is different between the predicted values and the golden reference. The width and the depth might be calculated in different slices, which is bound to create different results. The method for the volume calculation in the golden reference is unknown, but it is a calculated prediction based on the width and depth, and differences between predicted values and golden references are therefore highly plausible. Another reason for the outliers is that errors are found in the golden reference. The mean accuracy and precision for the quantification results are seen in table 4.17.

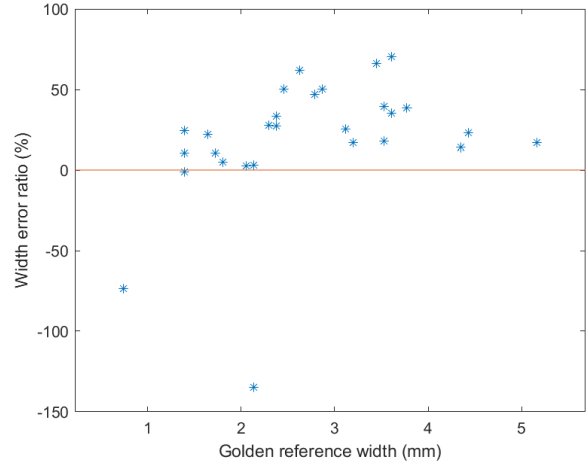
Table 4.17: Results gathered from the quantification experiment, showing the AE, AER, PE and PER for each of the quantification parameters; centroid, width, depth and volume.

	AE	AER	PE	PER
Centroid	0.6869mm	N/A	0.9295mm	N/A
Width	0.6760mm	18.98%	1.1818mm	44.14%
Depth	0.5137mm	23.17%	1.4018mm	45.49%
Volume	4.6288mm ³	23.90%	15.36mm ³	77.74%

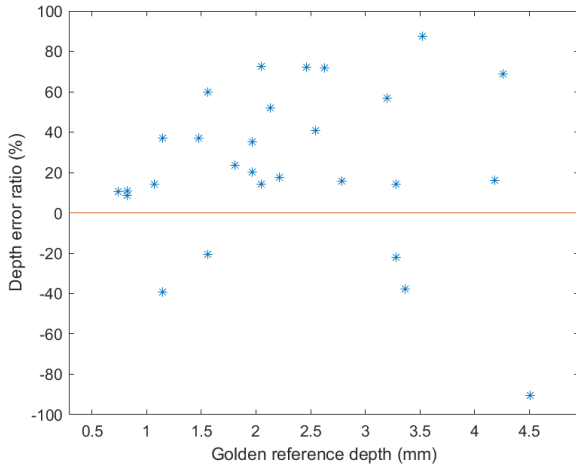
For the centroid the AE is 0.6869mm with a PE of 0.9295mm. For the width, depth and volume the AER is approximately 23%, indicating that the golden reference is generally measured higher than the prediction of the method. The PER for the width and depth is around 45%, which indicates a high variation in the prediction compared with the golden reference. This is primarily caused by large outliers in the results. The PER of the volume is 77.74%, which is considerably high, and also caused by outliers in the results. Overall, the quantification method is neither very accurate nor very precise, when compared with the golden reference. The PER would be improved if outliers are corrected, and the accuracy would therefore be a systematic error.



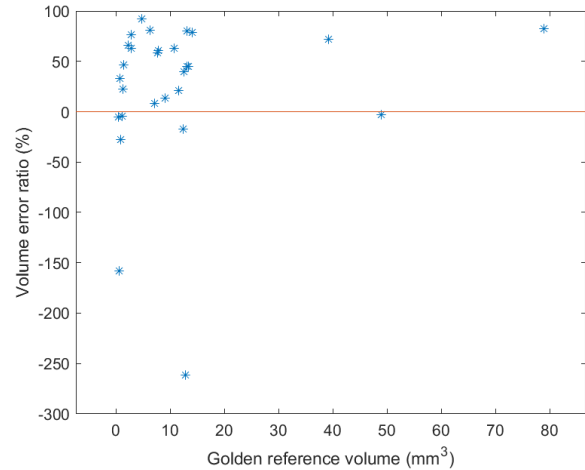
(a) The absolute distance between the predicted center coordinates and the golden reference.



(b) The width error ratio in percent for each of the detected erosions.



(c) The depth error ratio in percent for each of the detected erosions.



(d) The volume error ratio in percent for each of the detected erosions.

Figure 4.15: The errors calculated between the predicted quantification results and the golden references.

4.5 Profiling Experiment and Results

To analyze the share of computational time throughout the presented methods, a profiling experiment was conducted. Optimization of the presented method is not considered part of the scope of the study. The experiment is therefore merely conducted to assess where optimization would be beneficial.

Experiment - Profiling: The profiling experiment was done by execution of the entire proposed method on a dataset. The computational time and amount of function calls for each nested function was measured. Using MATLAB's profiling tool [89], a profile report was extracted containing the desired measurements. These measurements were then analyzed to enable an assessment of beneficial optimization steps.

Results - Profiling: The summary of the resulting profiling of the five overall steps of the proposed method is seen in table 4.18. It is seen that the segmentation and the erosion detection methods are

Table 4.18: Result of profiling experiment, containing the computational times in seconds and share of the total computational time in percentage. The overall computational time of the entire execution was 5819 seconds.

	Computational time (s)	Share (%)
Preprocessing	25	0.4
Segmentation	4662	80.1
Registration	80	1.4
Erosion Detection	1010	17.4
Erosion Quantification	3	0.05
Total	5780	99.35

the two most time consuming elements in the process. As the segmentation method takes 80.1% of the total computational time, it was further analyzed as presented in table 4.19. Due to the appliance of

Table 4.19: Profiling result of the hybrid segmentation method.

	Computational time (s)	Share (%)
Thresholding	2	0.04
Morphological Operations	69	1.48
Active Contour	4588	98.41
Total	4659	99.93

the active contour in the 2D plane, the method is called 330 times, once for each slice of the dataset. As the results of each of these calls are independent of each other, parallelization either by GPU or CPU would drastically reduce the overall computational time. To investigate the individual computational times, the individually times for the active contour methods nested functions are found. The amount of calls along with the computational times for the nested functions are presented in table 4.20. The

Table 4.20: Results of profiling for the active contour method. The top five consuming operations are shown, which share a total of 92.5% of the active contour. The operations are shown with references to their equations presented in section 3.4.5.

	Calls (#)	Computational time (s)	Share (%)
eq. (3.56)	6600	1494	32.6
eq. (3.51)	6600	827	18
eq. (3.53)	6600	736	16.1
eq. (3.54)	6600	729	15.9
eq. (3.57)	6600	455	9.9
Total	33000	4241	92.5

6600 calls of each equation implementation is a result of the 330 total active contour calls, multiplied with the selected 20 iterations for each image slice. The high computational time caused by the amount of calls, could be reduced utilizing parallelization.

Chapter 5

Discussion

The aim of this study, was to develop an algorithm for automating the process of detection and quantification of erosions related to RA in HR-pQCT images. The proposed method is based on the concept of isolating the cortical border through a hybrid segmentation method, whereafter cortical breaks, as a result of RA, are identified using different image manipulation techniques and assumptions. The underlying reason for this approach, lies in the assumption that the cortical breaks, as a result of RA, are distinguishable from the cortical border of the bone joints. In addition, similar promising work in the field of automatic erosion detection and quantification also exploits this approach [5, 4]. Because of the limited research in automatic erosion detection and quantification, the proposed approach has been limited to existing promising work. Other approaches to the problem has not been considered. Overall, the proposed method consists of four distinguishable steps being; preprocessing of the initial data, an automatic segmentation of the periosteal surface, registration of joints and an erosion detection and quantification method.

The purpose of the proposed hybrid segmentation method, is to create a fully closed segmentation of the periosteal surface, where cortical breaks are represented as irregular notches in the surface. The proposed hybrid segmentation method consists of three steps; thresholding, morphological operations and active contour. The reason for the use of a hybrid method is, that no independent segmentation method could fulfill the needed requirements. The steps of the proposed segmentation method are inspired by the hybrid method proposed in [61], which is used in the semiautomatic erosion quantification method proposed by [4].

The initial step of the proposed hybrid segmentation method is thresholding. The aim of the thresholding is to create of binary image, including as much cortical border information as conceivable. As this process is based directly upon the voxel intensities of the images, the introduction of noisy elements are highly likable and should be avoided. Four different thresholding methods were studied and tested, including the self-made Gaussian characteristic, Entropy, Otsu's clustering and Niblocks adaptive method. These methods were selected, as they represent common techniques and cover different categories of thresholding approaches. However, the selected methods represent a limited area of available thresholding techniques, implying that an outperforming technique might be available for the novel HR-pQCT images.

A larger study of thresholding methods for HR-pQCT images might reveal a better method than the Gaussian characteristic method selected for the final segmentation of the proposed method. Further inclusion of image enhancement techniques as preprocessing steps, might improve the thresholding methods performance. This could be achieved through the introduction of filtering or edge enhancement techniques improving the image quality. This has, however, not been a focus point in

this study. The results created in association with the thresholding methods are highly depended on the preceding morphological operations.

The purpose of the morphological operation step, in the proposed hybrid segmentation method, is to close the initial contour created by the thresholding. The result of the morphological operations is therefore highly dependable on the amount of contour and noise, included by the thresholding. Especially the placement of the thresholded cortical structure is important for the morphological operations, as the close operation only closes objects near to each other. If cortical objects are not near each other, the morphological operations will not be able to close the border and a cortical break will be present and misinterpreted as an erosion. However, if the morphological operations use a large closing, cortical breaks, actually representing erosions, will be closed. The development of a better thresholding method will therefore lead to a better morphological operation performance.

The third and final step of the proposed hybrid segmentation method is active contour. The purpose of this step is to refine the border of the desired contour. This was considered a need, as the morphological operations applied after thresholding, consistently added undesired information during the contour closing. Three overall active contour methods were analyzed, a global and two local ones. Through the presented experiments, it was shown that the local approaches outperformed the global, which implies, that the contour evolution was drastically affected by the heterogeneous statistical model, shared by the bone and hand tissue regions. By isolating the evolution to only consider local properties, both distance- and volume-based metrics were improved.

Furthermore, the importance of the thresholding and morphological operations were proven, as an optimum initialization of the contour was utmost important. The initialization dictates not only the final possible correctness of the segmented contour, but also the amount of iterations needed. To reduce the overall processing time of the segmentation, the best trade-off between contribution of the method and amount of iterations were found. However, increasing the number of iterations results in a further increase in the border refinement at the cost of processing time. Therefore, depending on the final implementation of the method, the amount of iterations can be increased if computational time allows it.

The overall performance of the hybrid segmentation method greatly depends on the image quality of the HR-pQCT datasets. As multiple challenges are introduced in relation to the image quality, such as low-intensity edges and various noise artifacts, the reliability of the proposed hybrid segmentation method is drastically degraded, as a result of low image quality. However, the quality of the future HR-pQCT images is expected to increase, as actions, such as better fixtures reducing patient motion, is introduced. In addition, personal training as well as correct scan calibration is also expected to increase the image consistency and quality. Finally, the proposed segmentation method is adjusted and trained against a single manual segmented dataset. This greatly reduces the amount of features present. Because of this, the reliability and robustness of the proposed hybrid segmentation method are reduced. However, through visually inspection of the resulting segmented datasets, it was shown that the proposed hybrid segmentation method satisfyingly segmented 84.62% of all datasets.

The registration method proposed, has the responsibility of aligning otherwise misaligned image slices. The registration process aligns the image slices 110-111 and 220-221, as these slices proposes possible misalignments. The proposed method uses the binary images, created by the segmentation process, to align each joint independently. The registration is therefore highly dependent on the performance of the segmentation process, as an incorrect segmentation will lead to an incorrect registration. Another limitation associated with the proposed registration method, is in the case of misalignment in

joint shifts, resulting in an erroneous alignment. The results created for the registration process, shows that the registration possesses a high accuracy and precision, with an error of approximately 1 pixel. The reliability and robustness of the registration is also adequate. The results, however, are merely based on a single dataset. This entails that the results do not represent the entire data collection, as other possible misalignment scenarios could exist. A more optimum registration process might be accomplished using a 3D registration process instead of the proposed 2D process, as obtainable 3D information could lead to more satisfactory results. The 2D registration is only performed in the axial plane, resulting in possible misalignment in coronal and sagittal planes, as these are left unattended. The reason for the registration problem is caused by patient motion during image acquisition. Improving the image acquisition using a better fixture, as discussed earlier, might therefore reduce the registration problem and possibly eliminate it.

The proposed detection method is highly depending on the resulting dataset produced by the segmentation and registration. Undersegmentation generally results in an increase of false positive detections, as unclosed cavities might meet the erosion criteria listed in list 3.3. Oversegmentation might yield false negatives, due to erroneous closing of true erosion regions. In addition, incorrect transformations during the registration, could introduce a large shift between image slices, which might contribute to either false positive cavities or, remove supportive information contributing to a true positive erosion.

The developed detection method is designed to fulfill the SPECTRA criteria presented in list 3.3, utilizing a definition of the trabecular bone thickness presented by [5]. Item 4 in list 3.3 defines that loss of the trabecular bone shall be present for an cortical break to count as an erosion. However, no clear definition of the amount of trabecular loss is specified. Therefore, an assumption is made, introducing a threshold parameter for the minimum trabecular loss of an erosion. This parameter is variable, and is in this study set to favor a high sensitivity over a high precision for the finished method. This decision was based on the desire to increase the capability to detect early erosions. Based on the detection methods appliance on 88 datasets containing 48 manually detected erosions, the method possesses a sensitivity of 71.79%. However, this sensitivity is based on corrections in the provided golden reference, as some erosions were deemed to not fulfill the SPECTRA criteria in list 3.3. The sensitivity for the proposed method is comparable to the sensitivity of 69.7 – 76.3% by the detection method proposed by Peters et al. [5]. Additionally, during the tests, the precision was determined to 6.6%. A low precision was expected due to the reasons explained in section 4.4.1. Overall, the increase in detections were expected, especially considering the trabecular loss threshold.

The final quantification method was based upon the SPECTRA guidelines presented in list 3.4. This decision was made to match the golden reference, and because no clear standard guideline is made for 3D erosion quantification. Four properties are found for the erosions, namely their volume, centroid, width and depth.

The volume, which was determined as the total amount of voxels in the detected erosion, had an AER of 23.90% and a PER of 77.74% compared to the golden reference. These results indicate a large variation in the quantification produced by the method. However, the golden reference volume calculations might be erroneous, as they are merely calculated assumptions of volumes. For the depth and width the AER was approximately 19 – 23% with a PER of 45%, which is also considered a relatively high variation. These variations are a result of the methods, which are not fully compliant to the golden reference. The impact of the varying results for the quantification method, might be acceptable, as the final method shall give an estimate of RA progression. This means that, the quantification metrics shall be used to verify changes in the erosions between scans, and the variation from the golden reference might therefore be insignificant, as long as the changes in the erosions can be recorded.

5.1 Further Research

A subject which has not been covered in depth during this study, is the possibilities within preprocessing. Filtering and edge enhancement methods applied to the HR-pQCT images, might produce a better basis for the segmentation method. However, a trade-off shall be considered, as image enhancement methods might remove important information in the images. A large erroneous factor in the segmentation method is low image quality, as a result of image artifacts. A better image quality assessment of the images could provide a more statistical representation of erosion detection possibilities. An automatic image quality assessment method for HR-pQCT images was proposed in [44], and might contribute to the overall methods capabilities.

During the parameter adjustment and method selection of the hybrid segmentation method, the training data available was limited to a single dataset. Therefore, by introducing more abundant training data, the robustness and performance of the proposed method is expected to increase. Additionally, the training data was conducted by operators with a limited amount of domain knowledge. One large limitation in this approach was that operator variability is not considered. Ideally, this process should be conducted by several experienced specialists or radiologists, followed by a comparison, to account for operator variations.

The final proposed detection method was selected to priorities a high sensitivity over a high precision. This trade-off can be adjusted through a minimum trabecular bone loss threshold for possible erosions. This specific amount of bone loss is not specified in the SPECTRA erosion criteria listed in section 3.6. Other erosion indicators could be considered in the erosion determination process e.g. shape and position. Introducing an erosion classifier to the detection method, might lead to a better erosion determination, as a more statistically representative selection is achieved.

As the guidelines for erosion quantification is limited to 2D properties, the introduction of a 3D erosion representation might reveal concealed information. The erosion width is defined by SPECTRA as the maximum cortical break width in the axial plane. However, by using the 3D information, a more representative width of the erosion might be achieved. The same principles applies for the depth calculation. The introduction of such new properties might provide a more accurate quantification of erosions, thereby, providing more information to the RA diagnosis and prognosis.

The proposed method is capable of detecting and quantifying erosions. However, this is merely a single of plural RA disease indicators. Therefore, extension of the proposed method with other automatic RA indicator methods, might provide more reliable diagnostic and prognosis of RA. Promising indicator methods are the BMD calculation method proposed by Yang et al. [27], and the JSW calculation method proposed by Barnabe et al. [45].

Chapter 6

Conclusion

A method applicable for erosion detection and quantification in HR-pQCT images, from patients affected by the chronic disease RA, is proposed in this study. The final method is capable of both detection and quantification of erosions.

The method is composed of several individual components, including a preprocessing step, initializing the patient data, a hybrid segmentation method, able to segment the periosteal surface of finger joint, a registration method, realigning joints affected by patient motion, a method that can detect erosions, and finally a method quantifying detected erosion.

Each of the individual methods in the proposed method is tested and adjusted using manual labeled data, consisting of both segmented images and quantified erosions.

The proposed hybrid segmentation method shows a correct segmentation rate of 84.62% for HR-pQCT datasets, based on adjustment using only a single manual labeled dataset. The erosion detection method was able to detect 71.79% of correct erosions, which were only 6.6% of the total amount of possible erosions found. The quantification of the correct erosions had an accuracy error ratio of approximately 23% with a varying precision error ratio of 45 – 77%.

The results from all of the presented methods have two common related limitations. The first being image quality, which shows to have a large impact on all methods. If the image quality of the HR-pQCT images are low, image artifacts have a large disruption on almost all methods. Further research in the area of HR-pQCT image quality and acquisition, would significantly improve the results of the proposed method. The second limitation is due to the reference data used to validate the methods, which was both insufficient and contained errors. Using abundant and accurate referencing data would improve the methods capabilities.

The proposed method allows for further development and extension. Other automatic RA indicator methods e.g. BMD and JSW, could be included in the proposed method, thereby further strengthening the RA diagnostic and prognosis abilities.

Overall, the proposed method shows promising results in its erosion detection and quantification capabilities. However, the proposed method should, in its current state, only aid domain personal in their diagnostic and prognosis of RA patients.

6.1 Perspectivation

The overall motivation behind this study, was to validate the use of HR-pQCT imaging for improving RA disease evaluation. Additionally, it was considered whether the introduction of an automatic algorithm for erosion detection and quantification was capable of both increasing patient prognosis reliability, as well as reducing financial expenses related to the personal involvement needed in todays manual detection.

The results of the introduced algorithm, might increase the capabilities for early erosion detection. This increase contributes to the general patient prognosis, as erosions are considered an early diagnosis indicator [3]. As described in chapter 2, other RA disease indicators obtainable through HR-pQCT imagery exists. The combination of the proposed erosion detection and quantification method with such other indicators, are also considered to plausibly increase the RA prognosis. In addition, by enabling the possibility to create 3D erosion representations, better quantification is considered possible, as earlier 2D quantification guidelines might result in misleading results. A 3D erosion representation could introduce new unseen erosion analysis potential, thereby possible contributing to the RA disease understanding.

The proposed method is, at its current state, seen as an assisting technology, and not yet a replacement for manual detection. For this to be reality, further refinement is needed for the erosion detection and quantification method, in addition with a more stable and reliable data acquisition process. However, as an assisting tool, the proposed method might reduce the time intensity of the manual erosion detection and quantification process currently applied in practices. This could greatly reduce both the prognosis estimation time and associated financial expenses. Moreover, the proposed method might also produce more reliable quantifications of erosions, as the process is identical for each erosion. Lastly, the proposed method might produce otherwise unseen erosions, by the HVS, which could have a large impact on the diagnostic and prognosis of RA patients.

6.2 Contributions

The main contributions of the presented study are:

- A hybrid segmentation method for periosteal surface of MCP in HR-pQCT images.
- A registration method for HR-pQCT MCP finger joints.
- An automatic erosion detection method.
- An automatic erosion quantification method.

The news value is considered high for the proposed segmentation method, as it presents a new hybrid combination of methods for the purpose of periosteal MCP joint segmentation. In addition, when comparing to other existing methods for the given purpose [5, 4], the presented solution is considered as fully automatic. The detection method is considered a new approach, by utilizing SPECTRA criteria [13] as arguments for the image manipulations and morphological operations performed during erosion detection. Lastly, the quantification method, also by meeting SPECTRA guidelines, presents a new approach in erosion quantification, as earlier methods did not meet these guidelines. Moreover, current research does not present a method both capable of detection and quantification of erosions.

The overall significance of the presented solution and the four main contributions is also noteworthy. By the introduction of a fully automatic method, personal involvement could be discarded, thereby reducing financial expenses. However, the method requires a certain level of image quality to function without personal evaluation of the segmented images. The registration method not only serves the purpose of contributing to the proposed method, but also contributes to todays manual detection by the removal of image misalignment. The introduction of 3D erosion quantification also introduces new possibilities in the analysis of RA. Finally, the introduction of a method both capable of detecting and quantifying erosions is significant.

Future work should include a larger training set for the proposed segmentation method, to increase its reliability against noise and artifacts. Additionally, the final solution should be tested with more patients, to fully represent it as an independent solution.

6.3 Personal Contributions

Prior to the presented study, the authors had a very limited knowledge of the area of medical image processing, which meant that the learning curve within the domain was very steep at the initial phase of the study. Due to the lack of domain knowledge, a vast research of medical image processing was necessary, in order to determine useful methods valid for the study. A large amount of different methods, including various combinations, have therefore been tested in order to determine the methods actually used. The learning outcome of this process has been considered tremendous.

The most challenging area within the study, was the development of a dynamic, robust, reliable and automatic segmentation method, determining the foundation for the actual detection and quantification method. A lot of different segmentation methods were studied, and the final proposed method ended up being a hybrid of three significant different methods, implying that these areas also had to be mastered. As the study is located in the area of biomedical engineering, a vast amount of medical terms, methods and expressions was unfamiliar, and had to be studied.

In order to validate and quantify the image segmentation performance correctly, segmented golden reference images was required. As no golden reference labeling for the concerning data was available, the authors had to manually label this golden reference. This proved extremely time consuming, resulting in only one segmented golden reference dataset. From this challenge, the authors have realized the importance of allocating time for data preparation, as well as the advantages by outsourcing such a task.

In addition, to create a truly dynamic solution, capable of correctly detect erosions, without the introduction of various self claimed assumptions, proved time consuming. As all methods and results were created using MATLAB, the authors gained a lot of experience, especially within image manipulation and medical image processing. Overall, the knowledge and experience gained through this study has been immense.

Appendix A

Manual Labeling

The following tables summarize the features represented in the manual labeled training dataset, which is used for parameter adjustment and method selection. The tables present ring artifacts, patient motion, low-contrast edges, joint changes, erosions and lastly, cysts respectively. Each feature is presented through a figure, in addition with a description of the location of the feature through the MCP count, axial slice number and location in relation to the MCP head.

Ring Artifacts

The most noteworthy ring artifacts present in the manual labeled dataset are captured in table A.1:

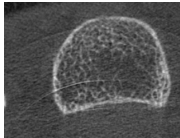
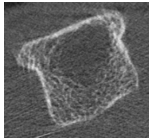
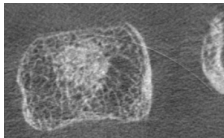
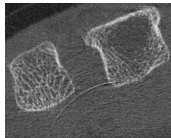
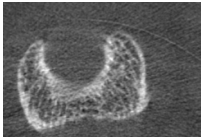
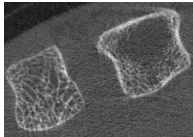
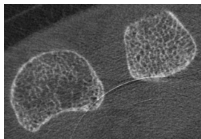
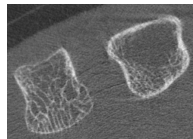
MCP	Slice	Quadrant	Figure	MCP	Slice	Quadrant	Figure
3	10	Ulnar		3	227	Palmar	
3	51	Radial		3-4	230	Palmar	
3	70	Dorsal		3-4	239	Ulnar	
3-4	120	Palmar		3-4	249	Ulnar	

Table A.1: Ring Artifacts in the manual labeled dataset

Patient Motion

Cases of patient motion in the manual labeled dataset are shown in table A.2:

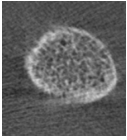
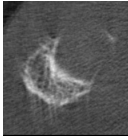
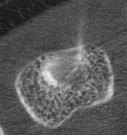
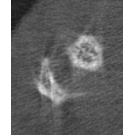
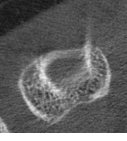
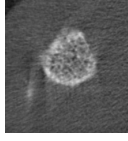
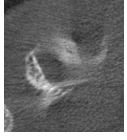
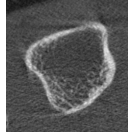
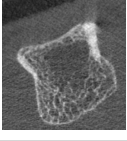
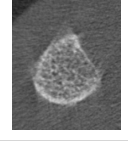
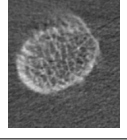
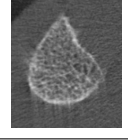
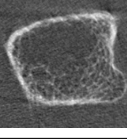
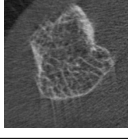
MCP	Slice	Quadrant	Figure	MCP	Slice	Quadrant	Figure
2	74	Palmar		5	237	Palmar	
4	160	Dorsal		5	245	All	
4	164	Dorsal		5	252	Palmar	
4	175	Palmar		3	254	Dorsal	
3	189	Dorsal		5	262	All	
4	193	Dorsal		5	274	Palmar	
2	225	Radial		5	305	All	

Table A.2: Patient motion in the manual labeled dataset

Low-contrast Edges

Low-contrast edges in the manual labeled dataset are shown in table A.3.

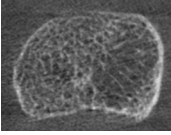
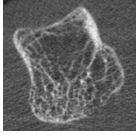
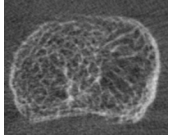
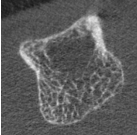
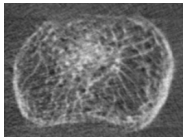
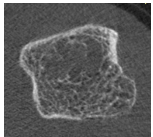
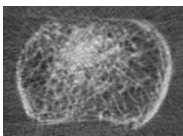
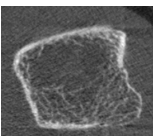
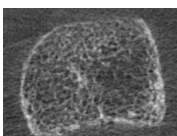
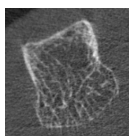
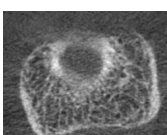
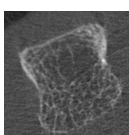
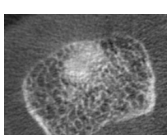
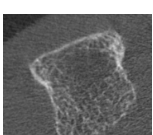
MCP	Slice	Quadrant	Figure	MCP	Slice	Quadrant	Figure
2	8	Dorsal		3	168	Palmar	
2	14	Dorsal		3	186	Palmar	
2	22	Dorsal		2	192	Palmar	
2	27	Dorsal		2	207	Palmar	
3	35	Dorsal		4	263	Palmar	
3	65	Dorsal		4	279	Palmar	
4	155	Dorsal		4	288	Palmar	

Table A.3: Low-contrast edges in the manual labeled dataset

Joint Change

Joint changes in the manual labeled dataset are seen in table A.4.

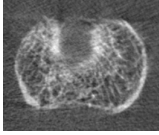
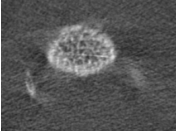
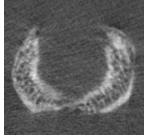
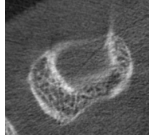
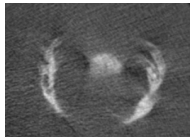
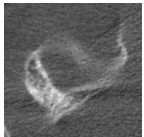
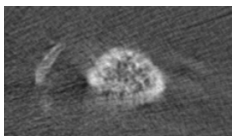
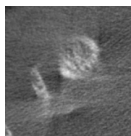
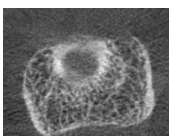
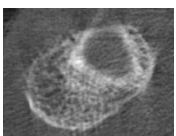
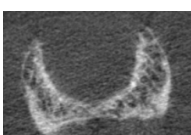
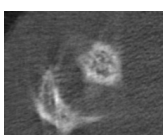
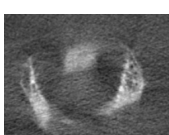
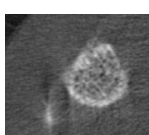
MCP	Slice	Quadrant	Figure	MCP	Slice	Quadrant	Figure
2	35	All		3	89	All	
2	47	All		4	166	All	
2	56	All		4	173	All	
2	62	All		4	179	All	
3	64	All		5	229	All	
3	77	All		5	244	All	
3	82	All		5	251	All	

Table A.4: Joint changes in the manual labeled dataset

Erosion and cyst

The manual labeled dataset contains both a case of erosion shown on table A.5 and a cyst which is presented on table A.6:

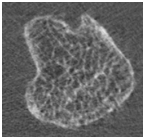
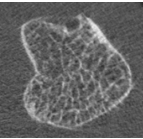
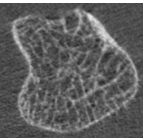
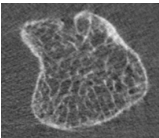
MCP	Slice	Quadrant	Figure
2	126	Dorsal	
2	132	Dorsal	
2	138	Dorsal	
2	144	Dorsal	

Table A.5: Erosion in the manual labeled dataset

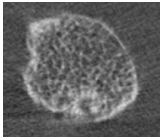
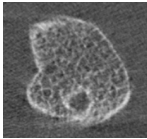
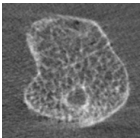
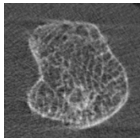
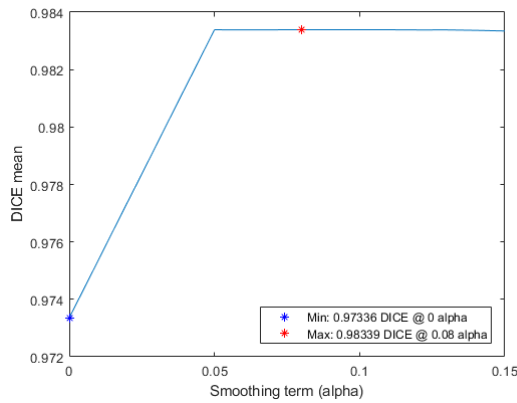
MCP	Slice	Quadrant	Figure
2	84	Palmar	
2	94	Palmar	
2	104	Palmar	
2	110	Palmar	

Table A.6: Cyst in the manual labeled dataset

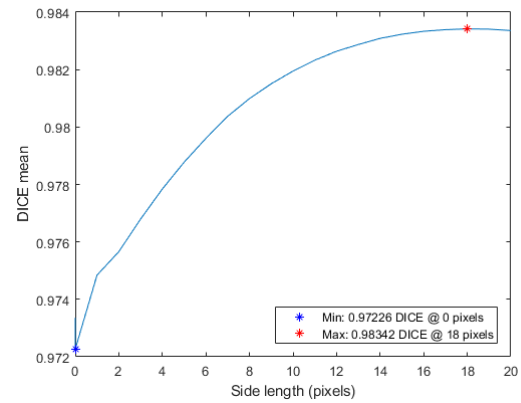
Appendix B

Active Contour Results

During the parameter adjustment of the active contour, a set of graphs were produced from where the parameters were selected. This appendix presents these figures for the two localized methods; Local CV fig. B.1 and Local MS fig. B.2, respectively.

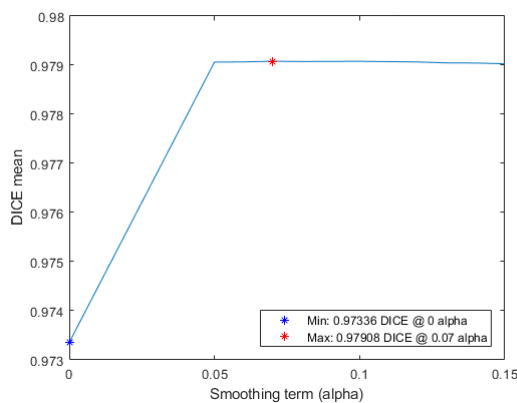


(a) DICE mean as function of smoothing term

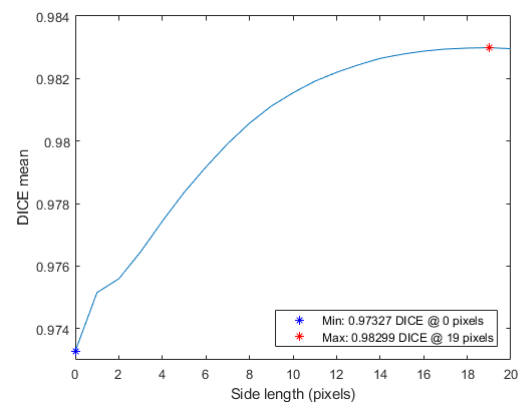


(b) DICE mean as function of side length

Figure B.1: Local CV parameter adjustment results.



(a) DICE mean as function of smoothing term



(b) DICE mean as function of side length

Figure B.2: Local MS parameter adjustment results.

Abbreviations

Abbreviation	Full Form	Meaning
AE(R)	Accuracy error (ratio)	Validation metric for accuracy estimation.
BMD	Bone mineral density	Measurement used as RA indicator.
CR	Conventional 2D radiography	Medical imaging modality.
CT	Computed tomography	Medical imaging modality.
CV	Chan-Vese	Active contour method technique.
DICE	Søren-Dice index	Statistics used for comparing two samples similarity.
DICOM	Digital Imaging and Communications in Medicine	Medical imaging storing standard.
FN	False negative (ratio)	Derivations from a confusion matrix.
FP	False positive (ratio)	Derivations from a confusion matrix.
HR-pQCT	High Resolution peripheral Quantitative Computed Tomography	Medical imaging modality.
HVS	Human visual system	Human beings visual system.
MS	Mean separation	Active Contour method technique.
JSW	Joint space width	Measurement used as RA indicator.
MRI	Magnetic resonance imaging	Medical imaging modality.
PE(R)	Precision error (ratio)	Validation metric for precision estimation.
RA	Rheumatoid arthritis	Autoimmune joint disease.
ROC	Receiver operating characteristic	Representation of TPR as function of FPR.
ROI	Region of interest	Areas within images or samples of specific interest.
SNR	Signal-to-noise ratio	Measure for comparison between level of desired signal to noise.
SPECTRA	Study group for xtrEme Computed Tomography in Rheumatoid Arthritis	RA study group.
TN(R)	True negative (ratio)	Derivations from a confusion matrix.
TP(R)	True positive (ratio)	Derivations from a confusion matrix.
VOI	Volume of interest	Volume of specific interest, within a given dataset.
μ CT	Micro computed tomography	Medical imaging modality.

Medical terms

Medical term	Meaning
Autoimmune disease	Disease occurring from responses of the immune system against its own healthy cells and tissues.
Cortical bone	The harder outer layer of the human bones. Often referred to as the compact dense part of the bone.
Distal	Term used to define body parts distant to the main human body. It is the counterpart of proximal, used to describe parts close to the main body.
In vitro	Used for studies on microorganisms, cells or biological molecules outside their normal biological context. Opposite to in vivo.
In vivo	"Within the living", used for studies on living organisms. Opposite to in vitro.
Metacarpophalangeal joint	Also known as MCP. Joint between the metacarpal bones and the proximal phalanges.
Osteoporosis	A rheumatology disease, resulting in risk of bone breakage due to weakening of the bones.
Pathological	Used to describe when a change to the human body is altered or caused by disease.
Periosteal surface	The outer membrane of bone surfaces.
Phalanges	The bones which are located in the human fingers as well as toes. Are divided into proximal, intermediate and distal. Proximal being closest to the Metacarpals.
Modality	Medical image acquisition technique.
Radius	Also known as radial bone, one of the two large bones of the human forearm.
Tibia	Also known as the shinbone, the largest of the two bones located in the human leg below the knee.
Trabecular bone	Also known as the cancellous bone. It is the internal tissue of the skeletal bone, and often referred to as the spongy part of the bone.
Coronal, Sagittal and Axial plane	Coronal plane divides the human body into left and right. Sagittal plane divides the human body into front and back. Axial plane divides the human body into bottom and top.
Radial, Ulnar, Palmar and Dorsal	Medical terms defining the orientations in hands. Radial is towards the thumb, Ulnar is away from the thumb, Palmar is towards the palm and Dorsal is away from the palm.

Bibliography

- [1] Josef S. Smolen, Daniel Aletaha, and Iain B. McInnes. "Rheumatoid arthritis". In: *The Lancet* 388 (2016), pp. 2023–2038. ISSN: 1474547X. DOI: 10.1016/S0140-6736(16)30173-8. URL: [http://dx.doi.org/10.1016/S0140-6736\(16\)30173-8](http://dx.doi.org/10.1016/S0140-6736(16)30173-8).
- [2] Rasmus K. Jensen. "Project description - Early diagnosis of joint destruction in rheumatoid arthritis". 2016.
- [3] Christian M. Stach, Michael Bäuerle, Matthias Englbrecht, Gerhard Kronke, Klaus Engelke, Bernhard Manger, and Georg Schett. "Periarticular Bone Structure in Rheumatoid Arthritis Patients and Healthy Individuals Assessed by High-Resolution Computed Tomography". In: *Arthritis and Rheumatism* 62.2 (2010), pp. 330–339. ISSN: 00043591. DOI: 10.1002/art.27252. URL: <https://www.ncbi.nlm.nih.gov/pubmed/20112404>.
- [4] Dominique Töpfer, Stephanie Finzel, Oleg Museyko, Georg Schett, and Klaus Engelke. "Segmentation and quantification of bone erosions in high-resolution peripheral quantitative computed tomography datasets of the metacarpophalangeal joints of patients with rheumatoid arthritis". In: *Rheumatology* 53.1 (2014), pp. 65–71. ISSN: 14620324. DOI: 10.1093/rheumatology/ket259. URL: <https://academic.oup.com/rheumatology/article/53/1/65/1780954>.
- [5] M. Peters, A. Scharmga, J. De Jong, A. Van Tubergen, P. Geusens, J. J. Arts, D. Loeffen, R. Weijers, B. Van Rietbergen, and J. Van Den Bergh. "An automated algorithm for the detection of cortical interruptions on high resolution peripheral quantitative computed tomography images of finger joints". In: *PLoS ONE* 12.4 (2017), pp. 1–15. ISSN: 19326203. DOI: 10.1371/journal.pone.0175829. URL: <http://journals.plos.org/plosone/article?id=10.1371/journal.pone.0175829>.
- [6] Vikas Majithia and Stephen A. Geraci. "Rheumatoid Arthritis: Diagnosis and Management". In: *American Journal of Medicine* 120.11 (2007), pp. 936–939. ISSN: 00029343. DOI: 10.1016/j.amjmed.2007.04.005. URL: [https://linkinghub.elsevier.com/retrieve/pii/S0002-9343\(07\)00361-0](https://linkinghub.elsevier.com/retrieve/pii/S0002-9343(07)00361-0).
- [7] Georg Schett and Ellen Gravallese. "Bone erosion in rheumatoid arthritis: mechanisms, diagnosis and treatment". In: *Nat Rev Rheumatol* 19.1 (2012), pp. 656–664. ISSN: 09694900. DOI: 10.1038/nrrheum.2012.153. URL: <https://www.ncbi.nlm.nih.gov/pmc/articles/PMC4096779/>.
- [8] King Christian X's Rheumatism Hospital. *Research projects — DanACT study*. <http://www.gigthospitalet.dk/forskning/forskningsprojekter/2014-danact-studiet/>. [Online; accessed 19-May-2018].
- [9] Kresten Krarup Keller. "QTE studiet Højopløselig perifer kvantitativ computertomografi - Ny og sensitiv billeddiagnostisk metode til måling af behandlingseffekt og prognose for patienter med tidlig reumatoid artrit". Aarhus.

- [10] Andrew J. Burghardt, Thomas M. Link, and Sharmila Majumdar. "High-resolution Computed Tomography for Clinical Imaging of Bone Microarchitecture". In: *Clinical Orthopaedics and Related Research* 469.8 (2011), pp. 2179–2193. ISSN: 0009921X. DOI: 10.1007/s11999-010-1766-x. URL: <https://www.ncbi.nlm.nih.gov/pmc/articles/PMC3126972/>.
- [11] Andrew J. Burghardt, Galateia J. Kazakia, Sweta Ramachandran, Thomas M. Link, and Sharmila Majumdar. "Age- and Gender-Related Differences in the Geometric Properties and Biomechanical Significance of Intracortical Porosity in the Distal Radius and Tibia". In: *Journal of bone and mineral research* 25.5 (2010), pp. 983–933. ISSN: 1523-4681. DOI: 10.1359/jbmr.091104. URL: <http://doi.wiley.com/10.1359/jbmr.091104><http://www.ncbi.nlm.nih.gov/pubmed/19888900><http://www.pubmedcentral.nih.gov/articlerender.fcgi?artid=PMC3153365>.
- [12] Jiri Jan. *Medical Image Processing, Reconstruction and Restoration*. Vol. 25. Signal Processing and Communications. CRC Press, 2005, p. 710. ISBN: 978-0-8247-5849-3. DOI: 10.1201/9781420030679. URL: <https://www.taylorfrancis.com/books/9781420030679>.
- [13] Cheryl Barnabe, Dominique Toepfer, Hubert Marotte, Ellen Margrethe Hauge, Andrea Scharmga, Roland Kocijan, Sebastian Kraus, Stephanie Boutroy, Georg Schett, Kresten Krarup Keller, Joost De Jong, Kathryn S. Stok, and Stephanie Finzel. "Definition for rheumatoid arthritis erosions imaged with high resolution peripheral quantitative computed tomography and inter-reader reliability for detection and measurement". In: *Journal of Rheumatology* 43.10 (2016), pp. 1935–1940. ISSN: 14992752. DOI: 10.3899/jrheum.160648. URL: <http://www.jrheum.org/content/43/10/1935>.
- [14] Waraporn Srikhum, Warapat Virayavanich, Andrew J. Burghardt, Andrew Yu, Thomas M. Link, John B. Imboden, and Xiaojuan Li. "Quantitative and Semiquantitative Bone Erosion Assessment on High-resolution Peripheral Quantitative Computed Tomography in Rheumatoid Arthritis". In: *Journal of Rheumatology* 40.4 (2013), pp. 408–416. ISSN: 0315162X. DOI: 10.3899/jrheum.120780. URL: <http://www.jrheum.org/content/40/4/408.short>.
- [15] Scanco Medical. *XtremeCT — Systems & Solution Scanco Medical*. <http://www.scanco.ch/en/systems-solutions/clinical-microct/xtremect.html>. [Online; accessed 05-April-2018].
- [16] 4C Medical. *XtremeCT HR-pQCT scanner by Scanco Medical AG*. http://www.4cmedikal.com.tr/uploads/kapak/1503054692-xtremect2_.jpg. 2017 (accessed March 22, 2018).
- [17] A. Scharmga, M. Peters, A. Van Tubergen, J. Van Den Bergh, J. De Jong, D. Loeffen, B. Van Rietbergen, R. Weijers, and P. Geusens. "Visual detection of cortical breaks in hand joints: Reliability and validity of high-resolution peripheral quantitative CT compared to microCT". In: *BMC Musculoskeletal Disorders* 17.1 (2016), pp. 1–7. ISSN: 14712474. DOI: 10.1186/s12891-016-1148-y. URL: <http://dx.doi.org/10.1186/s12891-016-1148-y>.
- [18] Anne Fouque-Aubert, Stéphanie Boutroy, Hubert Marotte, Nicolas Vilayphiou, Justine Bacchetta, Pierre Miossec, Pierre Dominique Delmas, and Roland D. Chapurlat. "Assessment of hand bone loss in rheumatoid arthritis by high-resolution peripheral quantitative CT". In: *Annals of the Rheumatic Diseases* 69.9 (2010), pp. 1671–1676. ISSN: 00034967. DOI: 10.1136/ard.2009.114512. URL: <http://ard.bmj.com/content/69/9/1671.info>.
- [19] Yinghe Huo, Koen L. Vincken, Désirée Van Der Heijde, Maria J.H. De Hair, Floris P. Lafeber, and Max A. Viergever. "Automatic Quantification of Radiographic Finger Joint SpaceWidth of PatientsWith Early Rheumatoid Arthritis". In: *IEEE Transactions on Biomedical Engineering* 63.10 (2016), pp. 2177–2186. ISSN: 15582531. DOI: 10.1109/TBME.2015.2512941. URL: <https://ieeexplore.ieee.org/document/7368104/>.

- [20] D L Scott, C Smith, and G Kingsley. "Joint damage and disability in rheumatoid arthritis: an updated systematic review." In: *Clinical and experimental rheumatology* 21.5 Suppl 31 (2003), pp. 20–27. ISSN: 0392-856X. URL: <http://www.clinexprheumatol.org/article.asp?a=2185>.
- [21] Y. Aurell, MLE Andersson, and K. Forslind. "Cone-beam computed tomography, a new low-dose three-dimensional imaging technique for assessment of bone erosions in rheumatoid arthritis: reliability assessment and comparison with conventional radiography – a BARFOT study". In: *Scandinavian Journal of Rheumatology* 47.3 (2018), pp. 173–177. ISSN: 15027732. DOI: 10.1080/03009742.2017.1381988. URL: <https://doi.org/10.1080/03009742.2017.1381988>.
- [22] Paul Bird, Marissa Lassere, Ron Shnier, and John Edmonds. "Computerized Measurement of Magnetic Resonance Imaging Erosion Volumes in Patients with Rheumatoid Arthritis: A Comparison With Existing Magnetic Resonance Imaging Scoring Systems and Standard Clinical Outcome Measures". In: *Arthritis and Rheumatism* 48.3 (2003), pp. 614–624. ISSN: 00043591. DOI: 10.1002/art.10820. URL: <https://onlinelibrary.wiley.com/doi/abs/10.1002/art.10820>.
- [23] Angela R. Crowley, Jing Dong, Alex McHaffie, Andrew W. Clarke, Quentin Reeves, Megan Williams, Elizabeth Robinson, Nicola Dalbeth, and Fiona M. McQueen. "Measuring Bone Erosion and Edema in Rheumatoid Arthritis: A Comparison of Manual Segmentation and RAMRIS Methods". In: *Journal of Magnetic Resonance Imaging* 33.2 (2011), pp. 364–371. ISSN: 10531807. DOI: 10.1002/jmri.22425. URL: <http://dx.doi.org/10.1002/jmri.22425>.
- [24] P. D. Emond, D. Inglis, A. Choi, J. Tricta, J. D. Adachi, and C. L. Gordon. "Volume Measurement of Bone Erosions in Magnetic Resonance Images of Patients with Rheumatoid Arthritis". In: *Magnetic Resonance in Medicine* 67.3 (2012), pp. 814–823. ISSN: 07403194. DOI: 10.1002/mrm.23037. URL: <http://dx.doi.org/10.1002/mrm.23037>.
- [25] Uffe Møller Døhn, Bo J. Ejbjerg, Michel Court-Payen, Maria Hasselquist, Eva Narvestad, Marcin Szkudlarek, Jakob M. Møller, Henrik S. Thomsen, and Mikkel Østergaard. "Are bone erosions detected by magnetic resonance imaging and ultrasonography true erosions? A comparison with computed tomography in rheumatoid arthritis metacarpophalangeal joints". In: *Arthritis Research and Therapy* 8.4 (2006), pp. 1–9. ISSN: 14786354. DOI: 10.1186/ar1995. URL: <https://arthritis-research.biomedcentral.com/articles/10.1186/ar1995>.
- [26] J. Duryea, M. Magalnick, S. Alli, L. Yao, M. Wilson, and R. Goldbach-Mansky. "Semiautomated three-dimensional segmentation software to quantify carpal bone volume changes on wrist CT scans for arthritis assessment". In: *Medical Physics* 35.6 (2008), pp. 2321–2330. ISSN: 00942405. DOI: 10.1118/1.2900111. URL: <https://aapm.onlinelibrary.wiley.com/doi/abs/10.1118/1.2900111>.
- [27] Haitao Yang, Andrew Yu, Andrew J. Burghardt, Warapat Virayavanich, Thomas M. Link, John B. Imboden, and Xiaojuan Li. "Quantitative characterization of metacarpal and radial bone in rheumatoid arthritis using high resolution- peripheral quantitative computed tomography". In: *International Journal of Rheumatic Diseases* 20.3 (2017), pp. 353–362. ISSN: 1756185X. DOI: 10.1111/1756-185X.12558. URL: <http://onlinelibrary.wiley.com/doi/10.1111/1756-185X.12558/abstract>.
- [28] Andres Laib, Hans J Häuselmann, and Peter Rügsegger. "In vivo high resolution 3D-QCT of the human forearm." In: *Technology and health care : official journal of the European Society for Engineering and Medicine* 6 (1998), pp. 329–337. ISSN: 0928-7329. URL: <https://www.ncbi.nlm.nih.gov/pubmed/10100936>.
- [29] Mathworks. *MATLAB - Overview*. <https://se.mathworks.com/products/matlab.html>. 2018 (accessed May 30, 2018).

- [30] MathWorks. *Image Processing and Computer Vision — MathWorks Documentation*. <https://se.mathworks.com/solutions/image-video-processing.html>. [Online; accessed 02-May-2018].
- [31] Omer Demirkaya and Asyali. *Medical Image Processing Toolbox — Image Processing with MATLAB*. <http://www.biomedimaging.org/AboutAuthors.aspx>. [Online; accessed 02-May-2018].
- [32] MathWorks. *Curve Fitting Toolbox — MathWorks Documentation*. <https://se.mathworks.com/help/curvefit/index.html>. [Online; accessed 09-May-2018].
- [33] Zachary Danziger. *Hausdorff Distance version 1.6 — MathWorks File Exchange*. <https://se.mathworks.com/matlabcentral/fileexchange/26738-hausdorff-distance>. [Online; accessed 02-May-2018].
- [34] Shawn Lankton. *Active Contour Segmentation version 1.0 — MathWorks File Exchange*. <https://se.mathworks.com/matlabcentral/fileexchange/19567-active-contour-segmentation>. [Online; accessed 02-May-2018].
- [35] Jincheng Pang. *Localized Active Contour version 1.1 — MathWorks File Exchange*. <https://se.mathworks.com/matlabcentral/fileexchange/44906-localized-active-contour>. [Online; accessed 02-May-2018].
- [36] Jan Motl. *Niblack local thresholding version 1.1 — MathWorks File Exchange*. <https://se.mathworks.com/matlabcentral/fileexchange/40849-niblack-local-thresholding>. [Online; accessed 02-May-2018].
- [37] Daydreamanatomy. *Bones of the wrist and hand — Human anatomy*. <https://daydreamanatomy.com/wp-content/uploads/2017/12/bones-of-the-wrist-and-hand-diagram-human-anatomy-hand-bone-anatomy-human-diagram-download-hand.png>. 2017 (accessed March 09, 2018).
- [38] Mikkel Østergaard, Uffe Mølner Dhøn, Anne Duer-Jensen, Merete Lund Hetland, Kim Hørslev-Petersen, Kristian Stengaard-Pedersen, Peter Junker, Jan Pdøenphant, and Bo Ejbjerg. “Patterns of magnetic resonance imaging bone erosion in rheumatoid arthritis - Which bones are most frequently involved and show the most change?” In: *Journal of Rheumatology* 38.9 (2011), pp. 2014–2017. ISSN: 0315162X. DOI: 10.3899/jrheum.110416. URL: <http://www.jrheum.org/content/38/9/2014.long>.
- [39] Edward F. Boas and Dominik Fleischmann. “CT artifacts: Causes and reduction techniques”. In: *Imaging in Medicine* 4.2 (2012), pp. 229–240. ISSN: 1755-5191. DOI: 10.2217/iim.12.13. URL: <http://www.edboas.com/science/CT/0012.pdf>.
- [40] Li Sze Chow and Raveendran Paramesran. “Review of medical image quality assessment”. In: *Biomedical Signal Processing and Control* 27 (2016), pp. 145–154. ISSN: 17468108. DOI: 10.1016/j.bspc.2016.02.006. URL: <http://dx.doi.org/10.1016/j.bspc.2016.02.006>.
- [41] Miki Sode, Andrew J. Burghardt, Jean Baptiste Pialat, Thomas M. Link, and Sharmila Majumdar. “Quantitative characterization of subject motion in HR-pQCT images of the distal radius and tibia”. In: *Bone* 48.6 (2011), pp. 1291–1297. ISSN: 87563282. DOI: 10.1016/j.bone.2011.03.755. arXiv: NIHMS150003. URL: [https://linkinghub.elsevier.com/retrieve/pii/S8756-3282\(11\)00863-5](https://linkinghub.elsevier.com/retrieve/pii/S8756-3282(11)00863-5).
- [42] Yves Pauchard, Fabio J. Ayres, and Steven K. Boyd. “Measuring patient motion in HR-pQCT”. In: *2009 IEEE International Symposium on Biomedical Imaging: From Nano to Macro*. 2. Calgary: IEEE, 2009, pp. 338–341. ISBN: 978-1-4244-3931-7. DOI: 10.1109/ISBI.2009.5193053. URL: <http://ieeexplore.ieee.org/document/5193053/>.

- [43] Emran M. Abu Anas, Jae G. Kim, Soo Y. Lee, and K Hasan. "Comparison of ring artifact removal methods using flat panel detector based CT images". In: *BioMedical Engineering Online* 10.72 (2011), pp. 1–25. ISSN: 1475-925X. DOI: 10.1186/1475-925X-10-72. URL: <https://www.ncbi.nlm.nih.gov/pmc/articles/PMC3201024/>.
- [44] Frederik Andersen, Morten M Madsen, Rasmus Klose, Kresten K Keller, Ellen M Hauge, and Christian F Pedersen. "HR-pQCT Image Quality Assessment and Enhancement". 2017.
- [45] Cheryl Barnabe, Eva Szabo, Liam Martin, Steven K. Boyd, and Susan G. Barr. "Quantification of small joint space width, periarticular bone microstructure and erosions using high-resolution peripheral quantitative computed tomography in rheumatoid arthritis". In: *Clinical and Experimental Rheumatology* 31.2 (2013), pp. 243–250. ISSN: 0392856X. DOI: 10.1016/j.bone.2010.05.034. URL: <https://www.ncbi.nlm.nih.gov/pmc/articles/PMC2926164/>.
- [46] Issac N. Bankman. *Handbook of Medical Imaging*. Ed. by William Brody, Elias Zerhouni, Rangaraj M. Rangayyan, Richard A. Robb, Roger P. Woods, H. K. Huang, and Joseph Bronzino. 2nd. Laurel, Maryland: Academic Press, 2000, p. 910. ISBN: 0120777908. DOI: 10.1016/B978-0-12-373904-9.X0001-4. URL: <https://www.sciencedirect.com/science/book/9780123739049>.
- [47] Mehmet Sezgin and Bülent Sankur. "Survey over image thresholding techniques and quantitative performance evaluation". In: *Journal of Electronic Imaging* 13.1 (2004), pp. 146–165. ISSN: 1017-9909. DOI: 10.1117/1.1631316. URL: <http://electronicimaging.spiedigitallibrary.org/article.aspx?doi=10.1117/1.1631316>.
- [48] Irwin Sobel. "An Isotropic 3 3 Image Gradient Operator". In: *Machine Vision for three-demansional Sciences* 1.1 (2015), pp. 23–34. DOI: 10.13140/RG.2.1.1912.4965. URL: <http://ci.nii.ac.jp/naid/10018992790/>.
- [49] Lawrence Gilman Roberts. "Machine perception of three-dimensional solids". PhD thesis. Massachusetts: Massachusetts Institute of Technology, 1963, pp. 1–82. ISBN: 0-8240-4427-4. URL: https://www.researchgate.net/publication/220695992/_Machine%20Perception%20of%20Three-Dimensional%20Solids.
- [50] Bernice Sacks Lipkin and Azriel Rosenfeld, eds. *Picture Processing and Psychopictorics*. Orlando, FL, USA: Academic Press, Inc., 1970. ISBN: 0124515509. URL: <https://www.elsevier.com/books/picture-processing-and-psychopictorics/lipkin/978-0-12-451550-5>.
- [51] Nikhil R. Pal and Sankar K. Pal. "A review on image segmentation techniques". In: *Pattern Recognition* 26.9 (1993), pp. 1277–1294. ISSN: 00313203. DOI: 10.1016/0031-3203(93)90135-J. arXiv: arXiv:1011.1669v3. URL: <https://www.sciencedirect.com/science/article/pii/S003132039390135J>.
- [52] John Canny. "A Computational Approach to Edge Detection". In: *IEEE transactions on pattern analysis and machine intelligence* 8.6 (1986), pp. 679–698. ISSN: 0162-8828. DOI: 10.1109/TPAMI.1986.4767851. URL: <https://ieeexplore.ieee.org/document/4767851/>.
- [53] Dzung L Pham, Chenyang Xu, and Jerry L Prince. "Current Methods in Medical Image Segmentation". In: *Annual Review of Biomedical Engineering* 2.1 (2000), pp. 315–337. ISSN: 1523-9829. DOI: 10.1146/annurev.bioeng.2.1.315. URL: <http://www.annualreviews.org/doi/10.1146/annurev.bioeng.2.1.315>.
- [54] Phan T.H. Truc, Tae-Seong Kim, Sungyoung Lee, and Young-Koo Lee. "A Study on the Feasibility of Active Contours on Automatic CT Bone Segmentation". In: *Journal of Digital Imaging* 23.6 (2010), pp. 793–805. ISSN: 08971889. DOI: 10.1007/s10278-009-9210-z. URL: <https://link.springer.com/content/pdf/10.1007/s10278-009-9210-z.pdf>.

- [55] Helen R. Buie, Graeme M. Campbell, R. Joshua Klinck, Joshua A. MacNeil, and Steven K. Boyd. "Automatic segmentation of cortical and trabecular compartments based on a dual threshold technique for in vivo micro-CT bone analysis". In: *Bone* 41.4 (2007), pp. 505–515. ISSN: 87563282. DOI: 10.1016/j.bone.2007.07.007. URL: <https://www.sciencedirect.com/science/article/pii/S8756328207005558?via=ihub>.
- [56] Andrew J. Burghardt, Galateia J. Kazakia, and Sharmila Majumdar. "A Local Adaptive Threshold Strategy for High Resolution Peripheral Quantitative Computed Tomography of Trabecular Bone". In: *Annals of Biomedical Engineering* 35.10 (2007), pp. 1678–1686. ISSN: 00906964. DOI: 10.1007/s10439-007-9344-4. URL: <https://link.springer.com/article/10.1007/s10439-007-9344-4>.
- [57] W. Birkfellner. *Applied Medical Image Processing: A Basic Course*. Taylor & Francis, 2011. ISBN: 9781439824450. URL: <https://books.google.dk/books?id=IX0XoUeW0J4C>.
- [58] Andrew J. Burghardt, Helen R. Buie, Andres Laib, Sharmila Majumdar, and Steven K. Boyd. "Reproducibility of direct quantitative measures of cortical bone microarchitecture of the distal radius and tibia by HR-pQCT". In: *Bone* 47.3 (2010), pp. 519–528. ISSN: 87563282. DOI: 10.1016/j.bone.2010.05.034. URL: <http://dx.doi.org/10.1016/j.bone.2010.05.034>.
- [59] KK Keller, JS Thomsen, K. Stengaard-Pedersen, AW Nielsen, B. Schiøttz-Christensen, L. Svendsen, M. Graakjær, PM Petersen, B. Unger, SG Kjær, BL Langdahl, and EM Hauge. "Local bone loss in patients with anti-citrullinated peptide antibody and arthralgia, evaluated with high-resolution peripheral quantitative computed tomography". In: *Scandinavian Journal of Rheumatology* 47.2 (2018), pp. 110–116. ISSN: 0300-9742. DOI: 10.1080/03009742.2017.1333629. URL: <https://doi.org/10.1080/03009742.2017.1333629>.
- [60] Kyle K. Nishiyama, Heather M. Macdonald, Helen R. Buie, David A. Hanley, and Steven K. Boyd. "Postmenopausal Women With Osteopenia Have Higher Cortical Porosity and Thinner Cortices at the Distal Radius and Tibia Than Women With Normal aBMD: An In Vivo HR-pQCT Study". In: *Journal of Bone and Mineral Research* 25.4 (2010), pp. 882–890. ISSN: 08840431. DOI: 10.1359/jbmr.091020. URL: <https://onlinelibrary.wiley.com/doi/abs/10.1359/jbmr.091020>.
- [61] Yan Kang, K Engelke, and W.A. Kalender. "A New Accurate and Precise 3-D Segmentation Method for Skeletal Structures in Volumetric CT Data". In: *IEEE Transactions on Medical Imaging* 22.5 (2003), pp. 586–598. ISSN: 0278-0062. DOI: 10.1109/TMI.2003.812265. URL: <https://ieeexplore.ieee.org/document/1207394/>.
- [62] MathWorks. *fit — MathWorks Documentation*. <https://se.mathworks.com/help/curvefit/fit.html>. [Online; accessed 09-May-2018].
- [63] J.N. Kapur, P.K. Sahoo, and A.K.C. Wong. "A new method for gray-level picture thresholding using the entropy of the histogram". In: *Computer Vision, Graphics, and Image Processing* 29.3 (1985), pp. 273–285. ISSN: 0734189X. DOI: 10.1016/0734-189X(85)90125-2. arXiv: 85 [0734-189X]. URL: <http://linkinghub.elsevier.com/retrieve/pii/0734189X85901252>.
- [64] Omer Demirkaya, Musa Asyali, and Prasanna Sahoo. *Image Processing with MATLAB: Applications in Medicine and Biology*. CRC Press, 2009. ISBN: 978-0-8493-9246-7. URL: <https://books.google.dk/books?id=D2TLBQAAQBAJ>.
- [65] Nobuyuki Otsu. "A Threshold Selection Method from Gray-Level Histograms". In: *IEEE Transactions on Systems, Man, and Cybernetics* 9.1 (1979), pp. 62–66. ISSN: 0018-9472. DOI: 10.1109/TSMC.1979.4310076. arXiv: arXiv:1011.1669v3. URL: <http://ieeexplore.ieee.org/document/4310076/>.

- [66] Wayne Niblack. *An Introduction to Digital Image Processing*. Strandberg Publishing Company, 1985. ISBN: 87-872-0055-4. URL: <https://books.google.dk/books?id=X0xRAAAAMAAJ>.
- [67] R. M. Haralick, S. R. Sternberg, and X. Zhuang. "Image Analysis Using Mathematical Morphology". In: *IEEE Transactions on Pattern Analysis and Machine Intelligence* 9.4 (1987), pp. 532–550. ISSN: 0162-8828. DOI: 10.1109/TPAMI.1987.4767941. URL: <https://ieeexplore.ieee.org/document/4767941/>.
- [68] Wikipedia. *Mathematical morphology — Binary morphology*. https://en.wikipedia.org/wiki/Mathematical_morphology. [Online; accessed 09-May-2018].
- [69] Tony F. Chan and Luminita A. Vese. "Active Contours Without Edges". In: *IEEE Transactions on Image Processing* 10.2 (2001), pp. 266–277. ISSN: 10577149. DOI: 10.1109/83.902291. URL: <https://ieeexplore.ieee.org/document/902291/>.
- [70] Shawn Lankton and Allen Tannenbaum. "Localizing Region-Based Active Contours". In: *IEEE Transactions on Image Processing* 17.11 (2008), pp. 2029–2039. ISSN: 1057-7149. DOI: 10.1109/TIP.2008.2004611. URL: <http://ieeexplore.ieee.org/document/4636741/>.
- [71] M. Kass, A. Witkin, and D. Terzopoulos. "Snakes: Active Contour Models". In: *International Journal of Computer Vision* 1.4 (1988), pp. 321–331. ISSN: 09205691. DOI: 10.1007/BF00133570. URL: <https://link.springer.com/article/10.1007/BF00133570>.
- [72] David Mumford and Jayant Shah. "Optimal Approximations by Piecewise Smooth Functions and Associated Variational Problems". In: *Communications on Pure and Applied Mathematics* 42.5 (1989), pp. 577–685. ISSN: 10970312. DOI: 10.1002/cpa.3160420503. URL: <https://onlinelibrary.wiley.com/doi/abs/10.1002/cpa.3160420503>.
- [73] Anthony Yezzi, Andy Tsai, and Alan Willsky. "A Fully Global Approach to Image Segmentation via Coupled Curve Evolution Equations". In: *Journal of Visual Communication and Image Representation* 13.1-2 (2002), pp. 195–216. ISSN: 10473203. DOI: 10.1006/jvci.2001.0500. URL: <https://www.sciencedirect.com/science/article/pii/S1047320301905000>.
- [74] Hui Zhang, Jason E. Fritts, and Sally A. Goldman. "Image segmentation evaluation: A survey of unsupervised methods". In: *Computer Vision and Image Understanding* 110.2 (2008), pp. 260–280. ISSN: 10773142. DOI: 10.1016/j.cviu.2007.08.003. arXiv: 1302.1539. URL: <https://www.sciencedirect.com/science/article/pii/S1077314207001294>.
- [75] A. Fenster and B. Chiu. "Evaluation of Segmentation algorithms for Medical Imaging". In: *2005 IEEE Engineering in Medicine and Biology 27th Annual Conference*. IEEE, 2005, pp. 7186–7189. ISBN: 0-7803-8741-4. DOI: 10.1109/IEMBS.2005.1616166. URL: <http://ieeexplore.ieee.org/document/1616166/>.
- [76] F. Hausdorff. *Grundzüge der Mengenlehre*. Chelsea, 1949. URL: <https://books.google.dk/books?id=tw8RnQAACAAJ>.
- [77] Abdel Aziz Taha and Allan Hanbury. "Metrics for evaluating 3D medical image segmentation: Analysis, selection, and tool". In: *BMC Medical Imaging* 15.29 (2015), pp. 1–28. ISSN: 14712342. DOI: 10.1186/s12880-015-0068-x. arXiv: NIHMS150003. URL: <http://dx.doi.org/10.1186/s12880-015-0068-x>.
- [78] Lee R. Dice. "Measures of the Amount of Ecologic Association Between Species". In: *Ecology* 26.3 (1945), pp. 297–302. ISSN: 00129658. DOI: 10.2307/1932409. arXiv: 1932409 [10.2307]. URL: <http://doi.wiley.com/10.2307/1932409>.
- [79] P.A. van den Elsen, E.-J.D. Pol, and M.A. Viergever. "Medical Image Matching - A Review with Classification". In: *IEEE Engineering in Medicine and Biology Magazine* 12.1 (1993), pp. 26–39. ISSN: 0739-5175. DOI: 10.1109/51.195938. URL: <http://ieeexplore.ieee.org/document/195938/>.

- [80] J B Antoine Maintz and Max a Viergever. "An Overview of Medical Image Registration Methods". In: *Nature* 12.6 (1996), pp. 1–22. ISSN: 1361-8415. DOI: 10.1.1.39.4417. URL: <http://citeseerx.ist.psu.edu/viewdoc/summary?doi=10.1.1.39.4417>.
- [81] Fatma El-Zahraa Ahmed El-Gamal, Mohammed Elmogy, and Ahmed Atwan. "Current trends in medical image registration and fusion". In: *Egyptian Informatics Journal* 17.1 (2016), pp. 99–124. ISSN: 11108665. DOI: 10.1016/j.eij.2015.09.002. URL: <http://linkinghub.elsevier.com/retrieve/pii/S111086651500047X>.
- [82] Francisco P.M. Oliveira and João Manuel R.S. Tavares. *Medical image registration: a review* Francisco. 2014. DOI: 10.1080/10255842.2012.670855. URL: <http://dx.doi.org/10.1080/10255842.2012.670855>.
- [83] J B Antoine Maintz and M A Viergever. "A survey of medical image registration." In: *Medical image analysis* 2.1 (1998), pp. 1–36. ISSN: 1361-8415. DOI: 10.1.1.39.4417. URL: <https://www.sciencedirect.com/science/article/pii/S1361841501800268?via=I%3Dihub>.
- [84] Frederik Andersen, Morten M Madsen, Rasmus Klose, Kresten K Keller, Ellen M Hauge, and Christian F Pedersen. "HR-pQCT Image Registration and Segmentation". 2017.
- [85] J.V. Hajnal and D.L.G. Hill. *Medical Image Registration*. Biomedical Engineering. CRC Press, 2001. ISBN: 9781420042474. URL: <https://books.google.dk/books?id=2dtQNsk-qBQC>.
- [86] Frederik Maes, André Collignon, Dirk Vandermeulen, Guy Marchal, and Paul Suetens. "Multi-modality Image Registration by Maximization of Mutual Information Frederik". In: *IEEE Transactions on Medical Imaging* 16.2 (1997), pp. 187–198. ISSN: 02780062. DOI: 10.1109/42.563664. URL: <http://ieeexplore.ieee.org/document/563664/>.
- [87] MathWorks. *RegularStepGradientDescent* — *MathWorks Documentation*. <https://se.mathworks.com/help/images/ref/registration.optimizer.regularstepgradientdescent.html>. [Online; accessed 30-April-2018].
- [88] MathWorks. *Image Labeler* — *MathWorks Computer Vision System Toolbox Documentation*. <https://se.mathworks.com/help/vision/ref/imagelabeler-app.html>. [Online; accessed 03-May-2018].
- [89] MathWorks. *Profile* — *MathWorks Documentation*. <https://se.mathworks.com/help/matlab/ref/profile.html>. [Online; accessed 17-May-2018].